University of Turin

Master Thesis

Nuclear and Subnuclear Physics

Study of the decay $\Upsilon(10753) \to \pi^+\pi^- h_b(1P)$ at the Belle II experiment

Author:
Giulia Italia

Supervisors:
Prof. Stefano Spataro
Dr. Umberto Tamponi

Contents

List of Figures

List of Tables

Abstract

In 2019, a new structure was discovered by the Belle experiment while performing an energy scan above the $\Upsilon(4S)$ mass. This resonance was observed around 10.753 GeV in the energy-dependent cross section of the process $e^+e^- \to \pi^+\pi^-\Upsilon(nS)$, with n = 1, 2, 3, and was therefore named $\Upsilon(10753)$. The new structure was determined to be an exotic state, but to better understand its nature, more statistic was needed. Thus, in 2021, the Belle II experiment performed a new energy scan, with higher luminosity and sampling four new energy points around the $\Upsilon(10753)$ mass to improve the coverage of the region of interest.

The aim of this work is to study the $\Upsilon(10753) \to \pi^+\pi^-h_b(1P)$ decay. This process can occur through a direct transition but is expected to be suppressed because it would require a spin flip of the heavy quark. However, the following transition, proceeding through an intermediate charged exotic state, is also possible and is not affected by spin-flip suppression: $\Upsilon(10753) \to \pi^\pm Z_b(10610)^\mp \to \pi^\pm\pi^\mp h_b(1P)$. Therefore, this decay channel is particularly interesting because it allows one to investigate the nature of the $\Upsilon(10753)$ state, but also to search for hints of the intermediate $Z_b(10610)$ production.

For this study, a blind analysis will be performed and an inclusive strategy for the reconstruction of $h_b(1P)$ and $Z_b(10610)$ will be adopted, looking, respectively, at the recoil mass distributions of $\pi^+\pi^-$ pairs and of the single π.

In Chapter 1 of this work, an overview of quarkonium spectroscopy and exotic states will be discussed. In Chapter 2, the Belle II experiment and its detectors will be presented. Then, in Chapter 3, the Belle II software will be discussed. Chapter 4 illustrates the motivations and challenges of this study, while also providing an overview of the analysis. In Chapter 5 the evaluation of the tracking reconstruction performance through Monte Carlo simulations, with a focus on low momentum tracks, will be presented. The track selection cuts for signal pions and their efficiency will be studied using Monte Carlo samples of both decay channels in Chapter 6. In Chapter 7 a study will be presented to validate the efficiency of these cuts, using MC simulations and experimental data from the following channel: $D^{*+} \to \pi^+D^0 \to \pi^+K^-\pi^+$. Then, in Chapter 8, the results of this work will be summarized.

Abstract

Nel 2019, durante lo scan di energie al di sopra della massa del mesone $\Upsilon(4S)$, una nuova struttura è stata scoperta dall'esperimento Belle. Questa risonanza è stata osservata intorno al valore di energia di 10.753 GeV nella sezione d'urto del processo $e^+e^- \to \pi^+\pi^-\Upsilon(nS)$, con n = 1, 2, 3, ed è stata quindi denominata $\Upsilon(10753)$. Questa nuova struttura è stata definita come uno stato esotico, ma per comprenderne meglio la natura era necessaria maggiore statistica. Così, nel 2021, l'esperimento Belle II ha realizzato un nuovo scan di energie, con maggiore luminosità, acquisendo dati in quattro nuovi punti intorno alla massa dello stato $\Upsilon(10753)$, in modo da avere una maggiore copertura della regione di interesse.

L'obiettivo di questo lavoro è quello di studiare il decadimento $\Upsilon(10753) \to \pi^+\pi^-h_b(1P)$. Questo processo può avvenire attraverso una transizione diretta, ma ci si aspetta che questa sia soppresa in quanto richederebbe una inversione dello spin del quark pesante. Tuttavia, è anche possibile la seguente transizione: $\Upsilon(10753) \to \pi^\pm Z_b(10610)^\mp \to \pi^\pm\pi^\mp h_b(1P)$. Questa procede passando attraverso uno stato esotico carico intermedio e non è influenzata dalla soppressione legata allo spin-flip. Quindi, questo canale di decadimento è particolarmente interessante in quanto permette non solo di investigare la natura della $\Upsilon(10753)$, ma anche di cercare dei segnali della produzione dello stato $Z_b(10610)$.

Per questo studio sarà effettuata un'analisi di tipo blind e per la ricostruzione sarà adottata una strategia inclusiva, esaminando per $h_b(1P)$ e $Z_b(10610)$, rispettivamente, le distribuzioni della massa di rinculo della coppia $\pi^+\pi^-$ e dei singoli π.

Nel Capitolo 1 di questo lavoro verrà presentata una panoramica della spettroscopia di quarkonio e saranno discussi gli stati esotici. Nel Capitolo 2 veranno invece introdotti l'esperimento Belle II ed i suoi rivelatori. Nel Capitolo 3 il software utilizzato in Belle II verrà discusso. Il Capitolo 4 illustra le motivazioni e le sfide di questo studio ed inoltre fornisce anche una panoramica dell'analisi. Nel Capitolo 5 verrà presentata la valutazione della performance dell'algoritmo di tracciamento usato per la ricostruzione, attraverso simulazioni Monte Carlo, con particolare attenzione alle tracce a basso momento. Succesivamente, nel Capitolo 6, saranno studiati i tagli per la selezione delle tracce dei pioni di segnale e le corrispettive efficienze, utilizzando simulazioni Monte Carlo per entrambi i canali di decadimento. Nel Capitolo 7 sarà poi presentato uno studio per la validazione dell'efficienza di questi tagli sfruttando simulazioni Monte Carlo e dati sperimentali del seguente canale di controllo: $D^{*+} \to \pi^+D^0 \to \pi^+K^-\pi^+$. Infine, nel Capitolo 8, saranno riassunti i risultati di questo lavoro.

Chapter 1

Introduction

Quarkonium spectroscopy is currently a field of great interest in high energy physics, especially after the discovery of many candidates of the so-called *exotic states* in the last two decades.

In Sections 1.1 and 1.2 of this chapter an overview of both quarkonium spectroscopy and production techniques of quarkonium states will be presented. Then, in Section 1.3, exotic states will be discussed. In Section 1.4, quarkonia spectra will be presented, with a focus on the states of interest for this work in Sections 1.5 and 1.6.

In the following sections, [1] and [2] have been used as general references.

1.1 Quarkonium overview

In particle physics, the name *quarkonium* is used to identify a bound state of a heavy quark and its own antiquark, generally indicated with $Q\bar{Q}$. The quarkonium states formed by $c\bar{c}$ and $b\bar{b}$ pairs are named respectively *charmonia* and *bottomonia*. Instead, *top* quarks cannot bind to form a quarkonium state, since they weakly decay before a bound state is created.

The masses of these states can be predicted using a simple phenomenological approach based on a non-relativistic potential model. In fact, due to the large masses of the heavy quarks and their small relative velocities, the $Q\bar{Q}$ system can be treated in a non-relativistic limit and the masses evaluated by solving the Schrödinger equation with a Coulomb-like potential that also incorporates confinement forces (the Cornell potential). Despite being a phenomenological model and not an actual theory, this approach successfully predicted most of the observed quarkonium states.

The first charmonium state, named J/ψ, was discovered in 1974 simultaneously by two independent research groups at SLAC [3] and BNL [4]. A few years later, in 1977, the first bottomonium state, the $\Upsilon(1S)$, was also found at Fermilab [5]. Then, in the next 20 years, many other new states, both in charmonium and bottomonium spectra, were observed.

Later, taking advantage of improved technologies and the higher achievable luminosity, the research moved onto the precision frontier. In this context, in 2003, the Belle experiment observed a new resonance [6], which showed an internal charmonium structure but whose properties were not compatible with the models' predictions. This state was named $X(3872)$, due to its unknown nature and the energy value around which it was observed, and was the first example of a new family of states without a clear theoretical interpretation, therefore called *exotic states*. In the past 20 years, several other candidates belonging to this family, both neutral and charged, have been found by various experiments [1].

Nowadays, more advanced theories, such as Lattice QCD and Non-Relativistic Effective Field Theories (NR EFTs), are available to describe quarkonia spectra and allow predictions that are more in agreement with experimental data. Those will not be discussed in this work, but more can be found in [7].

Instead, several models have been proposed to describe exotic states, but up to this point none of the hypotheses have been confirmed and their nature remains unclear.

1.2 Quarkonium production at e^+e^- colliders

In particle physics experiments at e^+e^- colliders, mainly two techniques are used to produce quarkonium states.

The first one takes advantage of the direct production process, in which an e^+e^- pair annihilates creating a virtual photon that might later decay into a quark-antiquark pair. If the collision energy is about the mass of a quarkonium state, the cross section of the process increases because of the resonance in formation. Moreover, electrons can also emit before annihilating one or more photons, through the *Initial-State Radiation* (ISR) process, which allows the creation of quarkonium states with energies lower than the energy of the collision (Fig. 1.1(d)). For the direct production mechanism, the collision energy is well determined, thus it is possible to perform energy scans of regions of interest. Due to the fact that the photon has quantum numbers $J^{PC} = 1^{--}$, where J, P, C are, respectively, the total momentum, parity and charge conjugation, only states with the same quantum numbers can be produced.

The second production technique takes advantage of the decay of heavy particles, such as quarkonium states different from the one being produced or open charm/bottom mesons. For example, charmonium production in B meson decays occurs mainly through the weak interaction transition $b \to c$ with the emission of a virtual W^- boson; the c quark can then combine with other sea quarks into a conventional or non-conventional state (Fig. 1.1(a)). For this mechanism, the produced resonances can be studied by reconstructing all the particles involved in the process, therefore using an exclusive strategy. The advantage of this technique is that states with quantum numbers different from $J^{PC} = 1^{--}$ can also be investigated [1].

Both production techniques are widely used at B-factories, such as Belle and Belle II.

Alternative methods to produce quarkonia states at e^+e^- colliders are the *double charmonium production* and the *two-photon fusion process*. In the first one, if the center-of-mass energy in the collision is enough, the direct production of two charmonium states together can occur (Fig. 1.1(c)); in the latter (Fig. 1.1(b)), the incoming e^+ and e^- radiate two photons that interact, producing a quark-antiquark pair, usually $c\bar{c}$, with even J and C quantum numbers [8].

Moreover, other techniques can be used to produce quarkonium states at hadron colliders. These will not be discussed, since in this analysis events produced at an e^+e^- collider will be studied.

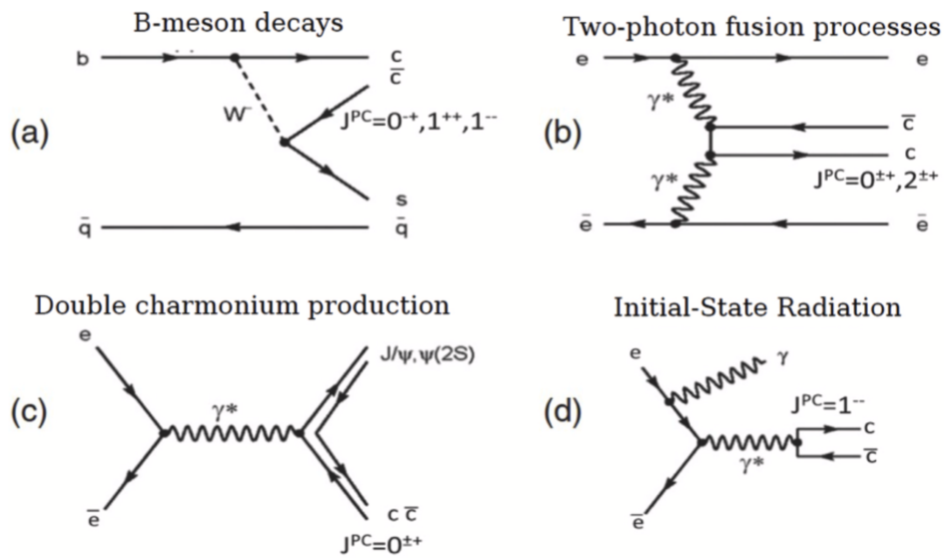

Figure 1.1: Quarkonium production techniques at e^+e^- colliders [1].

1.3 Exotic States

The strong force is the fundamental interaction that confines quarks into hadrons. The theory that describes this force is named *Quantum Chromo-Dynamics* (QCD) and is based on the gauge symmetry group SU(3), which is a non-Abelian group. Both quarks and gluons are characterized by a color charge, a degree of freedom which can assume tree distinct values: red, green and blue. Gluons mediate the interaction between quarks, by carrying a color charge, as well as taking part in the interaction itself; indeed, since QCD is a non-Abelian gauge theory, they can also self-interact.

Up to this time, no particle with a color charge has ever been observed; all known hadrons are made by different neutral combinations of quarks to form color-singlet states. In the quark model, hadrons are organized in two groups: *baryons*, which are bound states of three valence quarks (qqq), and *mesons*, which are bound states of a valence quark and an antiquark ($q\bar{q}$). These are the simplest color singlet states that can be formed. However, QCD also allows for the existence of more complex white combinations. These are the so-called *exotic states*, structures that most likely have more degrees of freedom compared to ordinary hadrons, such as multiquark states or structures with active gluons [2].

1.3.1 Exotic states models

In order to explain the nature of these new exotic states, several models have been proposed [7, 2], which can be divided into two main groups:

- **Structures with active gluons**, such as:
  - *Glueballs*, defined as bound systems of gluons, that do not carry any valence quark. From Lattice QCD calculations, glueball masses have been predicted to be up to 5 GeV/c^2.
  - *Hybrid states*, described as quark-antiquark structures in which gluons act also as active degrees of freedom.
- **Multiquark configurations**, such as:
  - *Hadroquarkonium*, identified as a compact quarkonium-like core surrounded by a light-quark and antiquark cloud.
  - *Hadronic molecules*, in which quarks and antiquarks create a compound state of two heavy hadrons. An important feature of these structures is that, when close to the threshold of its constituents, the molecule is quite extended.
  - *Tetraquark states*, defined as states containing di-quarks (light and heavy quark pair) and anti-di-quarks (light and heavy antiquark pair) structures. These structures are more compact compared to hadronic molecules.

A graphical representation of all the models previously discussed can be found in Fig. 1.2.

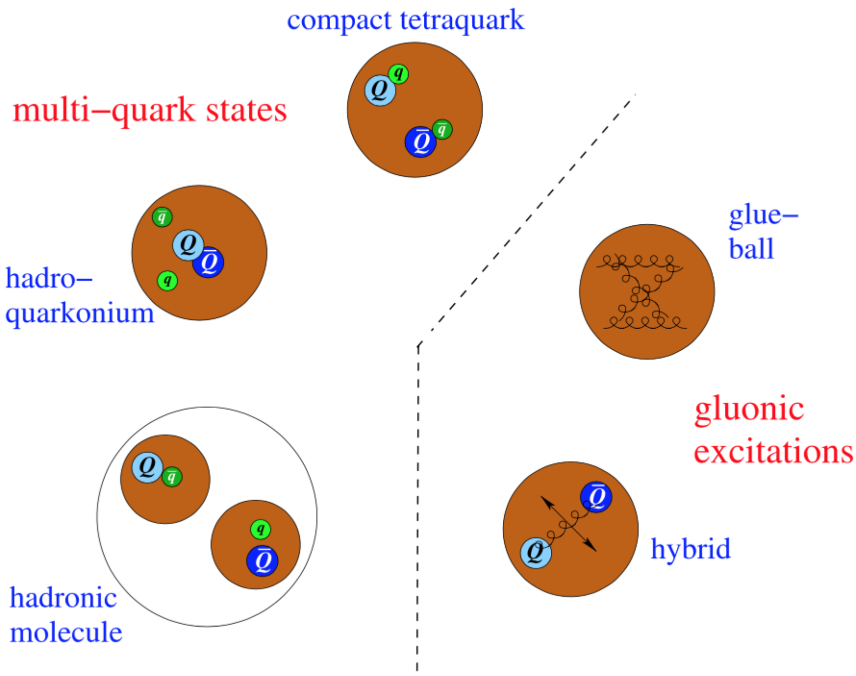

Figure 1.2: Graphical representation of the most common structure models for the exotic states [2].

1.3.2 Exotic states nomenclature

To describe the exotic states, the following traditional XYZ naming scheme [1] is generally adopted in most of the literature on the subject:

- *Y states* are all exotic neutral vectorial states. They have $J^{PC} = 1^{--}$ as quantum numbers, therefore they can be directly produced in e^+e^- collisions since they have the same quantum numbers of the virtual photon.
- *X states* are all the other neutral states. They have J^{PC} different from 1^{--}.
- *Z states* are all exotic charged states. From experimental results, they have been observed to decay into a quarkonium state and a light charged meson (but also into open-flavor meson pairs and a light charged meson) and they can form isospin triplets (they can have a neutral partner).

Due to the increasing number of exotic states discovered in recent years, the PDG [9] has adopted a new naming scheme proposed by the LHCb collaboration [10], to extend the quark model-based naming scheme used for ordinary quarkonia to exotic states. The new names do not carry information about the possible nature of the states, but instead they carry information about the quantum numbers. Excluding the ground states, a mass label is also added to the name symbol. For example, the states known as $X(3872)$, $Y(4230)$ and $Z_b(10610)$ with the traditional nomenclature will appear as $\chi_{c1}(3872)$, $\psi(4230)$ and $T_{b\bar{b}1}(10610)$, respectively, using the new naming scheme. In this work, the traditional XYZ naming scheme will be used most of the time.

1.3.3 $X(3872)$

The first experimental evidence of this new family of states was found, in 2003, in the heavy quark sector by the Belle experiment [6]. When the research in the quarkonium field moved onto the precision frontier, the collaboration was looking for some of the remaining missing states that were already expected by potential model predictions. In particular, the $J^{PC} = 2^{--}$ state was investigated by studying the $\pi\pi J/\psi$ invariant mass distribution. Instead, a narrow charmonium-like resonance was found near the $D\bar{D}^*$ threshold, as shown in Fig. 1.3.

This state has been seen in the $B^\pm \to K^\pm\pi^+\pi^- J/\psi$ process, and its internal charmonium structure was demonstrated by its decay into a J/ψ state. However, the properties of this new resonance were not compatible with the ordinary quarkonia predictions made by the potential model. The particle was therefore named $X(3872)$, due to the fact that its nature was fairly unknown.

Since it was the first exotic candidate to be discovered, this resonance has been extensively studied by different experiments and using various production techniques, such as e^+e^- collisions at the charmonium energies or B-meson decays at B-factories, but also at hadron colliders experiments.

Despite this, the debate regarding its nature is still pretty much open. For example, the $X(3872)$ average mass value, as reported by the PDG [9], is compatible, within the uncertainties, with the value of the $D\bar{D}^*$ threshold, which does not allow to establish if the resonance is above or below the $D\bar{D}^*$ threshold:

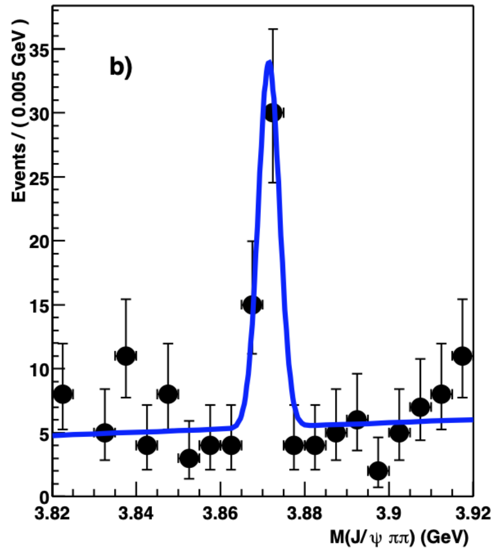

Figure 1.3: The plot of the $X(3872)$ discovery in the $\pi\pi J/\psi$ invariant mass distribution [6].

$$M_{X(3872)} = (3871.64 \pm 0.06)\ \text{MeV}/c^2$$
$$M_{D^0} + M_{\bar{D}^{*0}} = (3871.69 \pm 0.07)\ \text{MeV}/c^2$$

Moreover, the width of this state has been determined, as declared by PDG [9]:

$$\Gamma_{X(3872)} = (1.19 \pm 0.21)\ \text{MeV}$$

Despite being the most studied exotic candidate, so far the $X(3872)$ inner structure still remains under debate [1].

1.3.4 $Y(4260)$

The $Y(4260)$ state was the first vector exotic candidate to be discovered and was found by the BaBar collaboration while studying the $e^+e^- \to \pi^+\pi^- J/\psi$ process, while searching for the X(3872) previously seen by Belle. A peak was observed around 4.26 GeV/c^2 in the $\pi^+\pi^- J/\psi$ invariant mass distribution [11], as shown in Fig.1.4.

Being directly produced in e^+e^- collision, it was identified as a vector candidate.

Its non-conventional structure was confirmed by the study of the ratio $R = \sigma(e^+e^- \to hadrons)/\sigma(e^+e^- \to \mu^+\mu^-)$, since a dip can be observed around the 4.26 GeV energy, as shown in Fig. 1.5.

If $Y(4260)$ had a conventional charmonium structure, the decay into an open-charm pair should be the dominant process, as dictated by the OZI rule, which states that a strong decay process described by a disconnected Feynman diagram is suppressed compared to the one described by a connected diagram. A Feynman diagram is defined as disconnected if it can be divided into two parts by a single line cutting the gluon lines, so that initial state particles are on one side and final state particles are on the other. An example is shown in Fig. 1.6.

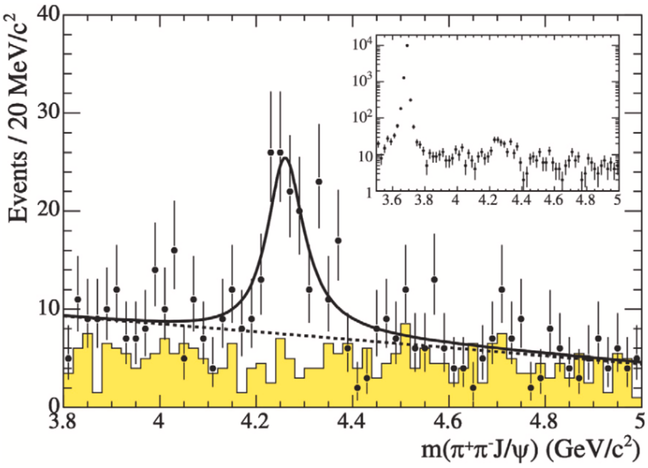

Figure 1.4: The $Y(4260)$ peak observed in the $\pi^+\pi^- J/\psi$ invariant mass distribution [11].

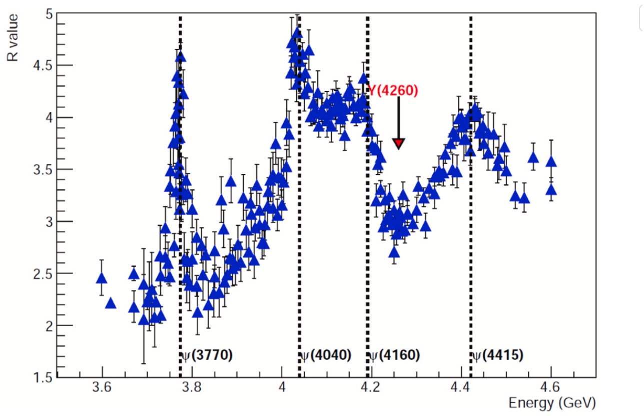

Figure 1.5: $R = \sigma(e^+e^- \to hadrons)/\sigma(e^+e^- \to \mu^+\mu^-)$ measurement at different center-of-mass energies [12]. Dashed black lines identify conventional charmonium vector states.

In the R ratio distribution, peaks are present corresponding to the conventional charmonium states, while a dip is observed corresponding to the $Y(4260)$ mass; therefore, the $Y(4260)$ cannot be identified as a conventional charmonium state.

Further studies above the open charm threshold made by the BESIII collaboration, with higher precision compared to previous measurements, showed that the $Y(4260)$ peak was actually composed of two different resonances, which have been named $Y(4230)$ and $Y(4320)$ [13]. The mass and width values of the two structures obtained from the study of the process $e^+e^- \to \pi^+\pi^- J/\psi$ are, respectively:

$$M_{Y(4230)} = (4222.0 \pm 3.1 \pm 1.4)\ \text{MeV}/c^2$$
$$\Gamma_{Y(4230)} = (44.1 \pm 4.3 \pm 2.0)\ \text{MeV}$$

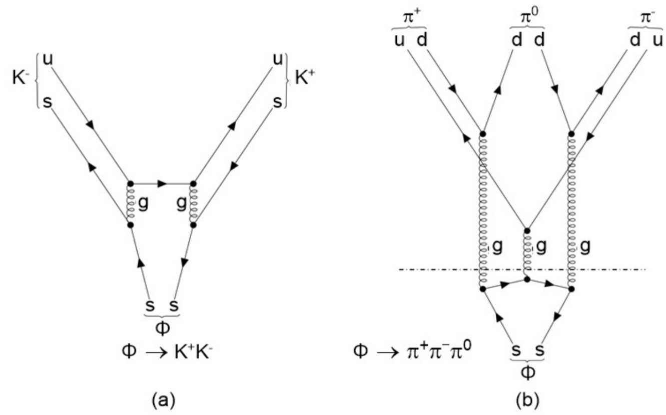

Figure 1.6: Schematic representation of the OZI rule applied to the decay of the ϕ resonance. The $\phi \to K^+K^-$ process (a) has a connected diagram, while the $\phi \to \pi^+\pi^-\pi^0$ decay is represented by a disconnected diagram. Therefore, the first process is favored, while the second one is suppressed.

$$M_{Y(4320)} = (4320.0 \pm 10.4 \pm 7.0)\ \text{MeV}/c^2$$
$$\Gamma_{Y(4320)} = (101.4^{+25.3}_{-19.7} \pm 10.2)\ \text{MeV}$$

where the first uncertainty is statistical, the second is systematic.

So far, a unique interpretation of the nature of these states has not been found [1].

1.3.5 Z charged exotic states

Among the *exotics*, charged states are particularly interesting, since their nature is manifestly exotic.

The experimental measurements have shown that they decay into conventional quarkonium states, therefore their inner structure must be composed of a $Q\bar{Q}$ pair. Meanwhile, they also carry an electric charge, thus they must also contain at least a quark-antiquark $q\bar{q}'$ pair. This dictates that these states must contain at least four quarks, which implies that they are undoubtedly exotic.

An example of exotic charged state is the $Z_b(10610)$ resonance, which is of interest for the analysis presented in this work, therefore it will be discussed in detail in section 1.6 .

1.4 $Q\bar{Q}$ sector spectra

Large part of the masses of charmonium and bottomonium states has been correctly predicted by theoretical models, such as potential models and, more recently, by Lattice QCD and Non-Relativistic Effective Field Theories (NR EFTs). Nevertheless, in the last 20 years, also several exotic states candidates, which do not have a place in the conventional quarkonia spectra, have been observed.

The current spectra of states in the $c\bar{c}$ and the $b\bar{b}$ sectors, including both conventional quarkonia and quarkonium-like states, are shown in Fig. 1.7 and Fig. 1.8, as reported by the PDG [9], updated on March 2024. Solid lines identify states that have been experimentally established and therefore already included in the PDG Summary Tables, while dashed lines are used for states not yet established, but whose quantum numbers have already been assigned. Grey arrows describe the dominant hadronic transitions between these states. In these figures, the new PDG naming scheme, already discussed in 1.3.2, is used.

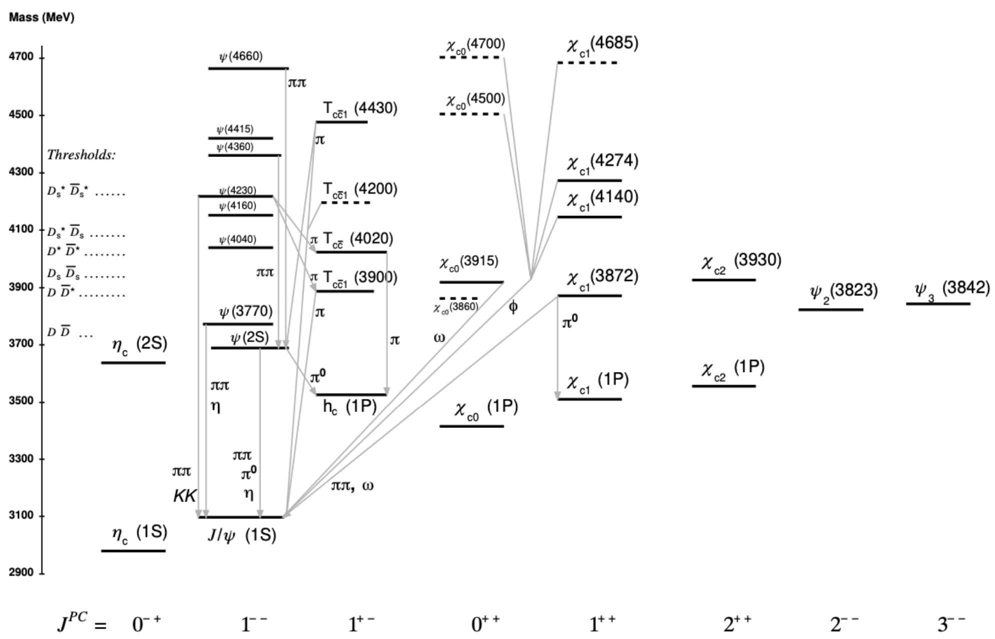

Figure 1.7: Spectrum of states in the $c\bar{c}$ sector (PDG new naming scheme is used). Solid lines stay for the established states, dashed lines for states still requiring confirmation.

All exotic states have been found to be above the open-flavor threshold, defined as the minimum energy that allows quarkonium states to decay into a pair of open-flavor mesons, each containing a heavy quark *(charm or bottom)* and a light quark.

In comparison to the charmonium spectrum, it can be noticed that in the bottomonium spectrum the number of exotic candidates found above the open-flavor threshold is significantly lower. This is mostly due to the fact that the region above the open-bottom threshold has been less explored so far, since the available statistics for e^+e^- collisions above $\Upsilon(4S)$ energy is limited.

For reference, an overview of some of the most recent and interesting results in exotic states spectroscopy can be found in [1].

The aim of this thesis is to study the $\Upsilon(10753) \to \pi^+\pi^- h_b(1P)$ and the $\Upsilon(10753) \to \pi^\pm Z_b(10610)^\mp \to \pi^\pm\pi^\mp h_b(1P)$ decays. In these transitions two exotic candidates found in the $b\bar{b}$ sector are observed, namely $\Upsilon(10753)$ and $Z_b(10610)$, a.k.a. $T_{b\bar{b}1}(10610)$. These will be discussed in detail in the following sections.

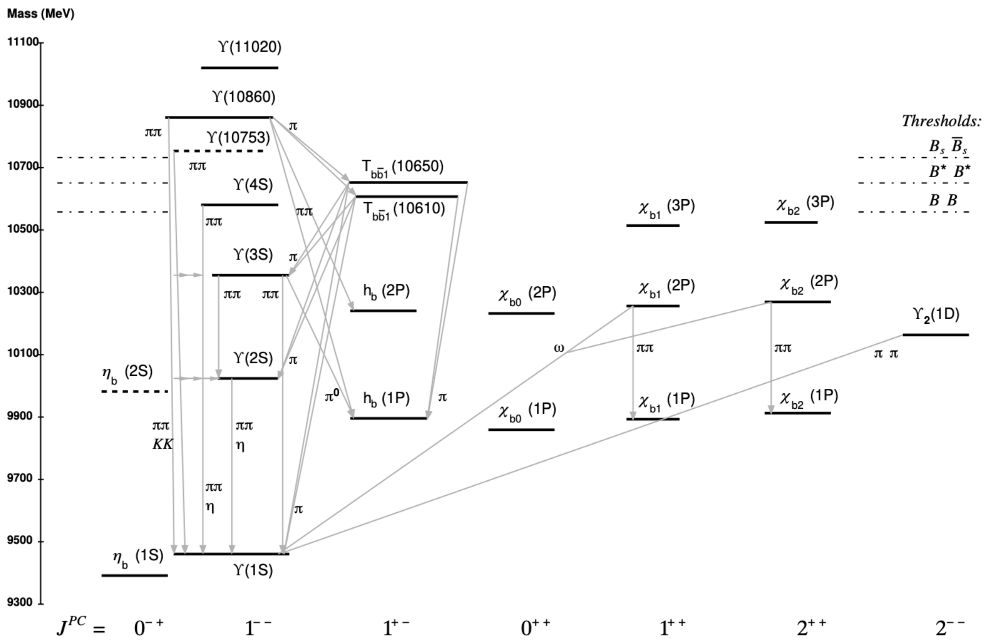

Figure 1.8: Spectrum of states in the $b\bar{b}$ sector (PDG new naming scheme is used). Solid lines stay for the established states, dashed lines for states still requiring confirmation.

1.5 $\Upsilon(10753)$

To better understand the nature of the observed vector states above the $B\bar{B}$ threshold, such as $\Upsilon(10860)$ and $\Upsilon(11020)$, generally called $\Upsilon(5S)$ and $\Upsilon(6S)$, in 2019, the Belle collaboration started to study the energy scan data collected above the $\Upsilon(4S)$, in the energy range from 10.63 GeV to 11.02 GeV. In this context, a new structure was found around 10.75 GeV in the energy-dependent cross section of the process $e^+e^- \to \Upsilon(nS)\pi^+\pi^-$, with $n = 1, 2, 3$ [14], as shown in Fig. 1.9.

A simultaneous fit of the three decay modes was made, including energy points around the masses of the $\Upsilon(5S)$ and $\Upsilon(6S)$ states and also in the region of the new resonance. For the new structure amplitude the Breit-Wigner parametrization was used. The mass and width values of the newly observed resonance obtained from the fit results are respectively:

$$M = (10752.7 \pm 5.9^{+0.7}_{-1.1}) \text{ MeV}/c^2$$
$$\Gamma = (35.5^{+17.6+3.9}_{-11.3-3.3}) \text{ MeV}$$

where the first uncertainty is statistical, the second is systematic.

This new structure was directly produced in e^+e^- collisions, therefore the quantum numbers $J^{PC} = 1^{--}$ have been assigned.

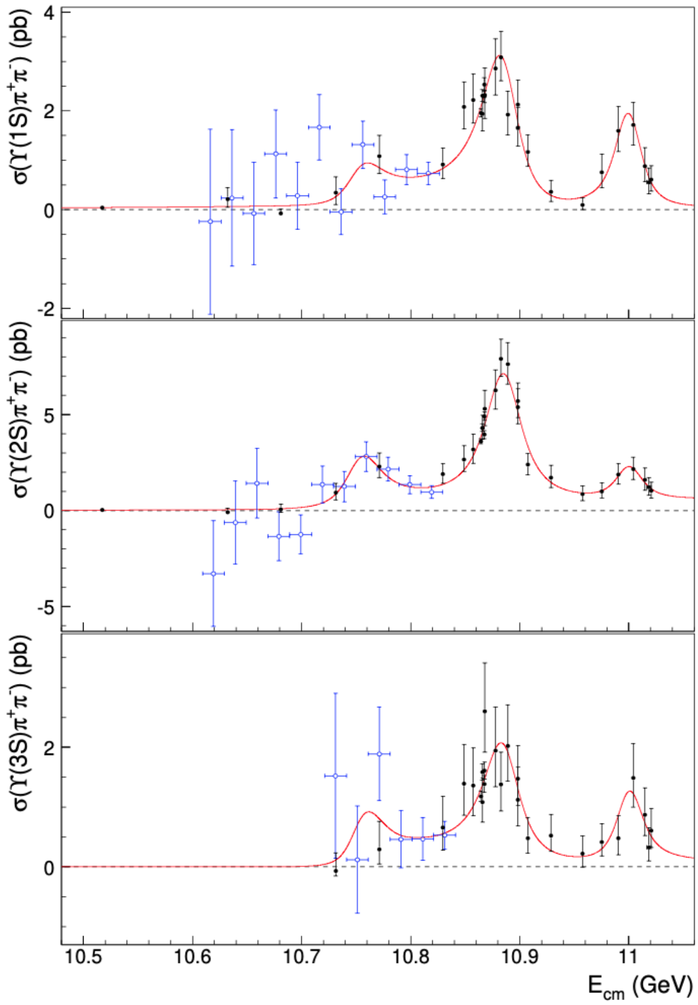

Figure 1.9: Energy-dependent cross section of $e^+e^- \rightarrow \Upsilon(nS)\pi^+\pi^-$, with $n = 1, 2, 3$ [14]. Black dots with error bars represent data from the energy scan. Red lines show the results of the simultaneous fit of the three decay modes. Blue dots with error bars are from ISR process from $\Upsilon(5S)$ on-resonance data and are intended for visualization only.

The new resonance also showed some similarities with another exotic vector candidate observed in the $c\bar{c}$ sector, the $Y(4260)$, previously discussed in Section 1.3.4.

In analogy to what has been observed in the charmonium sector around the 4.26 GeV energy, as shown in Fig. 1.5, in the $\sigma(e^+e^- \rightarrow b\bar{b})$ distribution measured using BaBar and Belle experiments data [15], a dip at around 10.750 GeV is found, as shown in Fig. 1.10. The dip can be interpreted as the interference between a Breit-Wigner function and a background component, suggesting that the $\Upsilon(10753)$ cannot be identified as a conventional bottomonium state.

In order to explain the $\Upsilon(10753)$ exotic nature, several models have been proposed, suggesting a tetraquark structure [16, 17], a hybrid state [18] or even a conventional bottomonium state [19]. However, neither of these hypotheses has yet been validated. To further investigate its nature, more measurements need

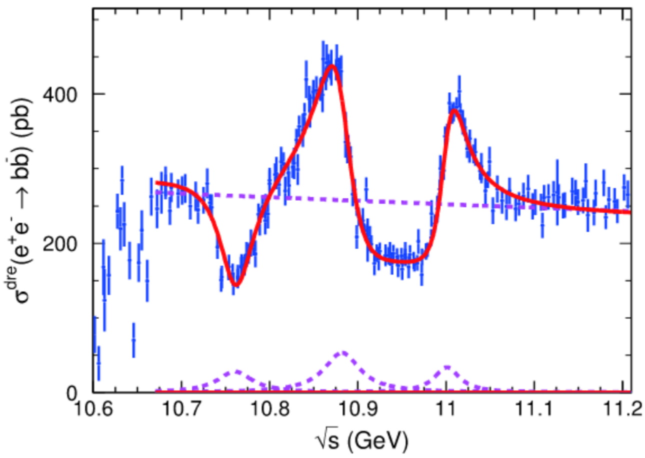

Figure 1.10: Fit of the $\sigma(e^+e^- \to b\bar{b})$ distribution with the coherent sum of a continuum amplitude and three Breit-Wigner functions. The solid red line is the total fit; the dashed lines represent the four components [15].

to be done by studying $\Upsilon(10753)$ different decay channels, and therefore more statistics is needed.

In November 2021, the Belle II experiment collected a new data sample by performing an energy scan at four energy points around 10.753 GeV. These energy points were chosen to be in between those already inspected by the Belle experiment, in order to improve the coverage of the region of interest. The new energy scan was done with higher luminosity, corresponding to a total of 19.6 fb^{-1}, compared to the previous data collected with around 1 fb^{-1} per energy point, as shown in Fig. 1.11.

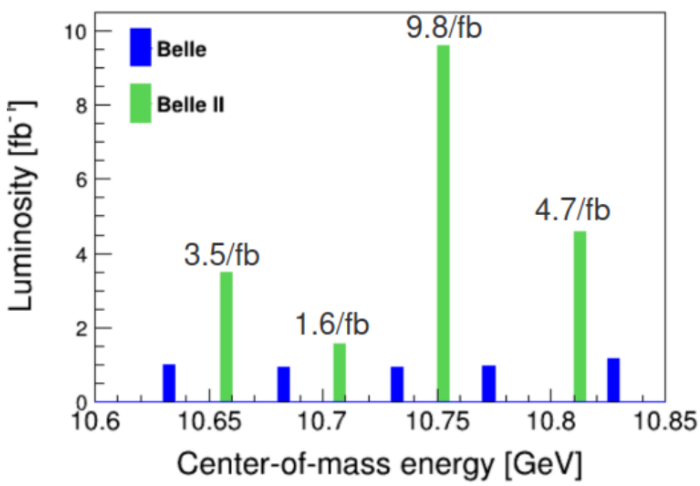

Figure 1.11: Energy points and respective luminosity values for the scan data collected by Belle (blue) and Belle II (green).

1.6 $Z_b(10610)$ and $Z_b(10650)$

The first hint of exotic charged states in the bottomonium sector was found by the Belle experiment during spectroscopy studies above the $\Upsilon(4S)$ energy. For these measurements, a data sample collected near the peak of the $\Upsilon(5S)$ resonance was used.

The collaboration first reported the observation of anomalously high rates for both the $\Upsilon(5S) \to \pi^+\pi^-\Upsilon(nS)$, with $n = 1, 2, 3$, and $\Upsilon(5S) \to \pi^+\pi^- h_b(mP)$, with $m = 1, 2$, processes. In particular, the partial widths for $\Upsilon(5S) \to \pi^+\pi^-\Upsilon(nS)$ exceeded by more than two orders of magnitude the values previously measured for di-pion transitions between the lower Υ resonances [20]. Furthermore, the $\Upsilon(5S) \to \pi^+\pi^- h_b(mP)$ rates were observed to be comparable to those of $\Upsilon(5S) \to \pi^+\pi^-\Upsilon(nS)$ [21]. Such a large rate was unexpected because the direct production of $h_b(mP)$ requires a spin-flip of the b quark, thus the process should be suppressed because it breaks the Heavy Quark Spin Symmetry (HQSS); instead, the production of the $\Upsilon(nS)$ preserves the symmetry. The observations were not compatible with the theoretical expectations, suggesting that some exotic mechanism could be contributing to these processes.

To further investigate, the $\Upsilon(nS)\pi^\pm$ invariant mass distributions were studied for the $\Upsilon(5S) \to \pi^+\pi^-\Upsilon(nS)$ decay channels; for the $\Upsilon(5S) \to \pi^+\pi^- h_b(mP)$ process the recoiling mass against the single charged pion was analyzed instead. In both cases, a clear two-peak structure was observed at the 10.61 GeV/c^2 and 10.65 GeV/c^2 masses, as shown in Fig. 1.12. These two charged bottomonium-like resonances have been named $Z_b(10610)$ and $Z_b(10650)$ [22].

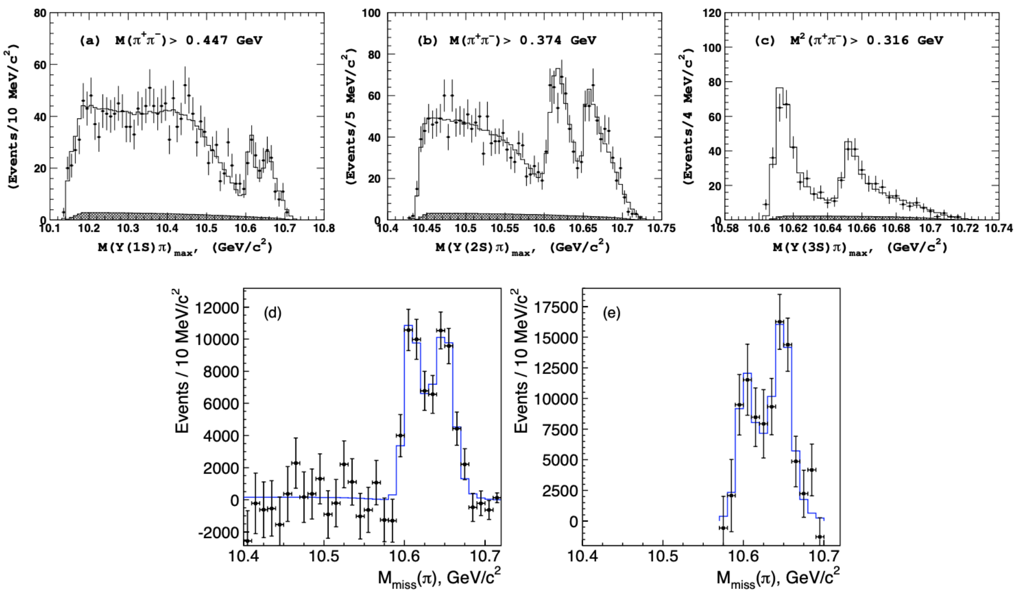

Figure 1.12: Fit results (histograms) and experimental data (points with error bars) for $\Upsilon(nS)\pi^\pm$ invariant mass distributions for $\Upsilon(5S) \to \pi^+\pi^-\Upsilon(nS)$ decays (a, b, c), and distributions of the recoiling mass against a single charged pion for $\Upsilon(5S) \to \pi^+\pi^- h_b(mP)$ decays (d, e) [23].

The mass and width values obtained using the weighed average of the values found from the five channels are as follows:

$$M_{Z_b(10610)} = (10607.2 \pm 2.0)\ \text{MeV}/c^2$$
$$\Gamma_{Z_b(10610)} = (18.4 \pm 2.4)\ \text{MeV}$$

$$M_{Z_b(10650)} = (1065.2 \pm 1.5)\ \text{MeV}/c^2$$
$$\Gamma_{Z_b(10650)} = (11.5 \pm 2.2)\ \text{MeV}$$

The statistic and systematic errors have been added in quadrature.

Being bottomonium-like states, but having a non-zero charge, these resonances must contain at least four quarks, making them manifestly exotics.

Through angular analysis, the favored quantum numbers are $J^P = 1^+$ [22], but they need to be confirmed.

Furthermore, the production of $h_b(mP)$ from the decay channels that proceed through the Z_b states accounts for the exceeding rates observed in [21].

The Belle experiment also observed the $Z_b(10610)^0$ neutral state in the decays $\Upsilon(5S) \to \pi^0\pi^0\Upsilon(nS)$, with $n = 1, 2, 3$ [24], which suggests that the $Z_b(10610)$ can be interpreted as an isospin triplet. Instead, the collected data were insufficient to establish the observation of the $Z_b(10650)$ neutral partner.

More recent analyses have shown that the mass values of these states are respectively below the $B\bar{B}^*$ threshold, for the $Z_b(10610)$, and just above the $B^*\bar{B}^*$ threshold, for the $Z_b(10650)$, which hints at an hadronic molecular structure [25].

Chapter 2

The Belle II experiment

The Belle II experiment is located at the asymmetric electron-positron collider SuperKEKB in Tsukuba, Japan. The data taking started in spring 2019 and a much larger data sample is expected to be collected compared to its precursor Belle.

The experiment operates at the center-of-mass energy range of bottomonium states and it aims to explore new physics beyond the Standard Model at the intensity frontier.

At the present time, the Standard Model is the theory that best describes elementary particles and their interactions. Many fundamental questions still remain unanswered within this theory. Belle II is one of the high-energy physics experiments designed to address these questions working at the precision frontier. In particular, the physics program is focused on the search for new physics in the flavor sector, such as CP violation and violations of lepton flavor universality in B mesons or τ leptons decays, but also performs quarkonium spectroscopy with special attention for exotic candidates.

In Section 2.1, an overview of the SuperKEKB facility will be discussed. In Sections 2.2, the Belle II detector and its several sub-detectors will be presented.

For the following sections [26] has been used as a general reference.

2.1 SuperKEKB

The SuperKEKB asymmetric e^+e^- collider is the upgrade of the KEKB accelerator located at Tsukuba, Japan. The overall configuration of the facility is shown in Fig. 2.1.

The main rings (MRs) of the collider are respectively a 7 GeV electron ring, also known as the high-energy ring (HER), and a 4 GeV positron ring, called the low-energy ring (LER).

SuperKEKB is designed to achieve the world record for instantaneous luminosity of $8 \cdot 10^{35}$ cm^{-2} s^{-1}, 40 times higher than its precursor. The goal is to collect a data sample of 50 ab^{-1} of integrated luminosity. A new peak for instantaneous luminosity of $5.105 \cdot 10^{34}$ cm^{-2} s^{-1} has been achieved in December 2024.

In order to achieve the target luminosity, a new accelerator design based on the nano-beam scheme has been adopted. The idea is to squeeze the beam size at the interaction point (IP), as shown in Fig.2.2.

SuperKEKB is a B-Factory, i.e. it is designed to produce a large amount of B mesons; indeed, it mainly operates at the $\Upsilon(4S)$ resonance, which decays for

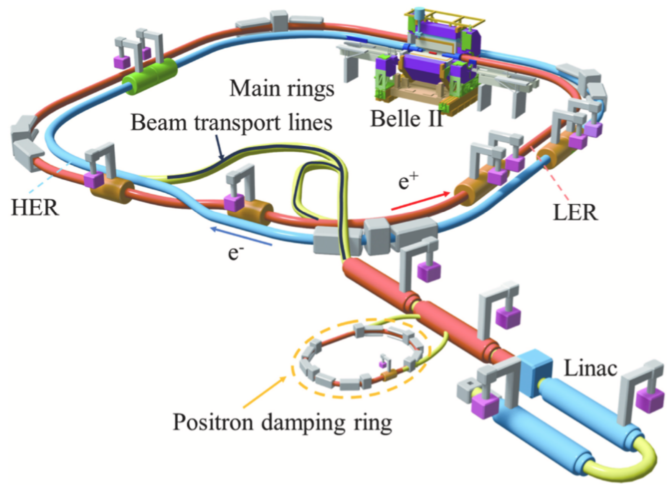

Figure 2.1: Schematic representation of the SuperKEKB accelerator complex.

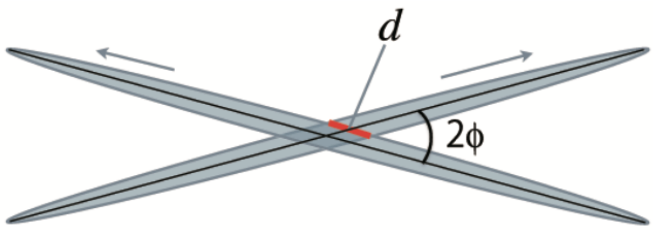

Figure 2.2: Schematic representation of the beam collisions in the nano-beam scheme; d is the size of the overlap region, considered to be the effective bunch length for the nano-beam scheme; ϕ is the horizontal crossing angle.

a large fraction into pairs of B mesons. It can also work above the $\Upsilon(4S)$, by modulating the beam energies.

The asymmetry in the beam energies is designed to provide a Lorentz boost along the axis of the detector to the B mesons produced in the collisions. This allows to extend the decay length of these particles in the laboratory frame, thus to observe the spatial separation of the B vertices.

The SuperKEKB beam energy asymmetry has been reduced compared to KEKB, from 3.5 GeV and 8 GeV for e^+ and e^-, respectively, to 4 GeV and 7 GeV. Thus, the Lorenz boost factor is also reduced from 0.42 to 0.28. This helps to mitigate the emittance growth due to the beam Coulomb scattering and the short beam lifetime caused by the Touschek effect.

2.2 Belle II detector

As a consequence of the upgrade of the KEKB facility, the detector also needed to be updated to be able to face the new challenges posed by the higher instant luminosity. With the new SuperKEKB accelerator, both signal and beam-background rates are expected to increase, thus an upgrade of the Belle detector was necessary to obtain a comparable or better performance in Belle II.

The Belle II detector is a general purpose spectrometer, 8 meters wide and 8 meters high. The design of the detector is asymmetrical, to account for the Lorenz boost provided to decay products by the asymmetry in the collision beams.

A schematic representation of the Belle II detector design is shown in Fig. 2.3.

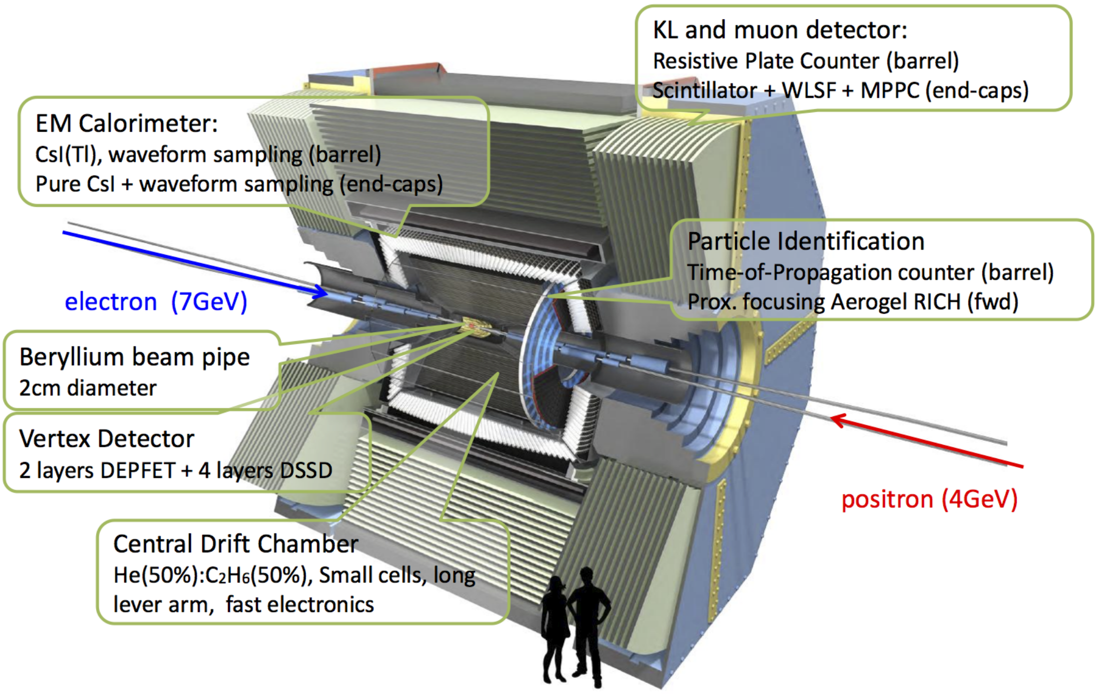

Figure 2.3: Schematic representation of the Belle II detector.

The detector is made of different sub-detectors components arranged in cylindrical layers around the beam pipe.

The beam pipe is made of two thin beryllium walls, and around the interaction region a system of focusing magnets is also present.

The innermost detector is the Vertex Detector (VDX), which consists of two silicon-based sub-detectors: the Pixel Detector (PXD), made of two layers of pixel sensors, and the Silicon Vertex Detector (SVD), made of four layers of double-sided silicon strip sensors. These are used to reconstruct the charged particles' tracks in order to find the decay vertex position. Next, there is the Central Drift Chamber (CDC), the central tracking detector used to measure the dE/dx and momenta of charged particles. Then, there are the Time-Of-Propagation (TOP) and the Aerogel Ring Imaging Cherenkov counter (ARICH) systems, located respectively in the barrel and forward endcap areas and used for particle identification. Next are the electromagnetic calorimeter (ECL), which detects both neutral and charged particles, and the K_L and Muon Detector (KLM), used to identify muons and K_L mesons.

A superconducting solenoid, located between the ECL and the KLM, provides a 1.5 T magnetic field directed along the symmetry axis of the CDC. The field is overall homogeneous in the whole detector, with only 1% order variations in the tracking volume.

All of these components will be discussed in detail in the following sections.

2.2.1 Vertex Detector (VXD)

The goal of the Vertex Detector is to precisely reconstruct the decay vertex positions. In order to cope with the significantly increased background and the higher occupancy due to the SuperKEKB upgrade, the design of this detector needed to be improved compared to the one used by the previous experiment.

In Belle II, the beam pipe consists of two thin beryllium walls with a liquid paraffin coolant between. The inner wall is covered with a thin layer of gold to protect the vertex detectors from synchrotron radiation [27]. The inner radius has been reduced to 10 mm, allowing the vertex detectors to be arranged closer to the IP to improve the vertex resolution.

The VXD is made of two complementary silicon-based sub-detectors, the Pixel Detector (PXD) and the Silicon Vertex Detector (SVD), which will be discussed in the following sections. A schematic view of these can be found in Fig. 2.4.

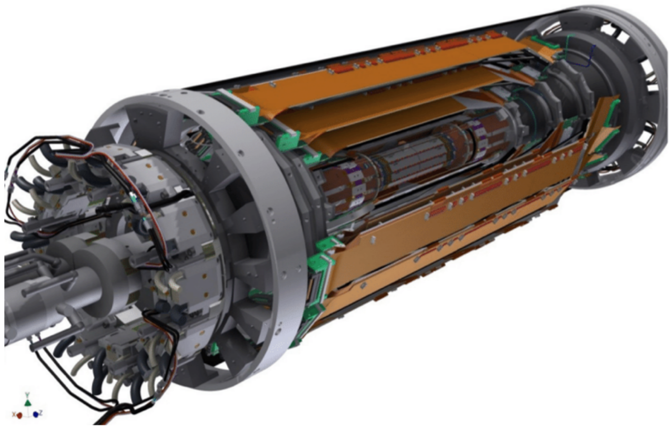

Figure 2.4: Schematic representation of the Vertex Detector (VXD).

The geometrical acceptance of the detector covers a range of polar angles θ between 17° and 150°, respectively, in the forward and backward directions, and the total azimuthal angle ϕ range.

Pixel Detector (PXD)

The innermost detector is the Pixel Detector (PXD), which is made of two layers of pixel sensors based on DEPFET (DEPleted Field Effect Transistor) technology.

Sensors are arranged in "ladders", modules each made of two pixel matrices mounted on a self-supported all-silicon structure, as shown in Fig. 2.5.

The first layer has a radius of 14 mm measured from the beam axis and is composed of 8 ladders. The outer layer, instead, has a radius of 22 mm and is made of 12 ladders. The ladders are arranged in a windmill structure around the

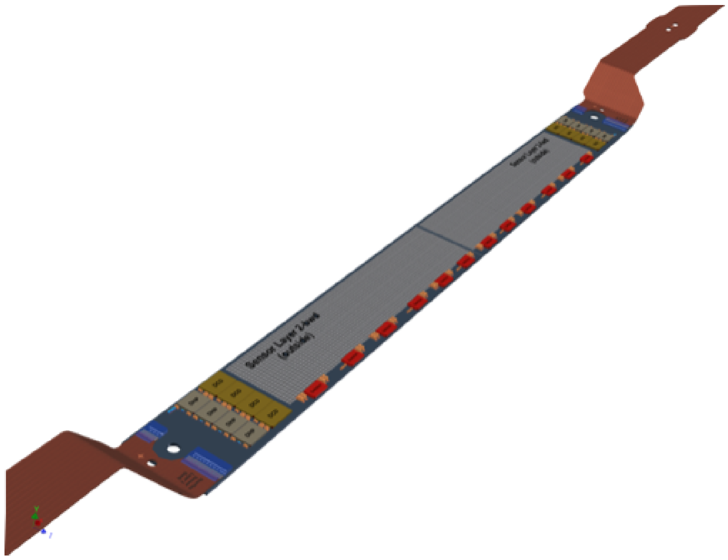

Figure 2.5: Schematic representation of a ladder.

beam pipe.

Until 2023 (run1) only 10 ladders were installed and used during data collection; during the long shutdown (LS1) the remaining ones were installed to be used for run2 (2024), for a total of 20 ladders. The run1 configuration for PXD is shown in Fig. 2.6.

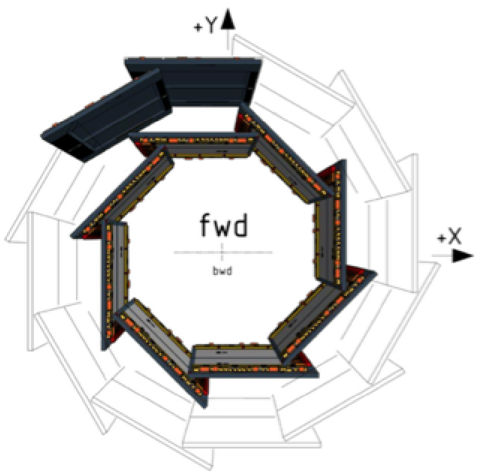

Figure 2.6: Schematic representation of the PXD run1 configuration used for data collection.

The pixels have different pitches in the z direction, from 55 μm to 85 μm, to achieve a finer granularity near the interaction point [27].

The DEPFET sensors are monolithic all-silicon structures that combine detection and amplification within the same device. For this reason, this technology allows to use very thin sensors, down to 50 μm, minimizing multiple scattering and obtaining high signal-to-noise ratio. Support structures are not needed in the active region of the detector and using just air cooling is sufficient, due to the very low power consumption.

The readout electronic system, which instead requires active cooling, is mostly placed outside the acceptance region to minimize the material budget. It is made of 3 different ASICs (Application-Specific Integrated Circuits) directly bump-bonded on the silicon substrate of the ladder.

Silicon Vertex Detector (SVD)

The Silicon Vertex Detector (SVD) is composed of four layers of double-sided silicon strip detectors.

The radii of the layers range from 39 mm to 135 mm, measured from the beam pipe.

The layers, from the innermost to the outermost, consist of 7 to 16 electrically and mechanically independent ladders, with 2 to 5 sensors each [28].

Every layer has a barrel-shaped part made of rectangular sensors, while only the three outer layers have a lamp-shade geometry made of trapezoidal sensors. The asymmetric setup of the detector accounts for the forward boost of the center-of-mass frame, minimizing the material budget encountered by the particles and maximizing the angular acceptance [27].

A schematic representation of the SVD geometry is shown in Fig. 2.7.

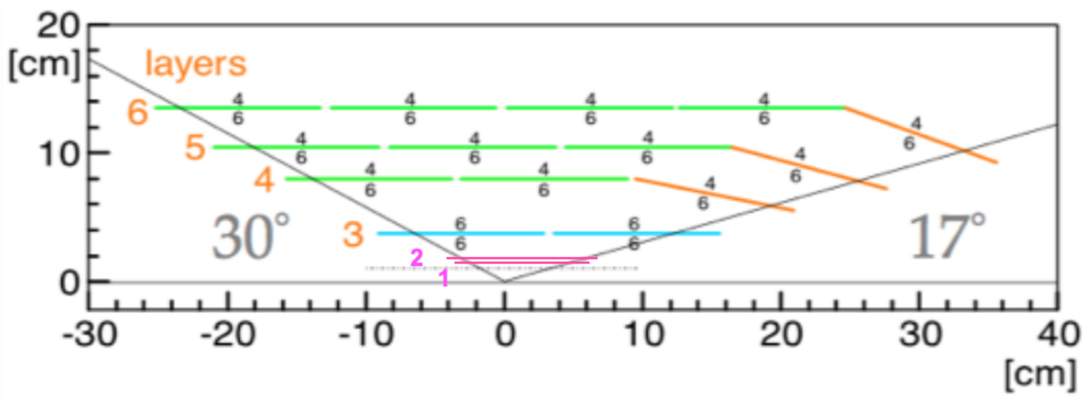

Figure 2.7: Schematic representation of the PXD + SVD geometry. Layers 1 and 2 (fuchsia) represent the PXD; layers 3 to 6 represent the SVD. Blue and green are the rectangular sensors, the orange ones have the trapezoidal geometry instead. The numbers above and below each SVD sensor show the number of the readout chips.

Ladders belonging to the same layer are often overlapping, to facilitate the alignment procedures.

The SVD provides two-dimensional spatial position information, since the strips on each side of the layers are placed orthogonally.

2.2.2 Central Drift Chamber (CDC)

The Central Drift Chamber of the Belle II detector is used for the reconstruction of charged tracks and to measure particle momenta. Furthermore, it provides particle identification (PID) information, by using dE/dx measurements, and is also used as a trigger for charged particles.

The detector is a large volume drift chamber, with outer radius of 1.1 m, containing about 50000 both sense and field wires, which define drift cells sized between 1 and 2 cm.

The 14336 sense wires are placed to form 56 layers, which are then arranged into 9 superlayers, as shown in Fig. 2.8. The innermost is made of 8 layers, while the others consist of 6 layers each. In particular, the inner layer has smaller drift cells to cope with the higher background expected at smaller radii. The wires of each superlayer alternate between axial "A" and stereo "U, V" orientation, with a total configuration of "AUAVAUAVA". Axial wires are aligned with the solenoidal magnetic field along the z-axis, while stereo wires are skewed by an angle between 45.4 and 74 mrad, both in positive and negative direction, which changes sign between "U" and "V" layers.

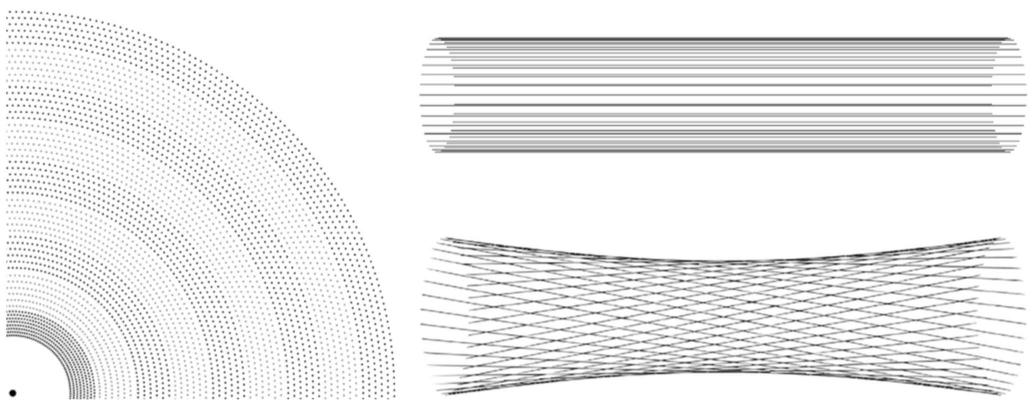

Figure 2.8: Schematic representation of the CDC sense wires configuration. On the left, a slice of the transverse plane projection. On the right, a scheme of axial (top) and stereo (bottom) wires configurations. In the latter the skew angle is exaggerated for visualization purposes.

The geometrical acceptance of the detector is the same as for the VXD, covering a range of polar angle θ from 17° to 150° and the total ϕ range.

The gas used in the CDC is a mixture of $He - C_2H_6$ (helium - ethane) with a 50:50 ratio. This has been found to be the best compromise to achieve good momentum resolution for tracking performance and good dE/dx resolution necessary for particle identification.

The drift time information provided by the CDC is affected by the left/right ambiguity, since the same time can be measured for particles passing at equal distance on either side of the wire cell [27].

The measurements obtained from both axial and stereo wires can be merged to reconstruct the full 3D helix track of the particle.

2.2.3 Time-of-Propagation counter (TOP)

The Time-of-Propagation (TOP) counter [29] is a detector located in the barrel region of the Belle II spectrometer, which has been designed to upgrade the particle identification (PID) system and, in particular, to improve the separation between kaons and pions.

The detector consists of 16 modules arranged in a barrel structure outside of the CDC, with radius of 1.2 m. Each module is made of a 2 cm thick, 45 cm wide and 2.7 m long quartz bar. In the backward region of the bar a small prism is located, which serves as a volume expansion and a light guide. Instead, in the forward region, there is a reflective mirror. At the backward end of the quartz bar an array of Micro Channel Plate Photo Multiplier Tubes (MCP-PMTs) is located, which allows to detect single photons with extreme timing precision. A schematic representation of the TOP module is shown in Fig. 2.9.

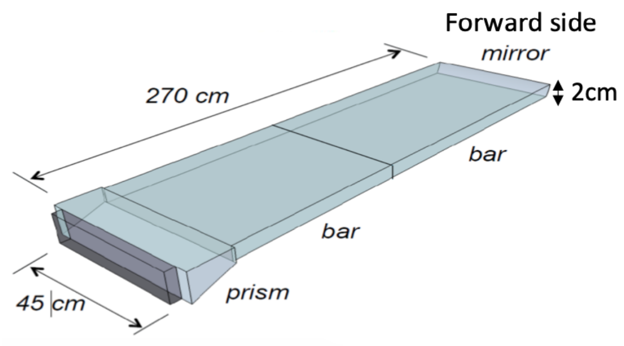

Figure 2.9: Schematic representation of a TOP module.

The quartz bars act as both Cherenkov radiators and photon collectors. The Cherenkov light propagates inside the bar through internal reflection until it reaches the PMTs, which measure the time of propagation of photons with high precision. Charged particles crossing the quartz bar radiate Cherenkov light characterized by a specific angle θ_c with respect to the incident particle direction, which depends on the refractive index of the medium and the masses and momenta of the particles. Different particles will have different Cherenkov angles, thus different paths, and will eventually be detected at different positions of the PMTs array and at different times, as shown in Fig. 2.10.

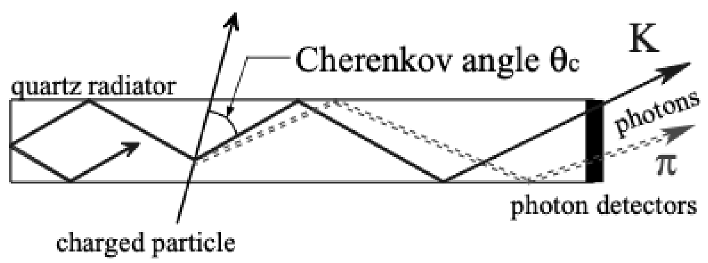

Figure 2.10: Schematic side-view of a TOP module and different internal reflections of Cherenkov photons from kaons and pions.

As a consequence, the Cherenkov image can be reconstructed using the (x, y) information related to the position where photons are detected, and the precise time measurements obtained by the MCP-PMTs.

2.2.4 Aerogel Ring-Imaging Cherenkov detector (ARICH)

Particle identification is also provided by another detector located in the forward endcap region of the Belle II spectrometer, the Aerogel Ring-Imaging Cherenkov counter (ARICH) [30]. Its main goal is to separate kaons from pions in the full kinematic range of the experiment, from about 0.5 to 4.0 GeV/c.

The detector is made of an aerogel radiator, an expansion volume and an array of position-sensitive photon detectors.

Charged particles crossing the radiator emit Cherenkov light at a specific angle θ_c, which depends on the refractive index and the velocity of the particle. Therefore, particles can be identified by reconstructing the Cherenkov ring image and also using the charged particle direction information provided by the tracking system.

Photons are collected in a large area array of photon detectors, which allows to measure the two-dimensional ring image with high resolution.

The working principle of ARICH is shown in Fig. 2.11.

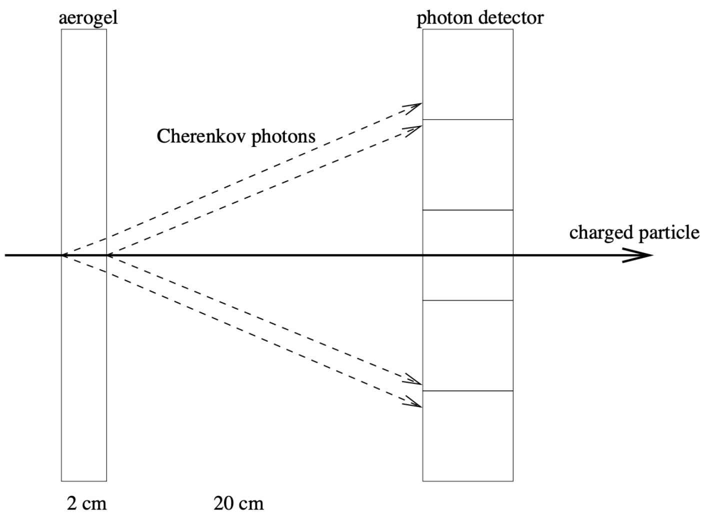

Figure 2.11: ARICH working principle.

To increase the photon yield and improve the angular resolution, two stacked aerogel layers with different refractive indices, $n_1 = 1.045$ and $n_2 = 1.055$, are used.

2.2.5 Electromagnetic Calorimeter (ECL)

The Belle II electromagnetic calorimeter (ECL) serves several purposes, such as photons detection and precise measurement of their energy; but also particle identification for electrons and generation of trigger signals.

The ECL is placed inside the 1.5 T magnetic field generated by the superconducting solenoid, as shown in Fig. 2.12.

It is a homogeneous calorimeter with high granularity, made of 8736 CsI(Tl) scintillating crystals. The light in each crystal is detected by two independent photodiodes, each coupled with a charge-sensitive preamplifier mounted on the rear face of the counter. The readout electronics also includes a flash ADC followed by a wave form analysis (WFA) realized in FPGA [31]. The update, compared to the previous Belle calorimeter, was necessary to cope with the expected 100 times higher rates.

The crystals are installed in a multi-cells support structure, covering both the barrel part and the endcaps, and are arranged to point toward the interaction point. The thickness of the crystals is of 30 cm, while their transverse dimension varies depending upon their polar angle positions, with average values of 6x6 cm^2.

The ECL covers a polar angle region between 12° and 155°, with the exception of two small 1° gaps between the barrel and the endcaps.

2.2.6 K_L and Muon detector (KLM)

The largest and outermost Belle II subdetector is the K_L and Muon detector (KLM).

As the name suggests, its main goal is to identify muons and K_L mesons. Muons usually travel through the KLM, leaving an almost straight trail of hits. K_L mesons, instead, interact in the ECL or with the iron plates of the KLM, creating a hadronic shower.

The detector is located outside of the superconducting solenoid, as shown in Fig. 2.12, and consists of several layers alternating thick iron plates and active elements. The iron structure serves as the magnetic flux return for the solenoid, as well as providing additional 3.9 interaction lengths of material, beyond the 0.8 interaction lengths of the ECL, in which K_L mesons can create a hadronic shower.

In the gaps between the iron plates are placed active particle detectors. These have been partially updated compared to the previous Belle experiment, whose active KLM elements were only RPCs. In particular, in the endcaps and the inner layers of the barrel, RPCs have been replaced by scintillators strips containing wavelength-shifting fibers read by silicon PMTs, to cope with the expected increased background.

The overall polar angle coverage of the KLM ranges from 20° to 155°.

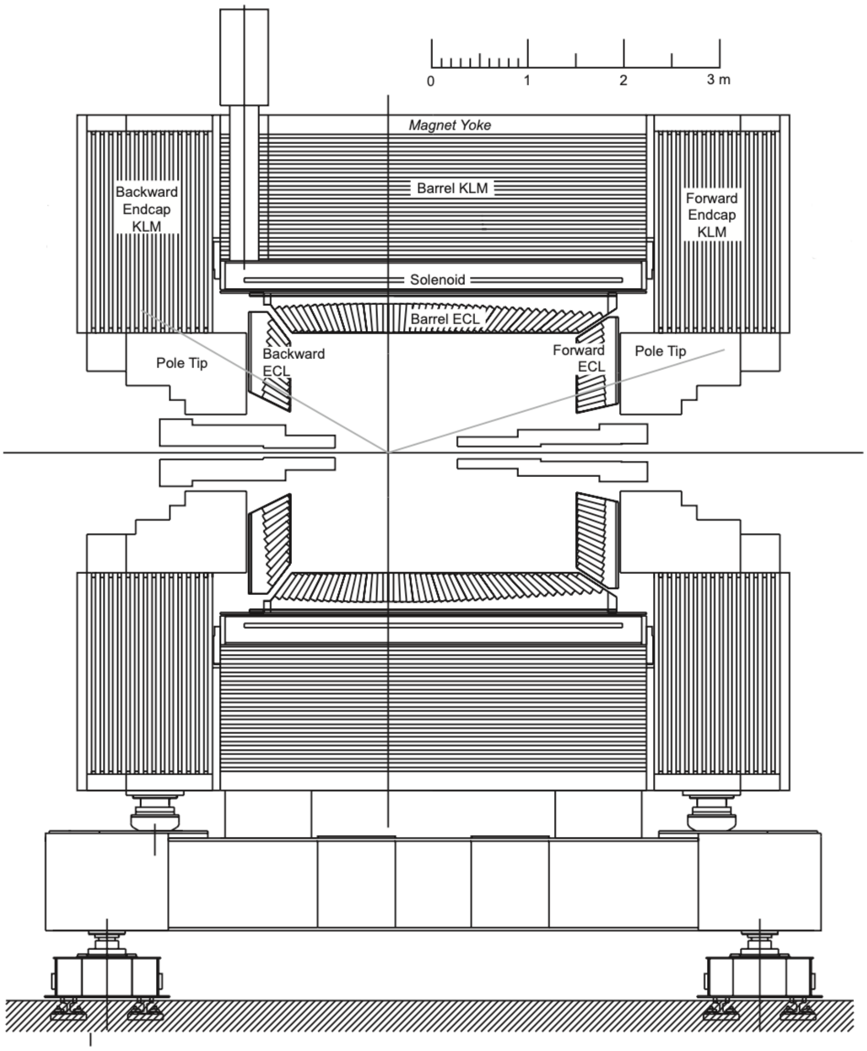

Figure 2.12: Side view of the ECL + KLM. Gray lines mark the nominal polar angle acceptance of the Belle II detector.

2.2.7 Trigger system

At SuperKEKB, particle bunches can cross in the interaction region up to every 4 ns, but most of the time no hard interaction takes place or collisions result in processes not interesting for the physics program, such as Bhabha scattering. Therefore, before storing the events, these needs to be filtered by the trigger system.

This is composed of the hardware based Level 1 Trigger (L1) and the software based High Level Trigger (HLT), and it is the upgrade of the previous Belle trigger system in which all components have been replaced with new technologies based on Field Programmable Gate Arrays (FPGA).

The Belle trigger was made of several sub-trigger systems, each one processing the information collected by the corresponding detector, and one global final decision logic, which reads the sub-systems information and issues the final decision. The same concept has been used for the L1 trigger, as shown in Fig. 2.13.

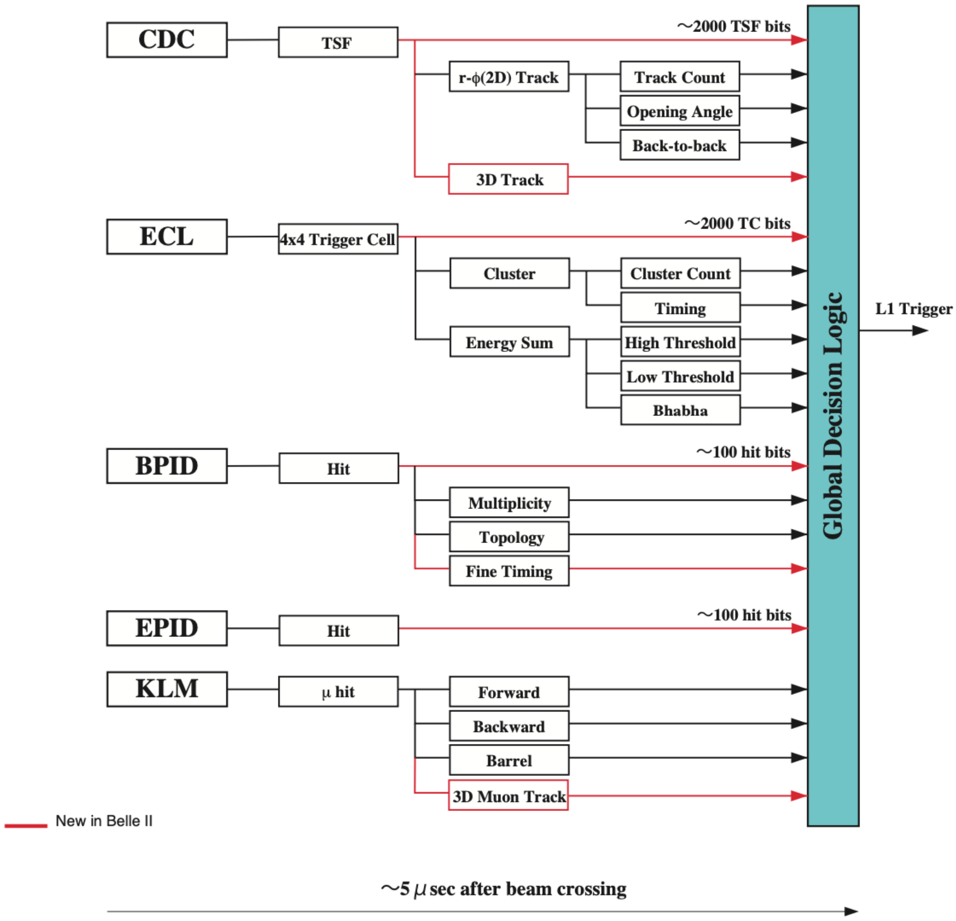

Figure 2.13: Scheme of the Belle II L1 Trigger.

The HLT, instead, consists of a computing cluster which performs an immediate full event reconstruction using the same software employed in offline data analysis. Based on the result of this reconstruction, events are classified and either saved into an offline storage hard disk drive or discarded.

Chapter 3

The Belle II Software

The new SuperKEKB accelerator and the goal of achieving higher instant luminosity pose new challenges for the Belle II experiment. As a consequence, not only the detector, but also the software needed to be updated. In fact, due to an increase in both signal and beam-background rates, an extremely high data volume is expected to be collected. Therefore, a highly performing software capable of processing the newly collected data while also maintaining high efficiency and good resolution for particle reconstruction is needed.

In Section 3.1 of this chapter, the Belle II software will be presented. In the following sections 3.2 and 3.3 the MC simulation process and the different steps of reconstruction will be respectively discussed.

For this chapter, the official Belle II software documentation [32] has been used as a general reference.

3.1 basf2

The official Belle II software is named basf2 [33], which stands for "Belle II Analysis Software Framework".

It is used in every step of the data processing chain, such as the generation of simulated data and their reconstruction, but also to unpack real raw data. Instead, basf2 is not used for the final steps of the analysis, such as creating histograms and fitting distributions, which are generally performed using the ROOT analysis framework or the Matplotlib Python library.

The standard basf2 data processing chain is made up of a sequential arrangement of *modules* stored in a *path*, as shown in Fig. 3.1.

A *module* is the smallest block of the framework, which consists of a code usually written in C++ that performs a specific task. This ranges from reading data from a file to full detector simulations or tracking. A *path* is the container in which modules are arranged to form a linear chain. In particular, the chosen modules and the order in which they are organized depend on the task that the user needs to perform.

During the data processing chain, the modules stored in a path are executed one at a time, from first to last, following the order in which the have been organized. Modules can also have *conditions* attached to them to eventually modify the processing flow based on the output of each module.

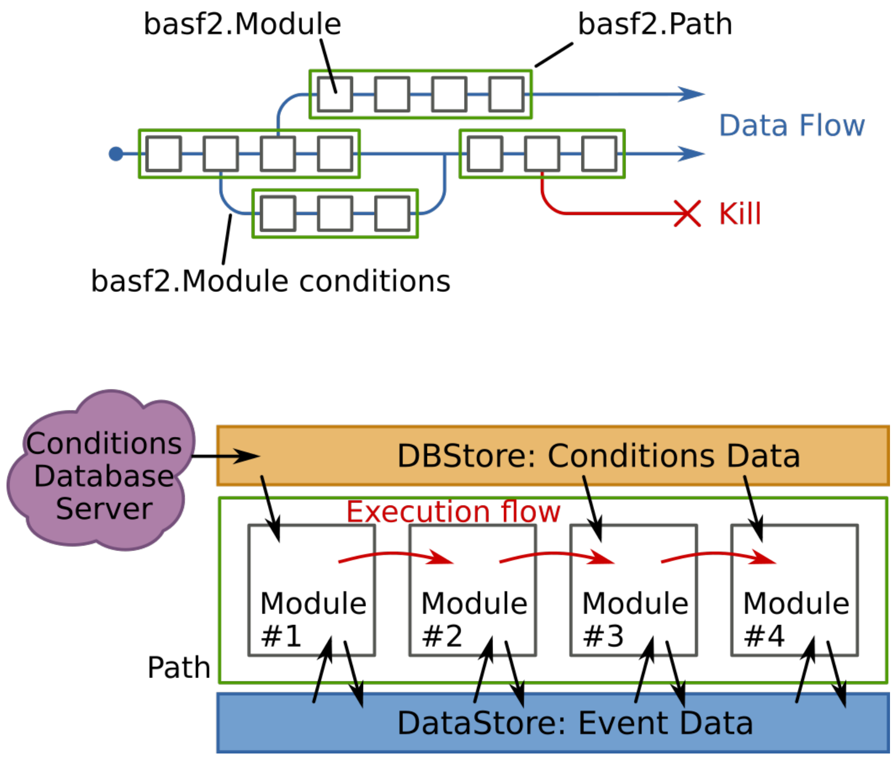

Figure 3.1: Schematic view of the basf2 data processing chain.

Modules process *event data* saved in the *DataStore*, a common storage to which each module has read and write access. Furthermore, there are non-event data, also called *conditions data*, such as settings or calibration information, which are loaded from a central conditions database server (CDS) into another storage called the *DBStore*.

To define the preferred data processing chain, the user needs to write a Python3 script, called *steering file*. In each script, the first thing that needs to be done is to create a new path; then, after all the required modules have been loaded and added in the correct order, the processing can start.

3.2 Monte Carlo simulations

A very important step of every physics analysis consists of performing Monte Carlo (MC) simulation studies of the events of interest. The aim of simulations is to reproduce as closely as possible what happens in the collisions and to understand the response of the detector. These samples can be used for performance studies and also as a comparison to confirm that what is observed in real event data is not some sort of artifact, but is actually related to a physical process.

The production of Monte Carlo samples can be divided into two parts: the generation and the simulation of the event.

The first step is related to the generation of the physical process of interest. After the initial conditions of the collider have been fixed, a number of particles are generated following a specific physical model, such as the Standard Model or more advanced ones. For each particle, the position and four-momentum information is created. In basf2 different physics generators are available, such as *EvtGen* [34], designed for the simulation of B and D decays, which is the one that will be predominantly used in this work.

The second step of the MC process consists of simulating the propagation of particles and their interactions with all the different detector components. The detector response to these processes also needs to be simulated. This is performed using the open-source toolkit *Geant4* [35] (GEometry ANd Tracking), which has been designed to accurately simulate the passage of particles through matter. This external package allows to reproduce the detector layout, including both the materials from active and non-active regions. It is also used to simulate the propagation of particles and all the processes through which they can interact with the different materials, such as ionization, Bremsstrahlung, Cherenkov radiation, and others. Furthermore, it handles the detector response.

3.3 Reconstruction

All the information coming from the various detectors, gathered from data or MC simulation, has to be processed to reconstruct the events. The goal is to retrieve particles initial positions and four-momenta as correctly as possible.

However, this process faces different challenges. For example, hadronic interactions often create short-lived particles that decay before being detected. Furthermore, detectors have some intrinsic noise, which might create random signals that are not related to actual particles. In addition, noise generated by the interaction of beam electrons or positrons with each other or with other components of the accelerator structure, called the beam background, has to be considered.

Therefore, the information provided by the sub-detectors is combined to identify the most likely particle candidates, which then can be further evaluated in following analyses.

Both MC simulations and data use the same reconstruction algorithms. In particular, for MC events the additional *MC truth* information can be retrieved, since the true particles participating in the interactions are well determined.

The main steps performed for reconstruction will be discussed in the following sections.

3.3.1 Clustering

The first step of reconstruction is called *Clustering* and consists of identifying all hits created by the same particle and combining them.

A simple example related to PXD is shown in Fig. 3.2.

When a particle crosses the detector, a signal is expected in one of the pixels. If the particle passes through the detector with a small angle or between the pixel boundaries, multiple pixels will record a signal related to the same particle.

The aim of clustering is to group neighboring pixels, also taking into account the intrinsic noise of the detector. Then the properties of these clusters can be evaluated, such as size, shape or center. For example, if the detector has an analog readout, the amount of measured charge per pixel is used to evaluate the center of the cluster with a weighted mean.

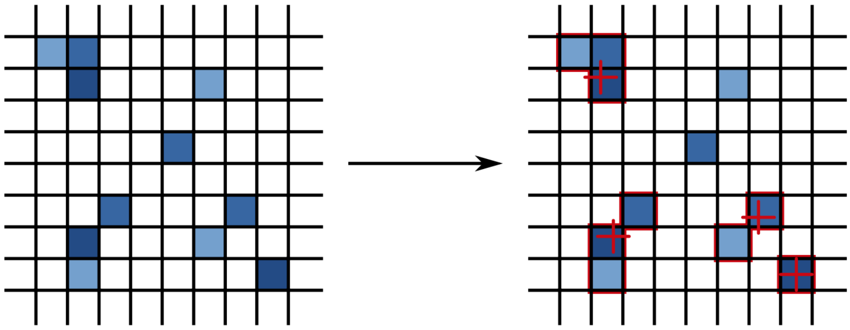

Figure 3.2: Example of 2D clustering in pixel detector with analog signals. The red cross identifies the center of the cluster evaluated with a weighted mean.

3.3.2 Tracking

One of the main steps of reconstruction is the *Tracking*. The goal is to identify the trajectories followed by charged particles, also named *tracks*, using the information provided by tracking detectors, i.e. PXD, SVD and CDC, discussed in Sec. 2.2.1 and 2.2.2.

The tracking software is built using basf2; therefore, it has a modular design which allows to split the process into several sub-tasks performed by independent and interchangeable modules. Each step employs a specific algorithm optimized to deal with the different tracking sub-detectors [27]. The software uses several global and local track-finding algorithms and also multivariate methods.

The tracking process can be divided into two main steps, the *Track Finding* and the *Track Fitting*, which will be discussed in the following subsections. First, a brief overview of track parametrization will be presented.

Track parametrization

The Belle II software uses the following x, y, z coordinate system, shown in Fig. 3.3.

- x*-axis*: horizontal and pointing toward the outside of the accelerator tunnel, roughly northeast;

- y*-axis*: vertical and upward;

- *z-axis*: along the solenoid axis, roughly parallel to the direction of the electron beam;

Furthermore, ϕ is the azimuthal angle around the z-axis and θ is the polar angle with respect to the z-axis.

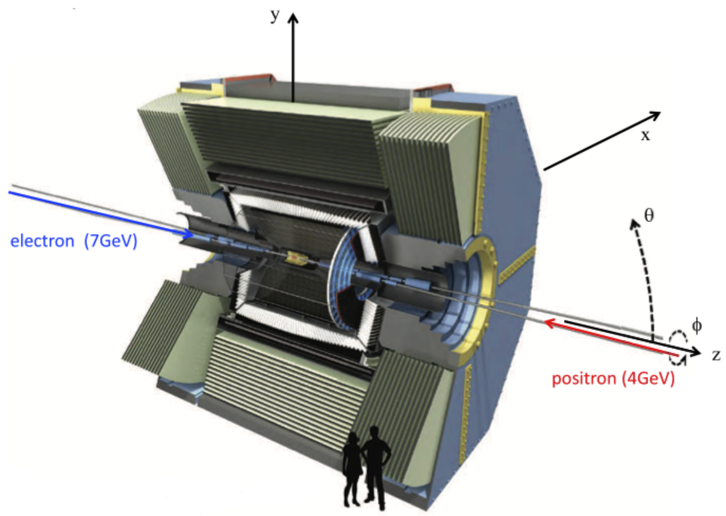

Figure 3.3: Schematic view of x, y, z coordinates used in Belle II software.

Tracks of charged particles in a homogeneous magnetic field can be described by a helix parametrization [27], which is characterized by 5 total parameters, computed at the point of closest approach (POCA) to the z-axis, as shown in Fig. 3.4:

- d_0: the signed distance of the POCA projected on the x-y transverse plane;
- z_0: the signed distance of the (POCA) along the z-axis;
- ϕ_0: the angle defined by the track transverse momentum at the POCA and the x-axis;
- ω: the inverse of the track curvature radius R, signed with the particle charge;
- $tan\lambda$: the tangent of the dip angle, defined by the momentum at the POCA and the transverse plane.

The helix is also represented by a straight line in the z-s space, where s is the path length of the circular trajectory in the transverse plane.

Track Finding

The aim of the first part of the tracking process, named *Track Finding*, is to identify patterns of hits measured in tracking detectors that belong to the same track.

The track finding process can be summarized as follows :

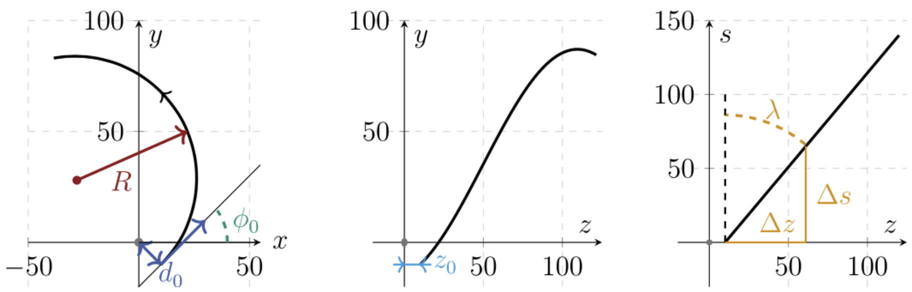

Figure 3.4: Schematic representation of the trajectory projection with the 5 helix parameters in the x-y (left), z-y (center) and z-s (right) planes. Dimensions are in cm.

1. The first step uses the information provided by the CDC and consists of removing hits which are induced by background effects. These are usually isolated in small clusters compared to the ones associated to charged particles which instead have neighboring hits. To filter out background hits a boosted decision tree (BDT) is employed [36].

   The remaining hits in the CDC are then processed independently by both a global track finder algorithm, based on the Legendre transformation, and a local track finder, using a Cellular Automaton method.

   Then, track candidates found by these algorithms are merged to prevent clones.

2. Next, the previously found CDC tracks are combined with SVD clusters using a *Combinatorial Kalman Filter* (CKF) (which will be discussed later).

3. The remaining SVD hits are then processed with a Standalone SVD track finder that employs a Sector Map algorithm.

4. The fourth step has been recently added to the tracking chain and consists of using the CKF to extrapolate tracks found in the previous step (SVD Standalone) into the CDC, to eventually attach some of the remaining CDC hits.

5. All the track candidates found until this step are then combined.

6. In the final step of track finding, PXD hits are attached to track candidates found in SVD and CDC, employing a CKF. In fact, PXD has a very high occupancy; therefore, PXD hits are not used in the initial stages of pattern recognition. Instead, SVD and CDC tracks are extrapolated into the innermost detector and compatible PXD hits are assigned to them [36].

A more detailed description of the algorithms cited previously, such as the Cellular Automaton, the Legendre transformation based algorithm and the Sector Map, can be found in [27].

A summary of the steps followed for track finding is shown in Fig. 3.5.

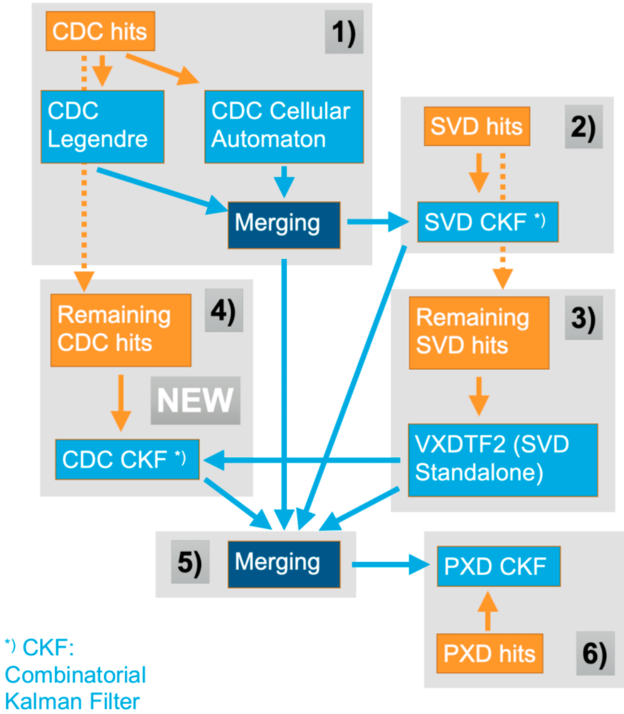

Figure 3.5: Schematic representation of the track-finding process.

The *Combinatorial Kalman Filter* is the iterative local algorithm employed in steps 2, 4 and 6 of the track finding chain, to extrapolate candidate tracks to other detectors and search for compatible hits. These are the steps that are followed by CKF [27]:

- The algorithm starts with a seed estimate of the track parameters and their uncertainties.
- From the seed point (K_{i-1}), the track is extrapolated to the next detector plane (e_i). The CKF extrapolation takes into account both the material budget, to compute the energy loss, and the propagation in non-uniform magnetic field (Runge-Kutta-Nyström method).
- If a measured hit (X_i) is found close to the extrapolated point, this is added to the track. Hit candidates are determined based on position and uncertainties of the track. If multiple hit candidates are found, the entire track is duplicated and treated independently until the end of the process, when the best one will be selected.
- Furthermore, an average point (K_i) between the one found by extrapolation (e_i) and the measured hit (X_i) is evaluated. This will be used as the new seed for the following extrapolation.
- The previous steps are then reiterated for extrapolation to the next detector plane.

A schematic representation of the CKF working principle is shown in Fig. 3.6.

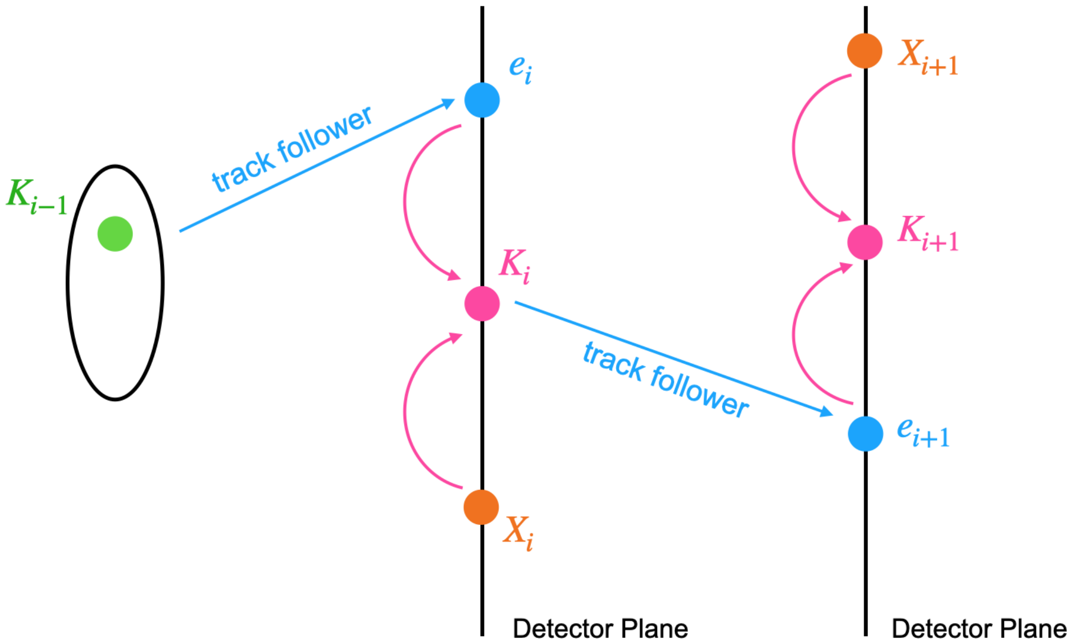

Figure 3.6: Schematic representation of the CKF working principle. In green the seed point estimated by a previous pattern recognition algorithm; in blue the hits obtained from extrapolation; in orange the measured hits; in pink the average points found by the Kalman Filter.

This mechanism can be repeated multiple times to improve the quality of the track candidate.

After the CKF process has been completed, an additional *backward smoothing extrapolation* can also be performed to update the seed starting point.

Track fitting

The next step of tracking is named *Track Fitting* and consists of fitting track candidates to retrieve the final trajectory parameters and determine the positions and momenta of the particles to the IP as precisely as possible.

The global fit is performed using the *GENFIT* [37] open source toolkit, which employs a Kalman Filter algorithm improved by a *Deterministic Annealing Filter* (DAF). The latter allows to reject hits that have been wrongly assigned by pattern recognition to the tracks, the so-called outliers, which instead belong to the background or to a different track. The DAF assigns a progressively lower weight to hits further away from the track. Reiterating the algorithm multiple times, the weight of outliers decreases each time, until they are removed.

To better estimate the track parameters, the fit takes into account the inhomogeneity of the magnetic field and the energy loss of particles in the tracking region. For this reason, it is important to assume the correct particle hypothesis. In fact, using the wrong particle in track fitting could create a systematic bias on the estimation of the track parameters [38]. For low momentum particles below 1 GeV/c this effect is important, while for higher energies is negligible. Therefore, using the correct hypothesis is necessary to achieve high performance results. In

Belle II, each track is fitted using the π, K and p hypotheses, as a compromise between performance and consumption of computing resources.

In the end, the fit results are stored to be used in physics analyses.

Flip and Refit Algorithm

The *Flip and Refit* is a new algorithm that can be used at the end of the tracking chain, to further improve the quality of tracks after the finding and fitting steps. It has been implemented since *release8* of the Belle II software, which has been used for the first part of this work. This refining step can only be applied if the PXD information is used for the reconstruction.

Low momentum tracks in the transverse plane are often correctly found, which means that the correct hits have been assigned to the track but, instead, the charge assignment might be wrong. In fact, the same hit pattern might belong to both an in-going particle track or to an out-going track with the opposite charge.

This new step aims to correct the sign of these tracks and thus improve the overall quality of track parameters.

The algorithm follows three steps:

1. Firstly, *candidate tracks* that may have the wrong charge assignment are selected based on low-level variables, such as the number of degrees of freedom of the track fit or the number of hits on the tracking detectors associated with the track. This first step is performed using a Multivariate Analysis (MVA).

2. The selected tracks are then flipped and refitted. This means that the same hit pattern is considered but the charge, momentum and starting point of the track are reversed. Then the new track is fitted again.

3. In the end, the fit results obtained from the original and the flipped tracks are compared using another MVA, to evaluate which is the best one between the two. Then a new list of candidate tracks is created to be used for analysis.

The two MVAs have been trained on simulated events.

The performance of this new algorithm will be studied in detail in Section 5.4.

3.3.3 Particle Identification

After the tracks have been reconstructed, the likelihood that each track belongs to a different particle can be evaluated by checking the information provided by the PID detectors. These likelihood values are then attached to the track information and available to be used later during the analysis.

Particle identification is performed differently for charged and neutral particles. For charged hadrons, the detectors employed for PID are mainly TOP and ARICH, but also the information related to specific ionization retrieved from the CDC is used. The ECL instead provides the main information to identify electrons, while the KLM is used for muons.

PID for neutral particles consists of identifying photons, π_0 and K_L^0. Photons and neutral pions identification is based on the information obtained from the ECL, while for K_L^0 both the ECL and KLM are employed.

The working principles and functions of these detectors have already been discussed in detail in Section 2.2.

In this work no PID information will be used.

3.4 Offline Analysis

After the reconstruction is completed, all retrieved information related to charged tracks and neutral clusters (not discussed in this work) are saved on the so-called *mdst files*, namely "mini data-summary table". These files contain a list of post-reconstruction data-objects, which provide all the necessary information for analysis. Mdst files are based on the ROOT file format, however to unpack information the use of the basf2 framework and its *Analysis* package is mandatory. This step is performed running Python3 scripts, named *steering files*, on these mdst. In this way different analysis tasks can be performed, such as applying selection cuts on the samples, creating lists of reconstructed candidate particles and their variables, but also performing kinematic or vertex fits. At the end of each steering file, the obtained information is written out in the so-called *ntuples* and saved onto a ROOT output file.

These files can then be used to perform the final steps of the analysis, such as creating histograms or fitting distributions. This can be done using the ROOT analysis framework through C++ macros, but also using Jupyter Notebooks.

Chapter 4

Analysis overview

The aim of this work is to study the $\Upsilon(10753) \to \pi^+\pi^- h_b(1P)$ decay.

The production of the $h_b(1P)$ state can occur through a direct pure-phase space transition with the emission of a charged pion pair. However, this process is expected to be suppressed since it would involve the spin-flip of the heavy b quark, thus violating the Heavy Quark Spin Symmetry (HQSS). This symmetry implies that in the direct decay of a heavy quarkonium state with spin S, only lower-lying heavy quarkonia with the same spin S can be produced. Nevertheless, this rule can be overcome if multiquark intermediate states are involved in the decay chain, allowing for transitions to the final-state heavy quarkonia with a different spin S' [39].

The Belle collaboration reported the observation of unexpected high rates for the $\Upsilon(5S) \to \pi^+\pi^- h_b(mP)$ decays, with $m = 1, 2$ [21]. The exceeding rates were justified by also taking into account the processes in which the $h_b(mP)$ states are created from the decay of the Z_b intermediate charged state, since these transitions are not affected by spin-flip suppression.

In fact, in the direct transition, going from a triplet to a singlet spin state, a flip of the spin of the heavy quark is necessary; instead, it has been found that the $b\bar{b}$ pair within the $Z_b(10610)$ and $Z_b(10510)$ resonances is a mixture of a spin-triplet and a spin-singlet of equal amplitudes and orthogonal phases [40]. For this reason, the transition that proceeds through the charged state is not suppressed.

In analogy, the $\Upsilon(10753) \to \pi^+\pi^- h_b(1P)$ decay is also expected to be observed through the following channel: $\Upsilon(10753) \to \pi^\pm Z_b(10610)^\mp \to \pi^\pm\pi^\mp h_b(1P)$.

Both decay chains are shown in Fig. 4.1.

If the transition through an intermediate charged state takes place, a signal is expected to be found in the recoil mass distribution of the single pion around the mass value of the $Z_b(10610)$ state. The process could also be searched by looking at the energy-dependent cross section of the process $e^+e^- \to \pi^+\pi^- h_b(1P)$, with energies around 10.753 GeV, and measuring the partial widths.

The $\Upsilon(10753)$ state is located around the $\pi^\pm Z_b(10610)^\mp$ production threshold, therefore this particular decay channel allows not only to investigate the nature of the $\Upsilon(10753)$ state, but also to search for hints of the $Z_b(10610)$ production. In addition, $\Upsilon(10753)$ does not have enough energy to allow the decay into $\pi^\pm Z_b(10650)^\mp$.

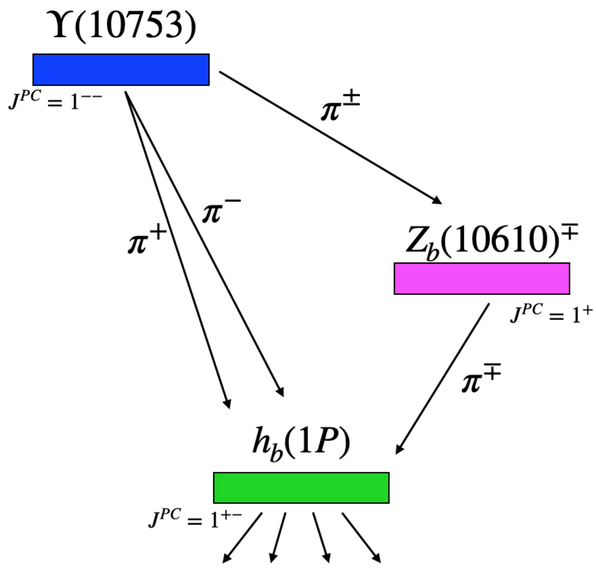

Figure 4.1: $\Upsilon(10753) \to \pi^+\pi^- h_b(1P)$ decay chains; both the pure phase space process and the transition through the intermediate charged state are shown.

4.1 Analysis outline

For this study, data taken during the 2021 Belle II energy scan around the $\Upsilon(10753)$ energy, with energies and corresponding luminosities indicated in Table 4.1, has been used. The pure phase-space transition is possible for all the energy values of the scan; instead, the process with the intermediate charged state is allowed only for the last energy point.

Table 4.1: Energy points of the scan and corresponding luminosities.

Energy [GeV]	**Luminosity(fb^{-1})**
10.653	3.5
10.701	1.6
10.745	9.8
10.805	4.7
Total	19.6

In this work, a blind analysis is presented without looking at the signal data of the decay channel of interest to avoid experimental bias that might influence the results of the analysis. Signal data will be eventually inspected in further studies, after the selection cuts and systematic uncertainties will be definitively determined and approved by the internal referee committee.

To reconstruct the decay chain, an exclusive strategy is not possible. In fact, the $h_b(1P)$ state mainly decays to the $\eta_b(1S)$ resonance through a radiative process. The latter then decays into lighter hadrons via multiple decay channels, each having a very small branching ratio that does not allow to reconstruct the single process with sufficient statistics. For this reason, an inclusive reconstruction is adopted. The recoil mass distribution of the pion pair will be inspected, searching for a signal around the $h_b(1P)$ mass value. For the decay channel that occurs through the intermediate charged state, also the recoil mass distribution of the single pion is studied, to look for a peak around the mass value of the $Z_b(10610)$ particle.

Since the $\Upsilon(10753)$ state is located around the $\pi Z_b(10610)$ threshold, the transition that occurs through an intermediate state has a narrower phase space, compared to the direct decay. In fact, the pion emitted with the $Z_b(10610)$ is expected to have a very low momentum, which generally affects the reconstruction performance. Since a large number of pions are produced in the decay chains, both from signal and background, it is important for the goals of this study to correctly reconstruct them.

The steps followed for the analysis are the following.

- Due to the importance of correctly reconstructing the pions produced in the decays, first of all the tracking reconstruction performance of the Belle II software is evaluated using Monte Carlo samples. In particular, special attention will be given to the low-momentum tracks.
- The first step of the physics analysis consists of finding the selection cuts in order to remove tracks that were wrongly reconstructed or generated by the beam background. Then, the efficiency of these cuts is evaluated. The track selection cuts are studied using MC samples.
- The efficiency of the cuts is then validated using experimental data belonging to the following control sample: $D^{*+} \to \pi^+ D^0 \to \pi^+ K^- \pi^+$. This particular channel has been chosen because it has similar properties to the processes studied in this analysis. In fact, the transition from the D^{*+} state to the D^0 has a very limited phase space, therefore the pion produced with the D^0 state is expected to have a very low momentum, just like the pions from the decay of the $\Upsilon(10753)$ resonance.

Chapter 5

Tracking Reconstruction Performance

To study the $\Upsilon(10753) \to \pi^+\pi^- h_b(1P)$ decay, it is very important to reconstruct the pions as accurately as possible. In particular, the transition that proceeds through the intermediate charged state $Z_b(10610)$ has a very limited phase space. In this process, pions with very low momenta are expected to be produced, which will strongly affect the reconstruction performance, since these tracks often do not reach the CDC and only the SVD information is available for tracking.

For this reason, in this chapter, a study is presented to evaluate the performance of the tracking reconstruction software.

In Section 5.1, both decay channels will be inspected with MC simulations, and, in Section 5.2, an additional study using the Particle Gun generator will be described. Then, in Section 5.3, the tracking efficiency will be evaluated and in Section 5.4 the performance of the new Flip and Refit algorithm will be studied.

All plots shown in the following sections have been made using the ROOT analysis framework.

5.1 Study with MC simulations

In this first section, a study of the $\Upsilon(10753) \to \pi^+\pi^- h_b(1P)$ decay is presented, considering both the direct process and the one that proceeds through the $Z_b(10610)^\pm$ states. The goal is to better understand these events and the response of the tracking detectors.

To perform this study, MC samples of both decay channels have been generated. The settings used for the simulations are summarized as follows.

- Software release: release08
- Number of events: 10.000
- Beam energy: 10.751 GeV
- Beam background: NO
- Flip&Refit: ON

In this chapter, the latest software release available at the time this work was started has been used, which is *release08*. This choice has been made to evaluate the tracking performance using the latest version of the software and also to study the effects of the new *Flip and Refit* algorithm, which has been implemented for the first time in this release.

The number of simulated events was chosen to be 10.000, as a compromise between sufficient statistics for the analysis and the necessary time required to generate the MC sample.

The simulated experiment recreates detector conditions similar to those recorded during the real data acquisition. In particular, for the PXD, the geometry discussed in section 2.2.1 has been considered, in which only the first layer of the detector is completed, while only two ladders are mounted on the second one, as shown in Fig. 2.6.

The beam energy has been fixed to the closest available value to the $\Upsilon(10753)$ resonance, which is 10.751 GeV. The beam background generation has been turned off for this study, while the Flip and Refit algorithm is being used at the end of the tracking chain.

The event generation has been performed using *EvtGen* [34]. The initial state particle is a virtual photon *vpho*, which then decays into $\pi\pi h_b(1P)$ through the two processes represented in Fig. 4.1. The $h_b(1P)$ state decays to $\gamma\eta_b(1S)$ or a gluon pair, using the event generator *PYTHIA* [41]. The $\eta_b(1S)$ resonance then decays into two gluons, also using *PYTHIA*.

The decay tables used for all these transitions can be found in Appendix A.

The output of the simulations for both processes will now be discussed, starting with single-pion distributions of several kinematic variables.

The transverse momentum distributions of single pions reconstructed in both decay channels are shown in Fig. 5.1.

Each plot shows the comparison between the distributions of pions from the decay of the $\Upsilon(10753)$ state with those from the $h_b(1P)$ decays (and from its decay products) (Fig. 5.1a) or $Z_b(10610)$ (Fig. 5.1b).

From now on, for both decay channels, pions directly produced from the $\Upsilon(10753)$ decay will be named *signal pions*.

The pions produced in these events mostly have momenta lower than 1 GeV/c. In particular, the distribution of signal pions in the pure phase space decay peaks around 300 MeV/c. Instead, for the decay channel that proceeds through the Z_b state, the peak value of the signal pions distribution is around 80 MeV/c. Indeed, since this transition has a very narrow phase space compared to the direct one, very low momentum pions were expected to be observed in this channel. Furthermore, pions from the Z_b decays are produced together with the $h_b(1P)$ state, thus, due to the limited available energy, their transverse momentum distribution is truncated at around 700 MeV/c.

In the distributions of the cosine of polar angle, all reconstructed pions show a boost in the forward direction, due to the asymmetry of the collisions. This is particularly prominent for the channel in which the transition proceeds through

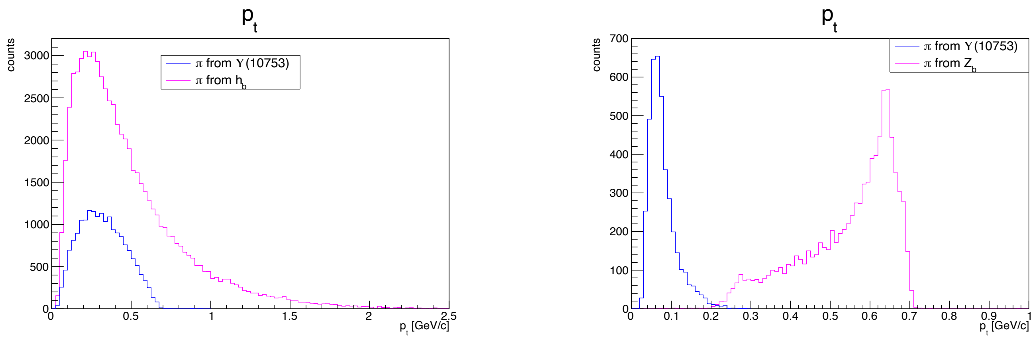

(a) (b)

Figure 5.1: Transverse momentum distributions of single pions reconstructed from (a) $\Upsilon(10753) \to \pi^+\pi^- h_b(1P)$ and (b) $\Upsilon(10753) \to \pi Z_b(10610) \to \pi\pi h_b(1P)$ decays. Blue lines are for pions coming from the $\Upsilon(10753)$ decay; magenta lines identify pions from the $h_b(1P)$ (a) and Z_b (b) decays.

the intermediate state and is related to the kinematics of the decay. Due to the mass difference between the $\Upsilon(10753)$ and $Z_b(10610)$, signal pions get most of the boost energy from the collision. For the pure phase space decays, instead, the energy boost is distributed between the two charged pions, making this effect less evident.

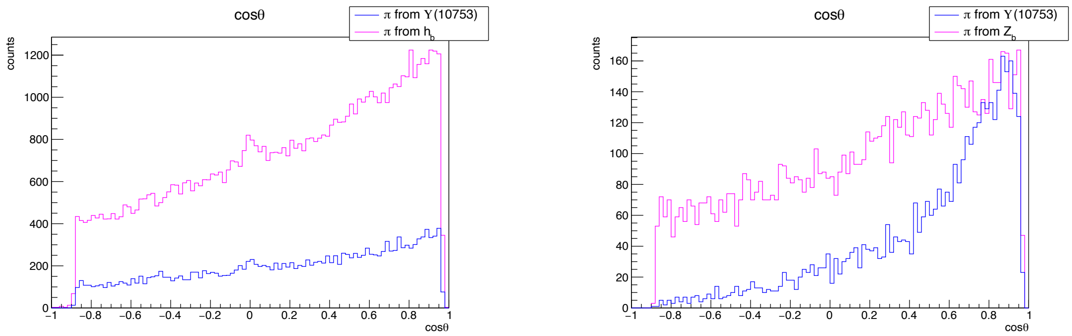

(a) (b)

Figure 5.2: $\cos\theta$ distributions of single pions reconstructed from $\Upsilon(10753) \to \pi^+\pi^- h_b(1P)$ (a) and $\Upsilon(10753) \to \pi Z_b(10610) \to \pi\pi h_b(1P)$ (b) decays. Blue lines are for pions coming from the $\Upsilon(10753)$ decay; magenta lines identify pions from the h_b (a) and Z_b (b) decays respectively.

In Fig. 5.2a a small peak around $\cos\theta = 0$ can also be noticed. This is due to low-momentum particles whose tracks are perpendicular to the solenoid axis. They keep curling in the detector leaving multiple hits in the same space region; therefore, the same track might be reconstructed multiple times by the software.

The azimuthal angle distribution, instead, is overall uniform for all pions, as shown in Fig. 5.3.

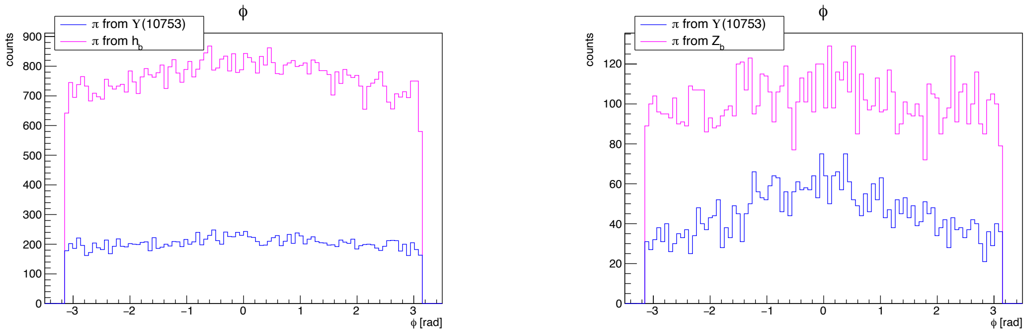

(a) (b)

Figure 5.3: Distributions of the ϕ angle for single pions reconstructed from (a) $\Upsilon(10753) \rightarrow \pi^+\pi^- h_b(1P)$ and (b) $\Upsilon(10753) \rightarrow \pi Z_b(10610) \rightarrow \pi\pi h_b(1P)$ decays. Blue lines are for pions coming from the $\Upsilon(10753)$ decay; magenta lines identify pions from the h_b (a) and Z_b (b) decays respectively.

The distributions of the number of hits associated to tracks for each tracking detector have also been studied, to evaluate the quality of reconstructed tracks.

From now on, in the following plots, only the distributions of reconstructed *signal pions* will be shown.

Starting from the innermost detector, the PXD, the number of hits distribution is shown in Fig. 5.4.

For the pure phase space decay, the distribution peaks at 1, with also some tracks recorded with 2 hits. This is in agreement with the simulated configuration of the detector, in which one layer is complete, while in the other one only two ladders are active.

Instead, for the decay channel that proceeds through the $Z_b(10610)$ state, something unexpected was observed. The distribution of the number of PXD hits shows a peak at 0, which means that no pixel detector hits have been attached to the track. This effect is observed for tracks with a very prominent boost in the forward direction and with very low transverse momenta, between 40-80 MeV/c, as shown in Fig. 5.4f and Fig. 5.4d. It might suggest a missing correlation with PXD, and thus will be investigated more in detail.

The other VXD component, the SVD, employs a double-sided strip technology; therefore, a particle crossing this detector should ideally leave a signal on both sides of each strip. Since there are 4 strips in total, the highest number of SVD hits to be detected should be 8. However, ladders belonging to the same layer overlap in certain regions of ϕ, thus the number of hits can reach up to 16.

The distributions of the number of hits on the SVD peak at 8 for both decay channels, as shown in Fig.5.5, which means that generally particles cross all 4 layers of the detector. For the transition that proceeds through $Z_b(10610)$, a large number of tracks composed of 6 hits can also be observed. This is due to very low momentum particles, which only reach the first three layers of the detector.

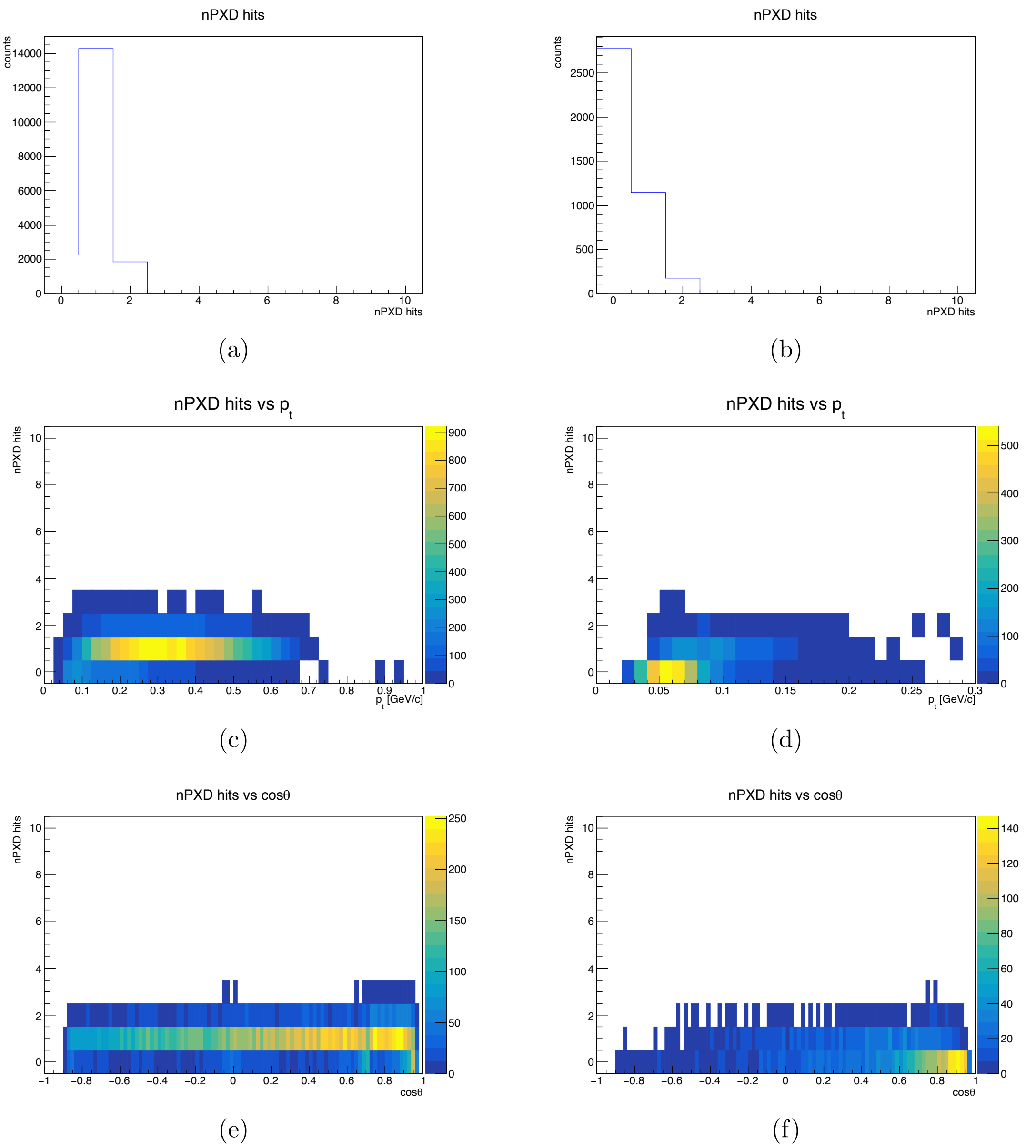

Figure 5.4: Number of PXD hits distributions of single pions reconstructed from $\Upsilon(10753) \to \pi^+\pi^- h_b(1P)$ (left) and $\Upsilon(10753) \to \pi Z_b(10610) \to \pi\pi h_b(1P)$ (right) decays. Only signal pions are shown. In the second and third row these distributions are shown as a function of p_t and cosθ, respectively.

Overall, for both decay channels, the tracks are well defined, even for low p_t particles, since three space points provide enough degrees of freedom to unambiguously define the helix trajectory in a magnetic field [27]. However, as previously noted, for very low momenta, tracks do not have PXD hits attached to them.

The missing information by the pixel detector for the track reconstruction of low momenta particles does not affect the track finding; in fact, as discussed in Section 3.3.2, PXD hits are attached to tracks already found using the CDC and SVD information, employing the CKF. However, the reconstruction of low

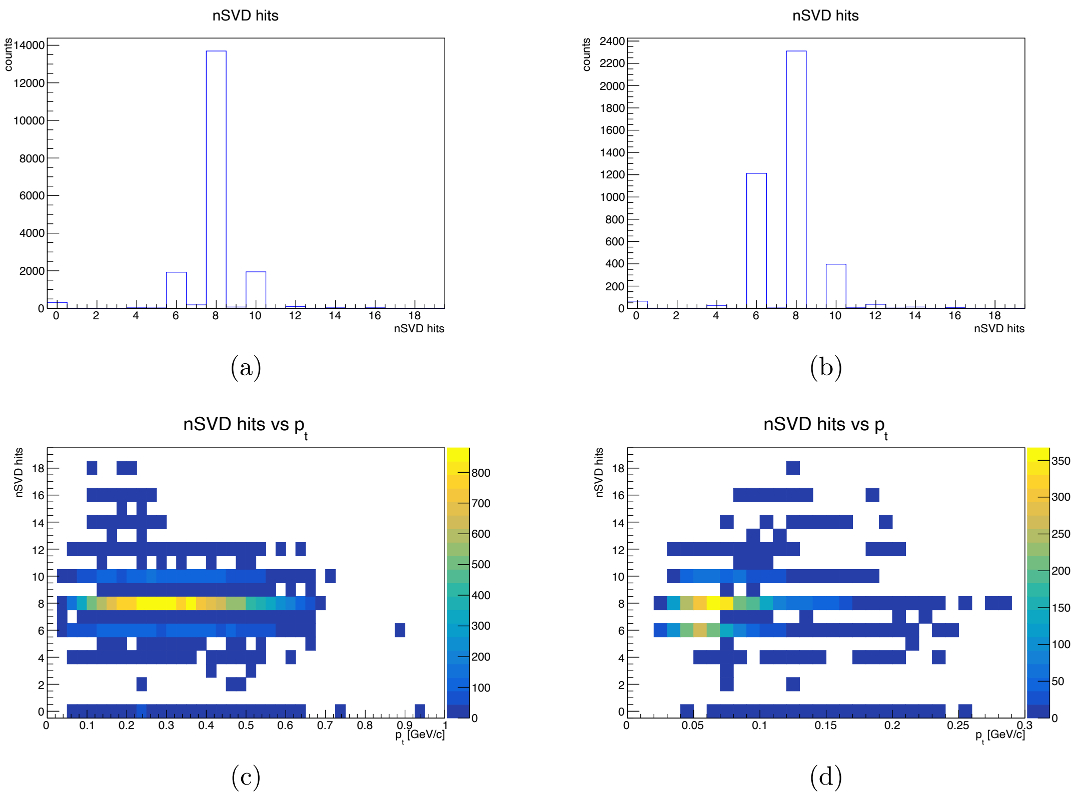

Figure 5.5: Number of SVD hits distributions of single pions reconstructed from $\Upsilon(10753) \to \pi^+\pi^- h_b(1P)$ (left) and $\Upsilon(10753) \to \pi Z_b(10610) \to \pi\pi h_b(1P)$ (right) decays. Only signal pions are shown. In the second row the same distributions are shown as a function of p_t.

momenta tracks is generally challenging, since for most of those only the measurements of the four layers of the SVD are available. Furthermore, if particles in this momentum region reach the CDC, they can loop several times in the detector volume, producing multiple hits, making reconstruction very challenging.

For this reason, the missing PXD information degrades the momentum resolution and, since the pixel detector is the closest to the IP, it also affects the quality of the vertex reconstruction.

To further investigate this unexpected effect, a study using the *Particle Gun* generator has been conducted and will be discussed in the next section.

To conclude the detector hits study, the number of CDC hits per track for low momenta particles is very low, since they often do not have the necessary energy to reach the outer tracking detector; this is particularly obvious for pions produced with the $Z_b(10610)$, as seen in Fig. 5.6b.

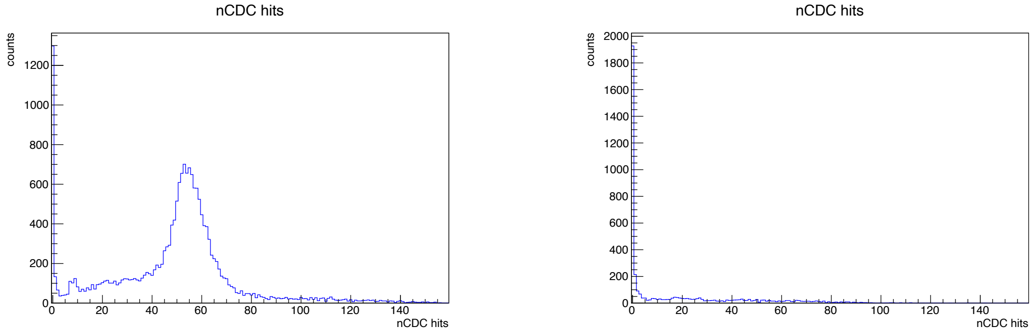

(a) (b)

Figure 5.6: Number of CDC hits distributions of single pions reconstructed from $\Upsilon(10753) \rightarrow \pi^+\pi^- h_b(1P)$ (left) and $\Upsilon(10753) \rightarrow \pi Z_b(10610) \rightarrow \pi\pi h_b(1P)$ (right) decays. Only signal pions are shown.

5.2 Particle Gun Scan

To understand the causes behind the missing association of PXD hits to low momenta tracks, this phenomenon has been investigated in more detail.

First of all, it was studied, with the sample generated in Section 5.1 and using *MC truth* variables, if this effect could be related to the wrong charge assignment to reconstructed tracks. It was also checked if, in these events, the MC particle was actually seen in the pixel detector. Both hypotheses were discarded to be the cause of the missing PXD hits association, as can be seen in Appendix B.

To further investigate this effect, a new MC sample has been produced using the *Particle Gun* module, which allows to generate simple events where all tracks have determined momentum, angular and vertex distributions.
The parameters chosen for the simulations are summarized as follows.

- Software release: release08
- 100.000 events
- Single track per event
- Random generation of $\pi^{\pm}$
- Beam background: NO
- Uniform p_t between [0.02, 0.1] GeV/c
- Uniform cosθ, with θ between [17°, 150°]
- Uniform *phi* between [0°, 360°]

For these simulations, the same version of the software as before has been used, *release08*.

To increase the available statistics, 100.000 events were simulated and in each event, a single track which randomly represented a positive or negative pion was generated.

The particles were produced with a uniform transverse momentum distribution from 0.02 to 0.1 GeV/c, in order to study the reconstruction performance in the very low momentum region. Furthermore, pions were simulated with distributions of the cosine of polar angle and the azimuthal angle uniform in the whole geometrical acceptance region of the detectors.

The events for this study were generated without beam background.

The average number of PXD and SVD hits per reconstructed track has been evaluated, as shown in Fig. 5.7.

In the very low p_t region, between 60 and 100 MeV/c, the average number of SVD hits attached to each track is predominantly around 8. This means that pions cross all four layers of the strip detector and therefore track candidates should be well defined even for very low momentum particles.

However, in the same momentum region, the average number of PXD hits attached to each track is always less than 1, which implies that no hit has been associated to the track candidates.

Therefore, for very low p_t particles, tracks are correctly found but they don't have any PXD hits attached to them, which degrades the overall reconstruction performance for these tracks, especially the quality of track parameters.

This effect might be related to issues regarding the extrapolation of tracks toward the PXD, for example, track parameter residuals being outside the acceptance region defined by the CKF. Another hypothesis is that the CKF algorithm has not been trained enough for this specific class of very slow pions.

Improving the track extrapolation algorithm toward PXD or re-training the CKF for very low p_t tracks might help solve this issue in the future.

5.3 Tracking Efficiency

In this section, the overall tracking efficiency for signal pions has been studied for both $\Upsilon(10753)$ decay channels, using the same MC sample generated in Section 5.1.

In all the plots that will be presented, the following cuts have been applied to the samples, *"seenInSVD or seenInCDC"*, which indicate whether the MC particle was measured by SVD or CDC. These cuts use the *MC truth* information and allow to factor out the geometrical acceptance of the detector to easily study the performance of tracking algorithms. The effects of taking or not into account the geometrical acceptance can be seen in Appendix C.

To evaluate tracking efficiency, several figures of merit have been studied. These have been estimated using MC truth-related information.

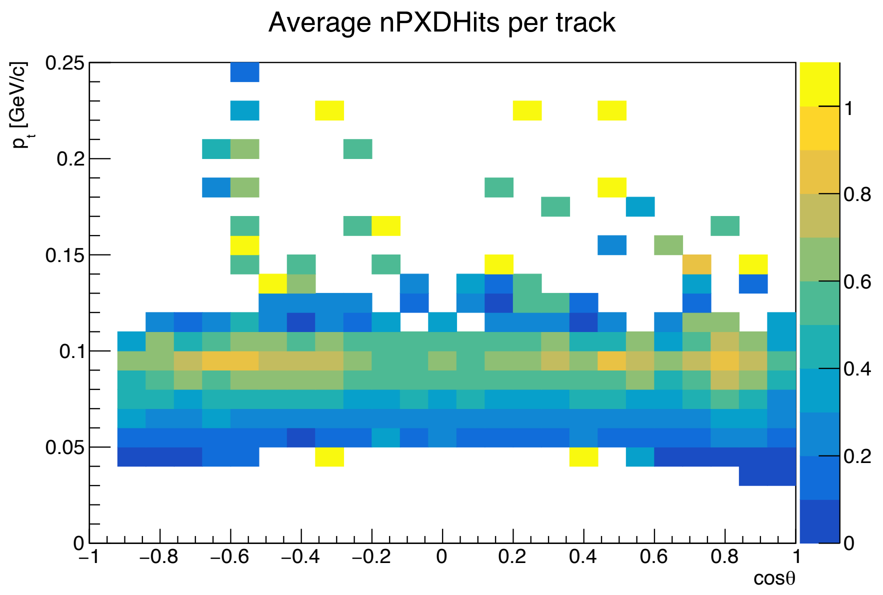

(a)

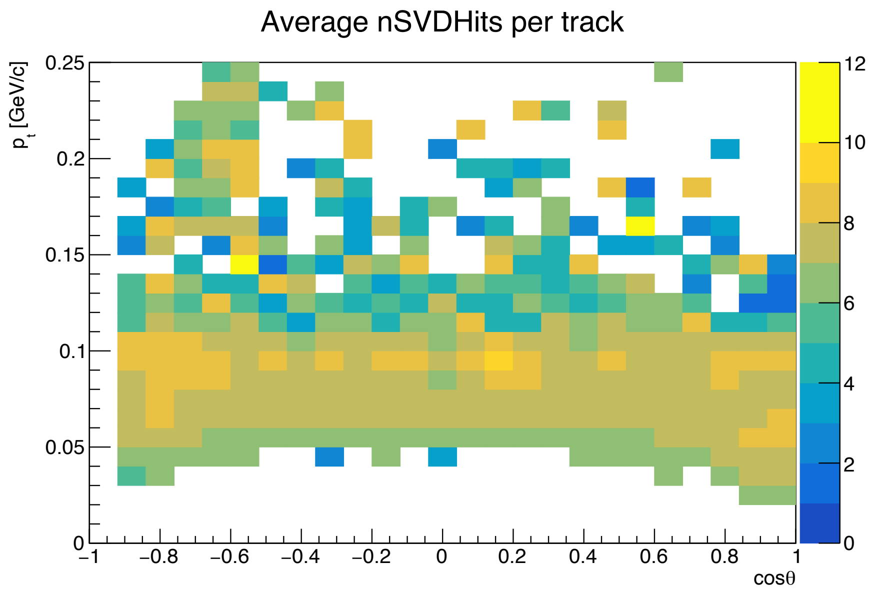

(b)

Figure 5.7: Average number of PXD (a) and SVD (b) hits per track as a function of p_t and $cos\theta$ evaluated using a Particle Gun scan.

Finding Charge Efficiency

The track *Finding Charge Efficiency* is defined as:

$$\text{Finding Charge Efficiency} = \frac{\text{matched MC with correct charge}}{\text{all primary MC}}$$

It is measured as the number of matched MC tracks reconstructed with the correct charge divided by the number of all the primary MC tracks, and evaluates the probability that the track is correctly reconstructed and that the correct charge is assigned to it.

In general, the Finding Efficiency does not depend on the pixel detector measurements, since in the tracking algorithm the PXD hits are attached to candidate tracks previously found only using the SVD and CDC information. The Finding Charge Efficiency, in particular, also requires for the correct charge to be assigned to the track.

The results, evaluated as a function of the MC value of transverse momentum for both the pure phase space decay channel and the one that proceeds through the $Z_b(10610)$ state, are shown in Fig. 5.8.

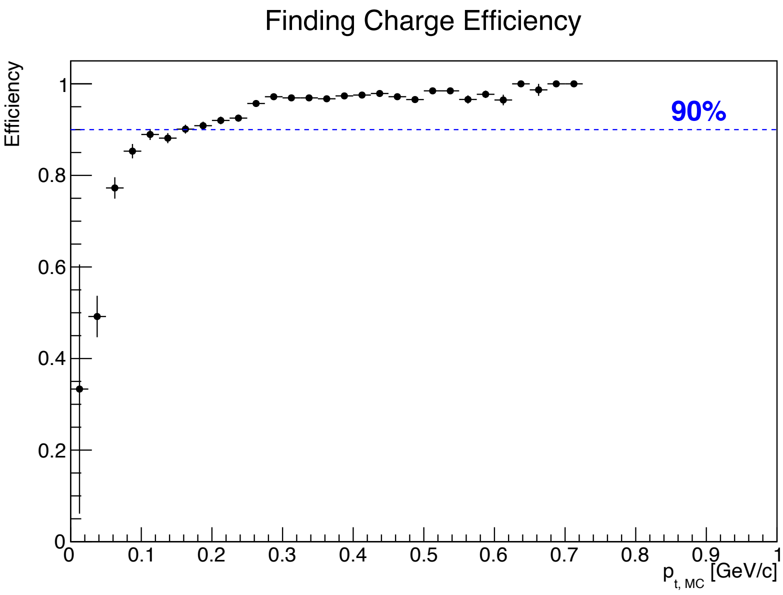

(a)

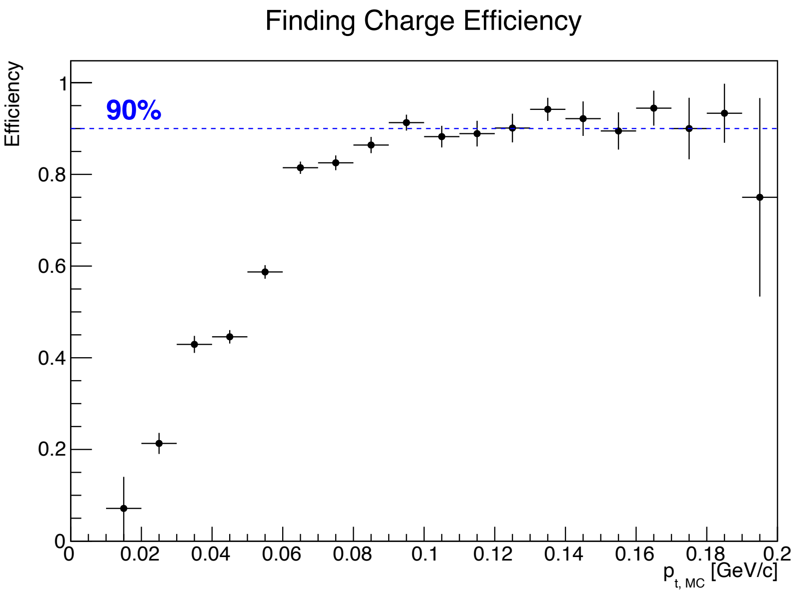

(b)

Figure 5.8: Finding Charge Efficiency of signal pions as a function of $p_{t,MC}$ for both $\Upsilon(10753) \to \pi^+\pi^- h_b(1P)$ (a) and $\Upsilon(10753) \to \pi Z_b(10610) \to \pi\pi h_b(1P)$ (b) decays. Binomial errors have been computed.

For each efficiency value, binomial errors have been computed.

In general, the decay channel that proceeds through the intermediate charged state shows larger error bars due to the lower number of signal pions in the sample.

For both channels, the finding charge efficiency decreases in the low momentum region, and in particular the efficiency value drops below 90% for p_t between 80 and 100 MeV/c. Furthermore, in the low transverse momentum region, the two distributions show compatible trends, in agreement with what is expected after factoring out the geometrical acceptance of the detector.

The small dips observed in the distributions are related to the geometry of the detector and, in particular, to which tracking detector information is being used to reconstruct the tracks.

Charge Efficiency

The track *Charge Efficiency* is defined as:

$$\text{Charge Efficiency} = \frac{\text{matched MC with correct charge}}{\text{matched MC}}$$

It is measured as the number of matched MC tracks reconstructed with the correct charge divided by the number of all matched MC tracks. This figure of merit evaluates the probability that the correct charge is assigned to the reconstructed track. The results, obtained for both decay channels, are shown in Fig. 5.9.

The large error bars for some efficiency values in Fig. 5.9b are due to being computed in bins with low statistics, as can be seen in Appendix D.

For both decay channels, the charge efficiency decreases in the p_t region between 80 to 300 MeV/c, which signifies that, for low transverse momenta tracks are correctly reconstructed, but the wrong charge has been assigned.

5.4 Flip and Refit Performance

The *Flip and Refit* algorithm, already discussed in detail 3.3.2, can be employed to correct the charge of tracks which have been correctly found, but have been assigned the wrong charge.

To evaluate the effect of this new step of the tracking chain, new MC samples, where the Flip and Refit algorithm has been turned *OFF*, have been generated for both decay channels, using the same settings presented in Section 5.1.

Then, using these newly simulated events, the Charge Efficiency has been evaluated, as defined in the previous section.

In the plots of Fig. 5.10, a comparison between the Charge Efficiency evaluated as a function of the MC value of transverse momentum and obtained using MC sample *with* and *without* the Flip and Refit algorithm, is shown.

Simulations in which the Flip and Refit algorithm has been employed show an overall improvement in the p_t region between 80 to 300 MeV where the charge efficiency has generally lower values for both decay channels. In particular, for the pure phase space transition the efficiency increases of about 3%. For the process

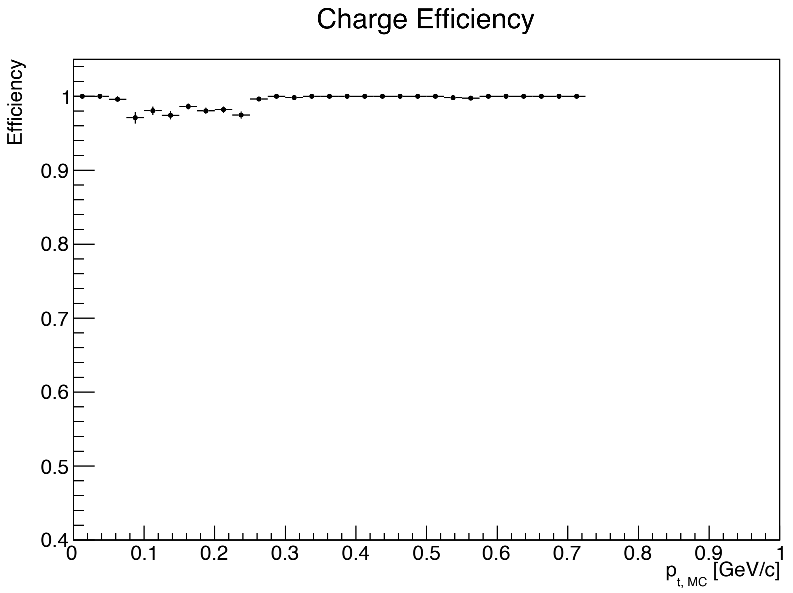

(a)

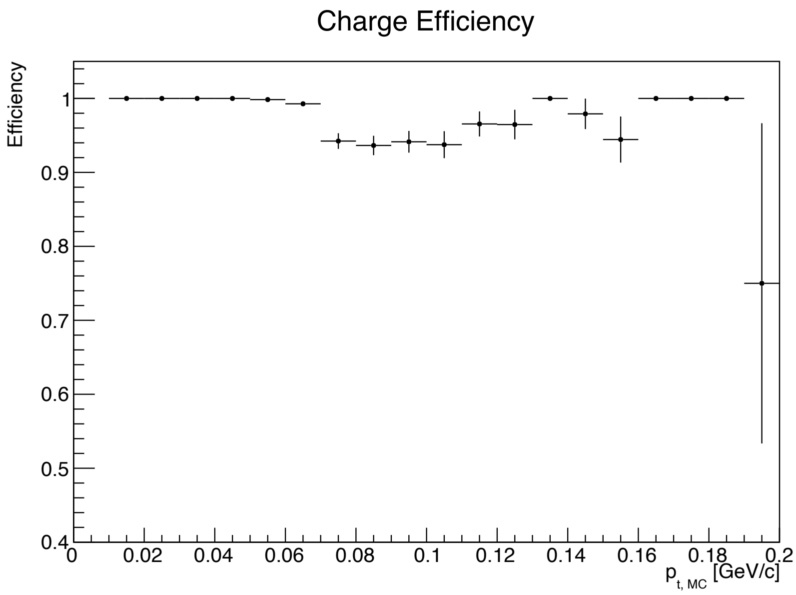

(b)

Figure 5.9: Charge efficiency of signal pions as a function of $p_{t,MC}$ for both $\Upsilon(10753) \to \pi^+\pi^- h_b(1P)$ (a) and $\Upsilon(10753) \to \pi Z_b(10610) \to \pi\pi h_b(1P)$ (b) decays. Binomial errors have been computed.

mediated by the $Z_b(10610)$ state, instead, the effect of Flip and Refit improves the charge efficiency from the lowest value of 85% measured without the use of the algorithm to around 95%.

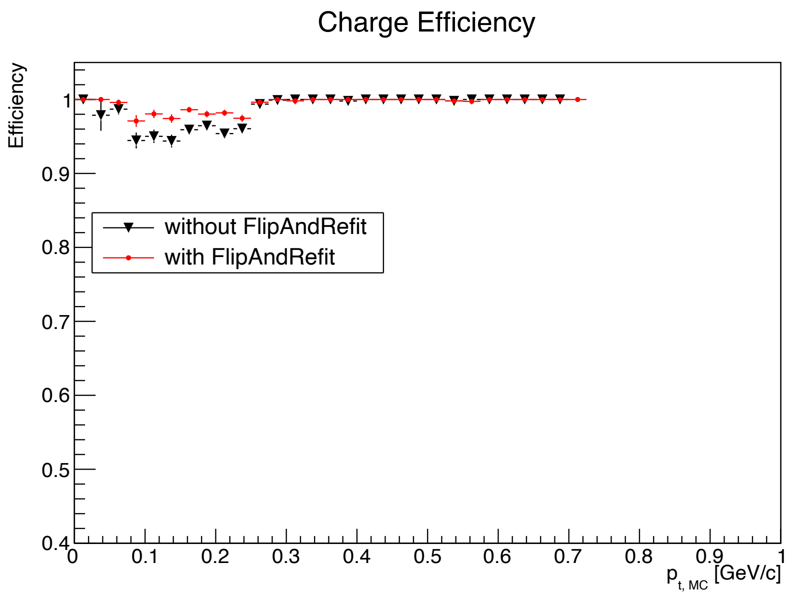

(a)

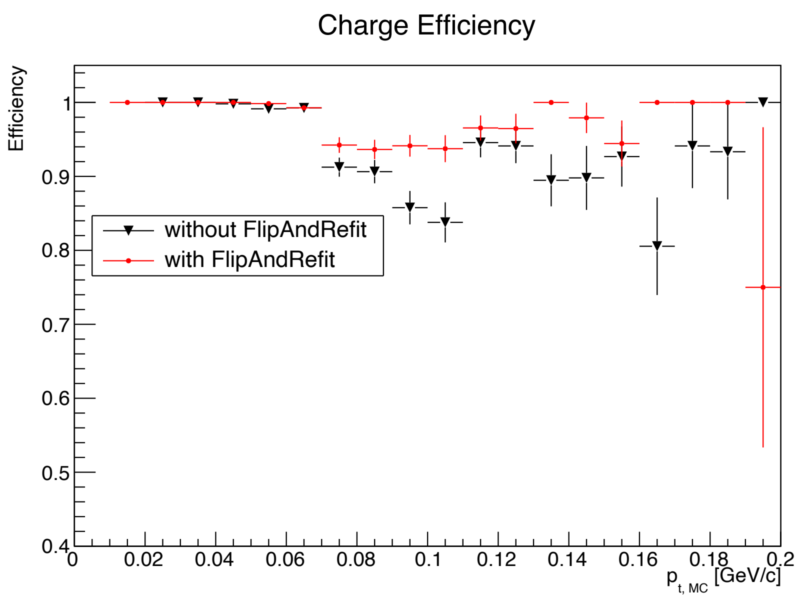

(b)

Figure 5.10: Charge efficiency of signal pions as a function of $p_{t,MC}$ for both $\Upsilon(10753) \rightarrow \pi^+\pi^- h_b(1P)$ (a) and $\Upsilon(10753) \rightarrow \pi Z_b(10610) \rightarrow \pi\pi h_b(1P)$ (b) decays. Binomial errors have been computed. Comparison between the efficiency evaluated with (red) and without (black) the Flip and Refit algorithm.

Flipped Fraction and Flipping Efficiency

To further study the performance of Flip and Refit, other figures of merit can be evaluated. These are the *Flipped Fraction* and the *Flipping Efficiency*, defined as follows:

$$\text{Flipped Fraction} = \frac{\text{FlippedAndRefitted tracks}}{\text{all reconstructed tracks}}$$

$$\text{Flipping Efficiency} = \frac{\text{(matched MC with correct charge) and (track is FlippedAndRefitted)}}{\text{(matched MC and track is FlippedAndRefitted) or (matched MC with wrong charge)}}$$

The first computes the fraction of reconstructed tracks to which the Flip and Refit algorithm has been applied. The Flipping Efficiency, instead, evaluates how many tracks were flipped correctly (with the correct charge) above all the tracks which were flipped or which had to be flipped due to the wrong charge. In more simple terms, it is an evaluation of the correctness of the flipping. The results are shown in Fig. 5.11.

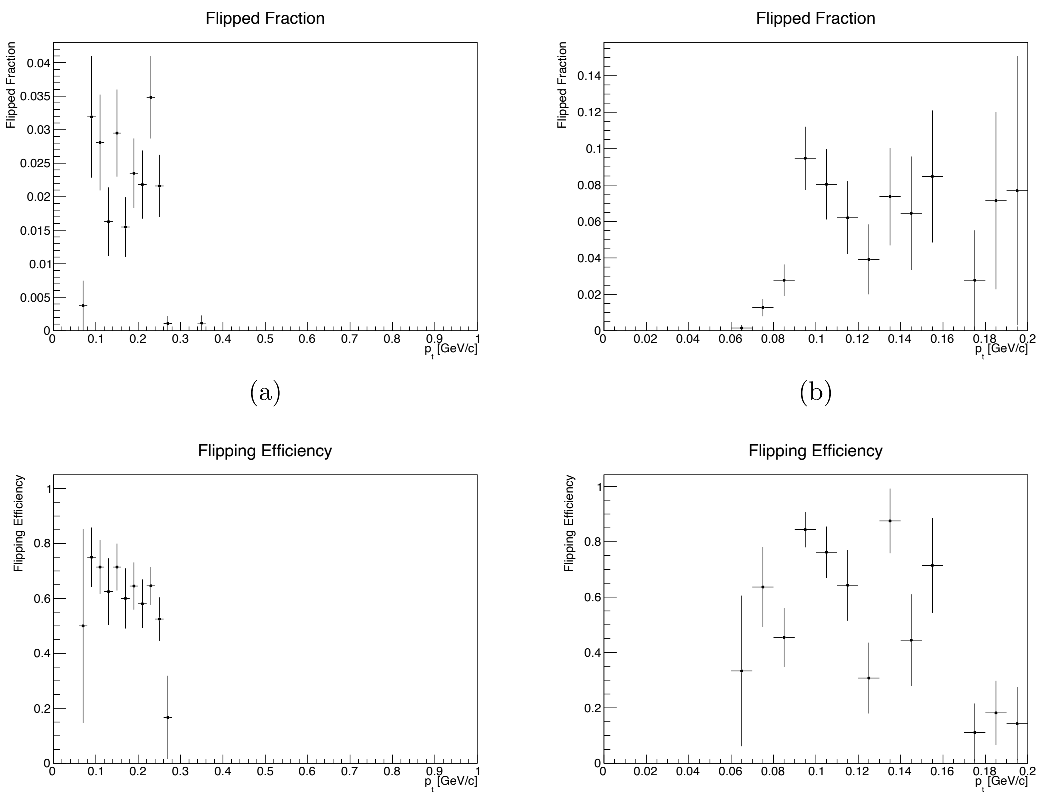

Figure 5.11: Flipped fraction (top) and Flipping Efficiency (bottom) of signal pions as a function of p_t, evaluated for both $\Upsilon(10753) \to \pi^+\pi^- h_b(1P)$ (left) and $\Upsilon(10753) \to \pi Z_b(10610) \to \pi\pi h_b(1P)$ (right) decays. Binomial errors have been computed.

For signal pions reconstructed in the pure phase space decay channel, the flipped fraction is small, around $1.5 - 3.5\%$. For the Z_b decay channel, instead, more tracks are flipped and refitted, up to the 15%, since the reconstruction performance is degraded for very low momentum pions.

The Flipping Efficiency is quite good for the first decay channel, from 50% to almost 80%; for the other channel, the efficiency fluctuates with transverse momenta from 20% to 90%.

Overall, these plots shows that mostly low momentum tracks are flipped, with p_t up to 300 MeV/c for the first decay channel. It is also important to note that the algorithm is not effective below 80 MeV/c; however, in this momentum region the charge efficiency is already very good and therefore the refining step of Flip and Refit is not necessary.

In conclusion, the Flip and Refit algorithms allows to increase the reconstruction efficiency for low momentum tracks, and this can play an important role in the analysis of the channels of interest of this work, in particular for the decay channel involving the $Z_b(10610)$ state production.

Chapter 6

Track Selection Cuts

In this chapter, the first part of the physics analysis will be discussed.

In Section 6.1, the signal for the $e^+e^- \to \pi^+\pi^- h_b(1P)$ and $e^+e^- \to \pi^\pm Z_b(10610)^\mp \to \pi^\pm\pi^\mp h_b(1P)$ transitions will be studied, using MC samples from the official Belle II production. In Section 6.2, the cuts for the signal track selection will be identified and in Section 6.3 their efficiency will be evaluated.

All plots shown in the following sections have been made using the Matplotlib Python library.

6.1 Studies on signal MC samples

For the next part of the analysis, MC samples generated during the latest available official data production campaign of the Belle II experiment have been used. The *run-dependent* MC simulations (i.e. reproducing experimental conditions during each run of data taking, including detector and accelerator configurations, but also beam background conditions) have been produced using the previous version of the software, the *release06*, in which, for example, the Flip and Refit algorithm discussed in the previous chapter is not implemented. This is due to the not readiness of the official run-dependent MC production with the *release08* at the time of the end of this work.

The sample in which the event is generated as a pure phase space transition, $e^+e^- \to \pi^+\pi^- h_b(1P)$, will be called from now on the *signal MC sample.* This process is kinematically allowed for all four energies of the scan, which are 10.653 GeV, 10.701 GeV, 10.745 GeV and 10.805 GeV. The pions directly produced from the $\Upsilon(10753)$ decay will be referred to as *signal pions.*

Instead, the MC sample in which the transition proceeds through an intermediate Z_b state will be named the Z_b *signal MC sample.* For the $e^+e^- \to \pi^\pm Z_b(10610)^\mp \to \pi^\pm\pi^\mp h_b(1P)$ decay, both processes follow a phase space transition. The only center-of-mass energy value of the scan for which this decay is kinematically allowed is 10.805 GeV. At this energy point, the transition could proceed through both the $Z_b(10610)$ and $Z_b(10650)$ states, with Q values of 55 MeV and 15 MeV, respectively. For the purposes of this analysis, the $e^+e^- \to \pi Z_b(10650)$ channel will not be investigated due to its extremely small Q value, which makes the signal pion substantially undetectable. The pions produced together with the $Z_b(10610)$ state in the $e^+e^- \to \pi Z_b(10650)$ decay will now be referred to as *soft* *pions*, while the pions from the decay $Z_b(10610)^{\pm} \to \pi^{\pm} h_b(1P)$ will be named *hard pions*. The motivation behind these names will be discussed shortly after.

The transverse momentum distributions of the reconstructed signal pions from the *signal MC sample* are shown, for the four different energy points, in Fig. 6.1.

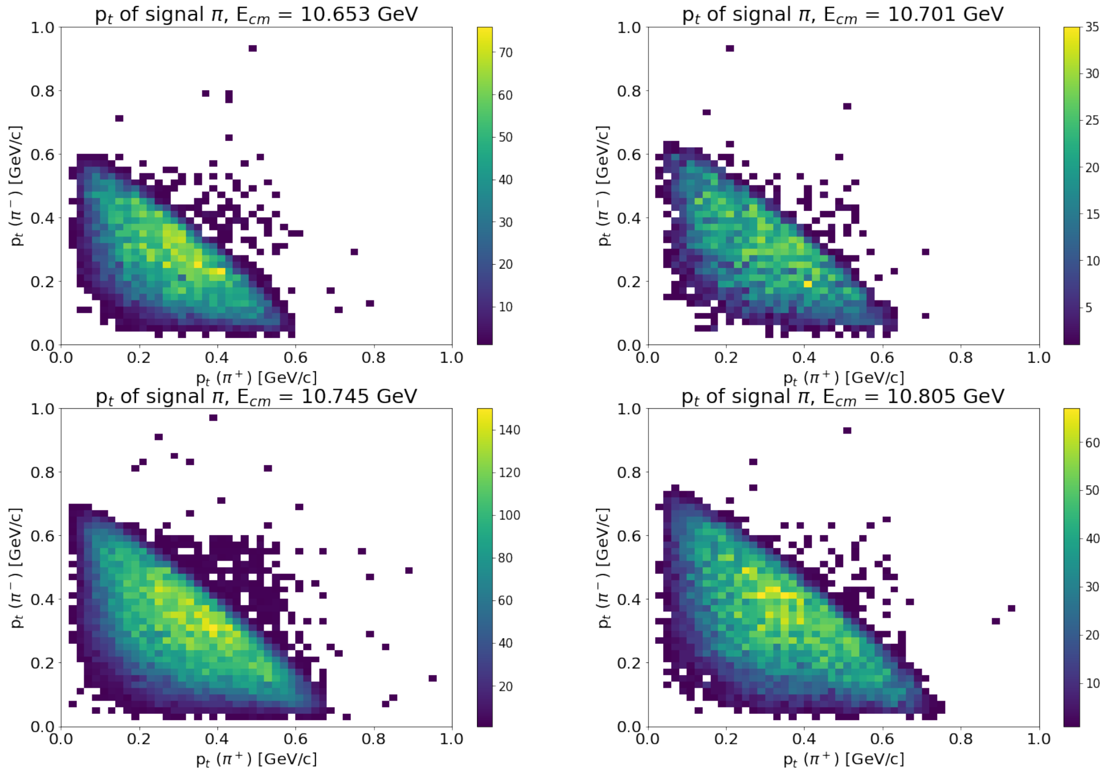

Figure 6.1: Two-dimensional transverse momentum distribution of the signal pion pair from the $e^+e^- \to \pi^+\pi^- h_b(1P)$ decay, at the four energy points of the scan.

At all four energy points, the positive and negative signal pion distributions are symmetric, in agreement with the kinematics of the decay. Reconstructed tracks of signal pions have low momenta, which slightly increase with the center of mass energy.

For the Z_b *signal MC sample*, the distribution of the reconstructed transverse momenta of slow and hard pions is shown in Fig. 6.2.

The plot shows an asymmetry between the two distributions; in particular, pions generated with the $Z_b(10610)$ state have very low momenta, with the peak value of the distribution around 130 MeV/c. This is in agreement with the kinematics of the decay, since the $e^+e^- \to \pi Z_b(10610)$ transition has a very limited phase space compared to the $Z_b(10610) \to \pi h_b(1P)$ decay. This explains the choice of naming the pions produced with and from the Z_b respectively *soft* and *hard*.

For both the $e^+e^- \to \pi^+\pi^- h_b(1P)$ and $e^+e^- \to \pi^{\pm} Z_b(10610)^{\mp} \to \pi^{\pm}\pi^{\mp} h_b(1P)$ processes, the distributions of the other kinematic variables related to the reconstructed pions have been inspected, such as cosθ, ϕ and the number of PXD, SVD

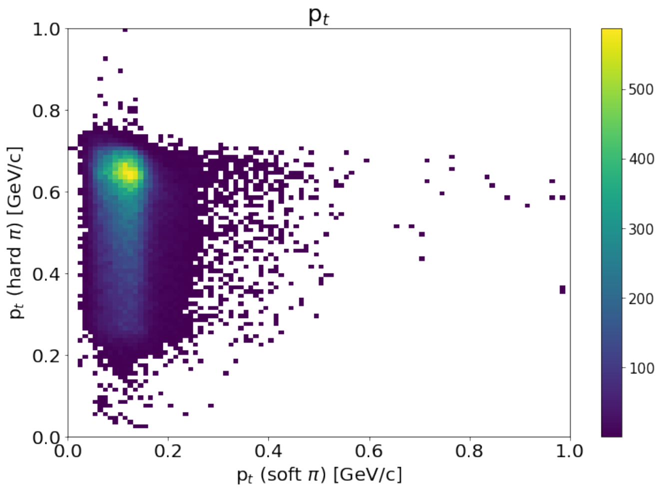

Figure 6.2: Two-dimensional transverse momentum distribution of soft and hard pions from the $e^+e^- \to \pi Z_b(10610) \to \pi\pi h_b(1P)$ decay, at the 10.805 GeV energy point of the scan.

and CDC hits. For the first decay channel, the reconstructed values from the four energy points have been combined. These plots can be found in Appendix E.

For the $e^+e^- \to \pi^+\pi^- h_b(1P)$ process, the invariant mass of the system recoiling against the reconstructed pion pair $M_{recoil}(\pi\pi)$ has been evaluated. This variable is defined as follows:

$$M_{recoil}(\pi\pi) = \sqrt{(E_{c.m.} - E^*_{\pi\pi})^2 - p^{*2}_{\pi\pi}}$$

where $E_{c.m.}$ is the center-of-mass energy and $E^*_{\pi\pi}$ and $p^*_{\pi\pi}$ are, respectively, the energy and momentum of the pion pair measured in the center-of-mass frame. The distributions obtained from the four energy points of the scan are shown in Fig. 6.3.

For the *signal MC sample*, the number of events generated for each energy point is proportional to the luminosity recorded during the real data scan, indicated in Table. 4.1.

The $M_{recoil}(\pi\pi)$ distribution is evaluated considering both signal and non-signal pions, since in real data the two contributions cannot be separated.

For all energy points, the distribution is composed of a background uniform component and a signal component, identified by a peak around the $h_b(1P)$ mass value 9.899 GeV$/c^2$.

The recoil mass distribution has also been studied for the $e^+e^- \to \pi^\pm Z_b(10610)^\mp \to \pi^\pm\pi^\mp h_b(1P)$ process, as shown in Fig. 6.4. For this decay channel, only the MC samples at the 10.805 GeV energy are used.

Even in this case, the $M_{recoil}(\pi\pi)$ distribution has been evaluated using both the reconstructed signal and non-signal pions, like in real data samples.

The distribution consists of an asymmetric background component around the signal component, which peaks at the mass value of $h_b(1P)$.

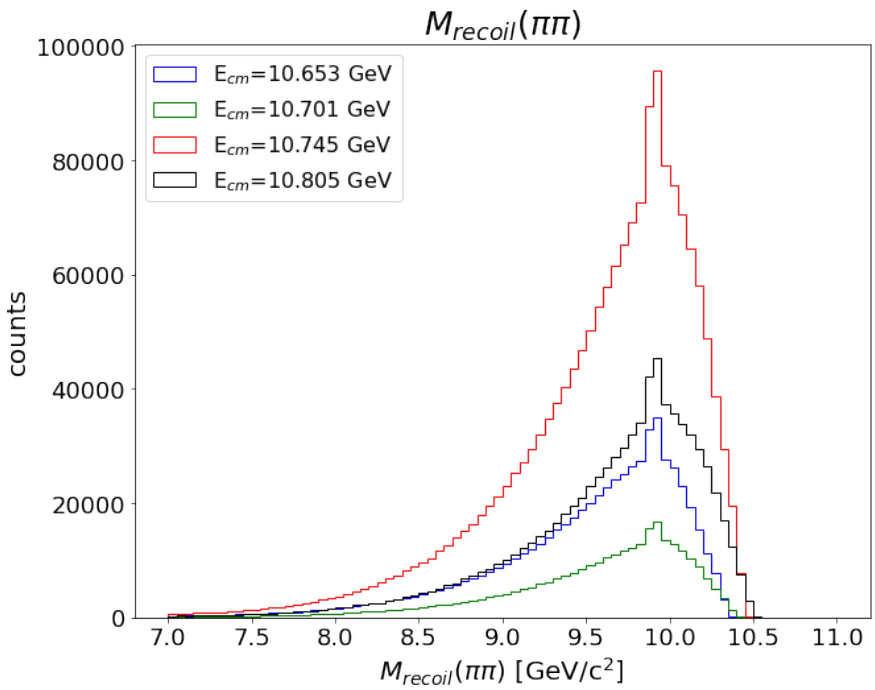

Figure 6.3: $M_{recoil}(\pi\pi)$ distribution from the $e^+e^- \to \pi^+\pi^-h_b(1P)$ decay, at the four energy points of the scan.

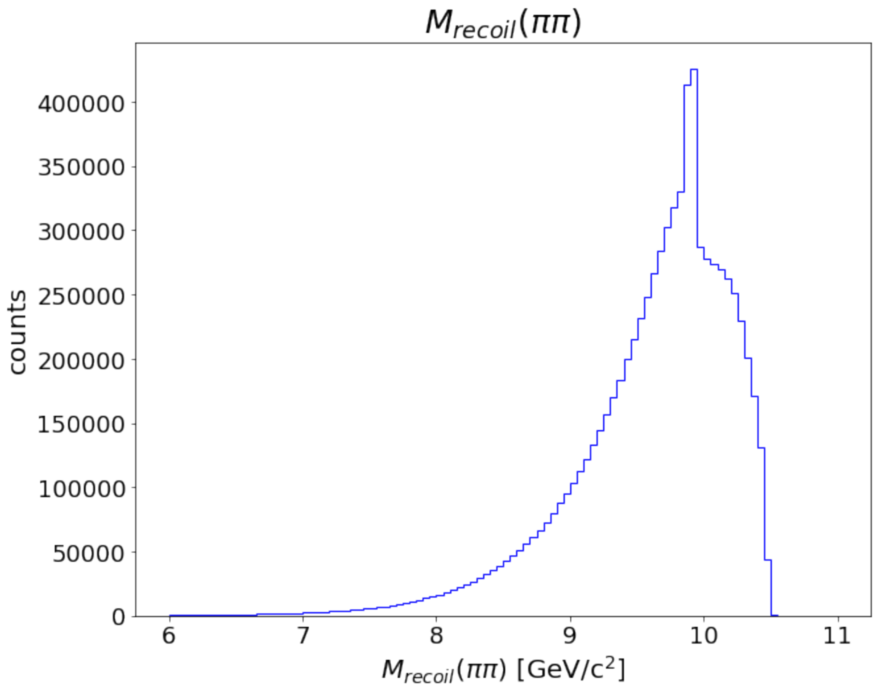

Figure 6.4: $M_{recoil}(\pi\pi)$ distribution for the $e^+e^- \to \pi Z_b(10610) \to \pi\pi h_b(1P)$ decay, at the 10.805 GeV energy point of the scan.

For this channel, the invariant mass of the system that recoils against a single pion, $M_{recoil}(\pi)$, is shown in Fig. 6.5. In this distribution, both signal and non-signal pions have been taken into account.

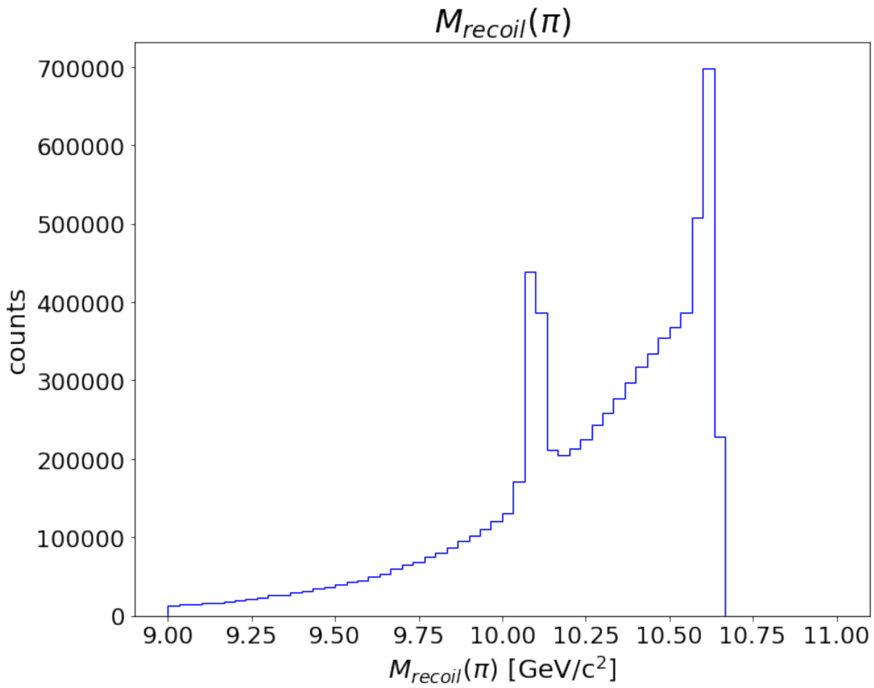

Figure 6.5: $M_{recoil}(\pi)$ distribution for the $e^+e^- \rightarrow \pi Z_b(10610) \rightarrow \pi\pi h_b(1P)$ decay, at the 10.805 GeV energy point of the scan.

In this plot two peaks can be observed: the first around the value corresponding to the sum of the mass of the $h_b(1P)$ state and the pion mass, i.e. when the pion is coming from the Z_b decay, and the other around the mass value of the $Z_b(10610)$ resonance, when the pion comes directly from the $\Upsilon(10753)$.

6.2 Track selection cuts

In order to extract the signal from real data samples, background has to be removed as much as possible. To achieve this, some selections need to be applied to remove tracks coming from the beam-induced background and also the so-called *fake* and *clone tracks*.

In fact, the high occupancy of the innermost detectors represents a major challenge for track reconstruction since a large number of hits measured by these detectors are related to beam-background sources and not to the primary interaction. Therefore, the algorithm may misidentify wrong combinations of hits as particles tracks. These bad tracks also degrade the overall tracking performance, thus they must be removed.

Fake tracks are composed of wrong combinations of hits, not associated to real particles. However, these tracks are relatively easy to reject. In fact, beam background tracks not always originate from the interaction point (IP) and usually have a boost along the z-axis. Fake tracks also do not necessarily arrive from the IP, as opposed to signal tracks which instead are produced close to the IP.

Also, beam background and fake tracks are expected to have lower momenta compared to signal particles, therefore they will not cross all four layers of the

SVD detector.

The variables that have been studied to identify the *track selection cuts* are:

- dr: the transverse distance of the point of closest approach (POCA) of the track with respect to IP.
- dz: the axial distance of the POCA of the track with respect to IP.
- $nSVDHits$: the number of SVD hits associated to the track.

The distributions of these variables have been inspected for both signal pions and background tracks, from the MC samples already studied in the previous section. To account for the background tracks, only fakes have been used for this study, due to their sufficiently high statistics in the sample. They have been identified as tracks not matched with a generated MC particle.

The distributions obtained from the *signal MC sample* for the $e^+e^- \to \pi^+\pi^- h_b(1P)$ decay are shown in Fig. 6.6.

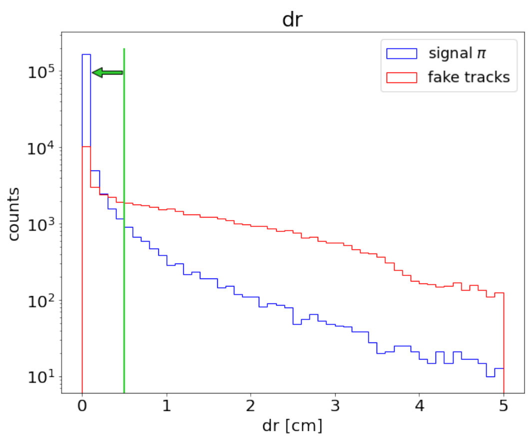

(a)

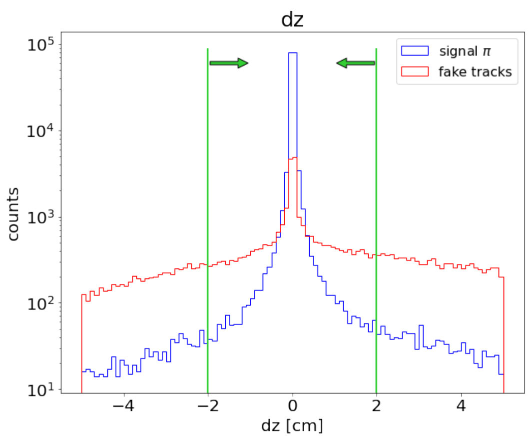

(b)

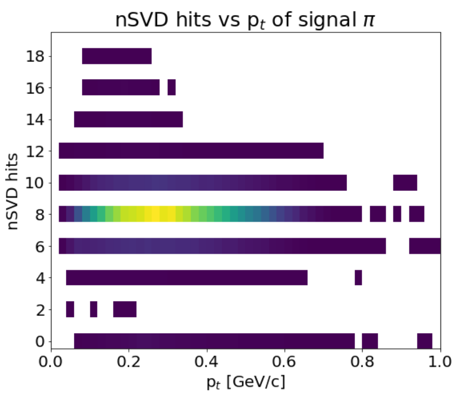

(c)

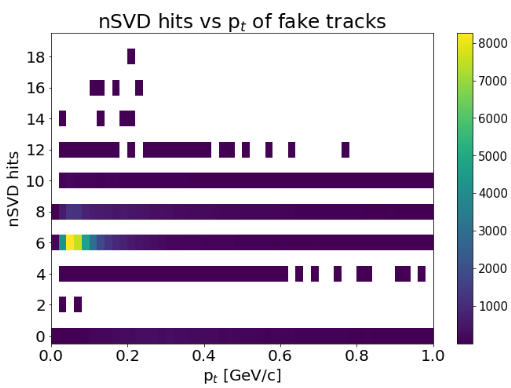

(d)

Figure 6.6: Distributions of dr, dz and $nSVDHits$ for both signal pions and fake tracks from $e^+e^- \to \pi^+\pi^- h_b(1P)$ decay. The green lines show the chosen cuts.

As expected, the fake track distributions of dr and dz are broader compared to the ones of signal tracks.

Furthermore, as already seen in previous studies, real tracks usually cross all four layers of the SVD. Fake tracks, instead, have very low momentum, as can be seen in Fig. 6.6d, and therefore are not expected to reach the last layer of the SVD, since they will be stopped by the material or will keep curling in the detector due to the effect of the magnetic field.

The same distributions have also been inspected for the Z_b *signal MC sample*. The results are shown in Fig. 6.7.

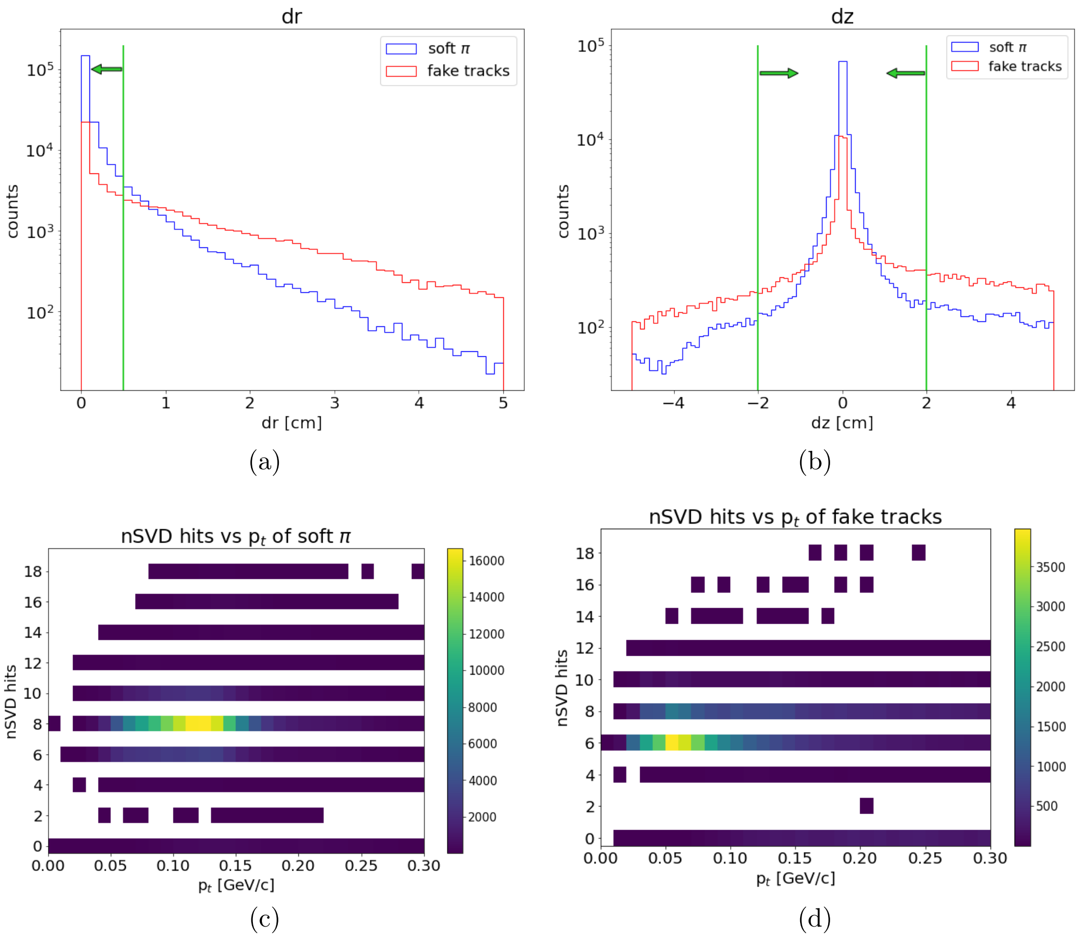

Figure 6.7: Distributions of dr, dz and $nSVDHits$ for both signal soft pions and fake tracks from $e^+e^- \to \pi Z_b(10610) \to \pi\pi h_b(1P)$ decay. The green lines show the chosen cuts.

As previously discussed, due to the kinematics of this decay, pions produced with the Z_b state are expected to have a very low momentum. In this particular sample, the value of the center-of-mass energy in the collisions allows most soft pions to still have enough energy to cross all four layers of the SVD detector. In fact, just a small fraction of these tracks is measured with only 6 SVD hits. Fake tracks, instead, can only reach the first three layers of the detector.

From what has been observed in the previous distributions, the chosen *track selection cuts* are:

- $dr < 0.5$ cm
- $|dz| < 2$ cm
- $nSVDHits > 6$

The cuts on dr and dz allow to select events produced close to the IP regions, while the cut on the number on SVD hits is used to pick only tracks which leave a signal on all the four layers of the SVD.

These will be applied to signal pions of both the *signal MC sample* and the Z_b *signal MC sample*.

6.3 Efficiency of track selection cuts

The efficiency of the *track selection cuts* will now be discussed.

Firstly, an estimate of the overall efficiency has been evaluated as:

$$\text{Efficiency}_{cuts} = \frac{N_{\text{rec with cuts}}}{N_{rec}}$$

where N_{rec} is the number of reconstructed signal pions and $N_{\text{rec with cuts}}$ is the number of reconstructed signal pions that passed the selection cuts.

For the *signal MC sample*, the efficiency has been computed using simulated data from the four energy points of the scan. The overall efficiency value with the corresponding binomial error is:

$$\text{Efficiency}_{cuts} = 0.8460 \pm 0.0008$$

For the Z_b *signal MC sample*, instead, only data from the last energy point of the scan have been used. The measured efficiency value and the binomial error are:

$$\text{Efficiency}_{cuts} = 0.714 \pm 0.001$$

The lower efficiency value for the Z_b *signal MC sample* is related to the fact that the cut on the number of SVD hits removes the small fraction of soft pions that can only reach the first three layers of the detector.

In general, for both samples, the track selection cuts show an overall good efficiency.

Then, the efficiency of the track selection cuts has also been evaluated as a function of the transverse momentum p_t and cosine of the polar angle $cos\theta$ of the reconstructed signal pions, as follows:

$$\text{Efficiency}_{cuts}(p_t, cos\theta) = \frac{N_{\text{rec with cuts}}(p_t, cos\theta)}{N_{rec}(p_t, cos\theta)}$$

where $N_{rec}(p_t, cos\theta)$ and $N_{\text{rec with cuts}}(p_t, cos\theta)$ are, respectively, the number of reconstructed signal pions without and with the selection cuts, evaluated in each bin of p_t and $cos\theta$.

To define the optimal width of the p_t bins, a study of p_t resolution has been conducted using MC truth-related information, which can be found in Appendix F.

The bi-dimensional distribution obtained from the *signal MC sample* is shown in Fig. 6.8.

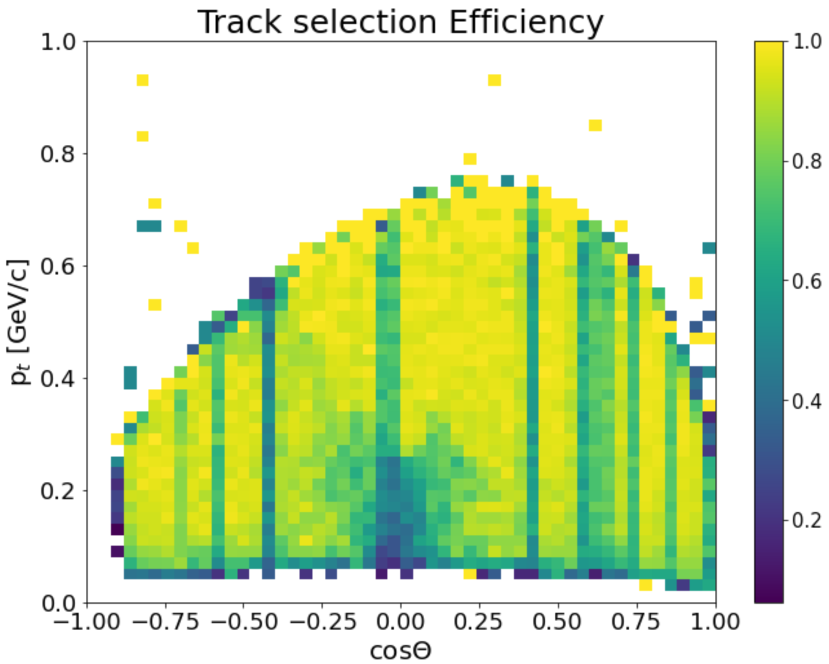

Figure 6.8: 2D distribution for the efficiency of track selection cuts in bins of p_t and $cos\theta$, studied for the $e^+e^- \rightarrow \pi\pi h_b(1P)$ decay.

The low efficiency values observed in the region around $cos\theta$=0 and low p_t are related to very low momentum pions with tracks perpendicular to the solenoid axis. Due to the effect of the magnetic field, these particles keep curling in the detector, leaving several hits in the same space region, making the tracks harder to be reconstructed.

In the distribution, we can also observe that at certain fixed values of $cos\theta$ the efficiency drops at very low values. This is related to the geometry of the detector; in particular, in the SVD there are some blind regions at certain values of $cos\theta$, due to the presence of non-active materials. For tracks that cross the detector in these regions, only 6 hits are measured and, therefore, using the selection cuts they are excluded.

The efficiency evaluated for the Z_b *signal MC sample*, instead, is shown in Fig.6.9.

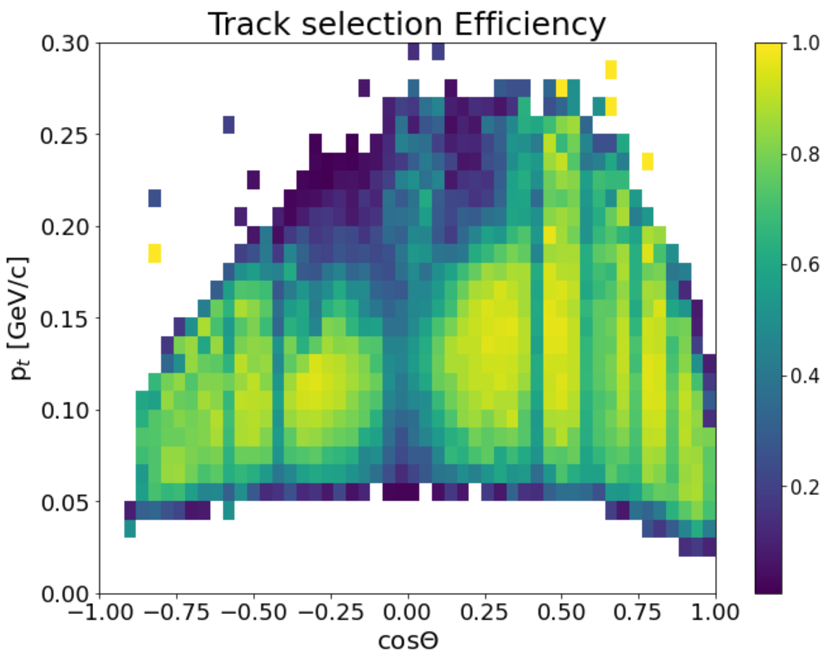

Figure 6.9: 2D distribution for the efficiency of track selection cuts in bins of p_t and $cos\theta$, studied for the $e^+e^- \to \pi Z_b(10610) \to \pi\pi h_b(1P)$ decay.

Even in this case, both observations made for the $e^+e^- \to \pi\pi h_b(1P)$ channel are still valid. The overall efficiency is lower compared to the other channel, due to the fact that reconstructed soft pions have generally very low momenta, and therefore the reconstruction performance is degraded. It is also important to note that there are no tracks with momentum lower than 50 MeV/c, with the exception of the ones reconstructed in the very forward direction. This is possible thanks to the asymmetrical geometry of the SVD detector. In this region of p_t and $cos\theta$, the efficiency is also pretty good.

Effects of correlation between the two pions

In the previous section, the efficiency of track selection cuts has been evaluated on the single reconstructed tracks.

For the $e^+e^- \to \pi\pi h_b(1P)$ channel, in particular, where the transition to the $h_b(1P)$ state happens with the emission of a pion pair, the effects of correlation between the two pions must be taken into account. In fact, the reconstruction and selection of two correlated pions might have a different efficiency compared to the product of efficiencies related to single pions.

To evaluate the effect of this correlation, the ratio between the product of single pion selection efficiencies and the selection efficiency of the pion pair is measured as follows:

$$\frac{Eff_{(\pi^+)} \cdot Eff_{(\pi^-)}}{Eff_{(\pi^+\pi^-)}}$$

where $Eff_{(\pi^+)}$ and $Eff_{(\pi^-)}$ are the selection efficiencies measured for single signal positive and negative pions, respectively. $Eff_{(\pi^+\pi^-)}$ is the efficiency for the simultaneous reconstruction and selection of the two pions produced in the decay. It is important to note that efficiency values found in the previous section have been measured considering both positive and negative pions together. For this study instead the two samples have been separated; however, as can be seen in Appendix G, the two samples have very similar efficiency distributions.

These quantities have been evaluated using the *signal MC sample*.

In Fig. 6.10, the measured ratio is shown in a two-dimensional histogram, in bins of the reconstructed p_t for π^+ and π^-.

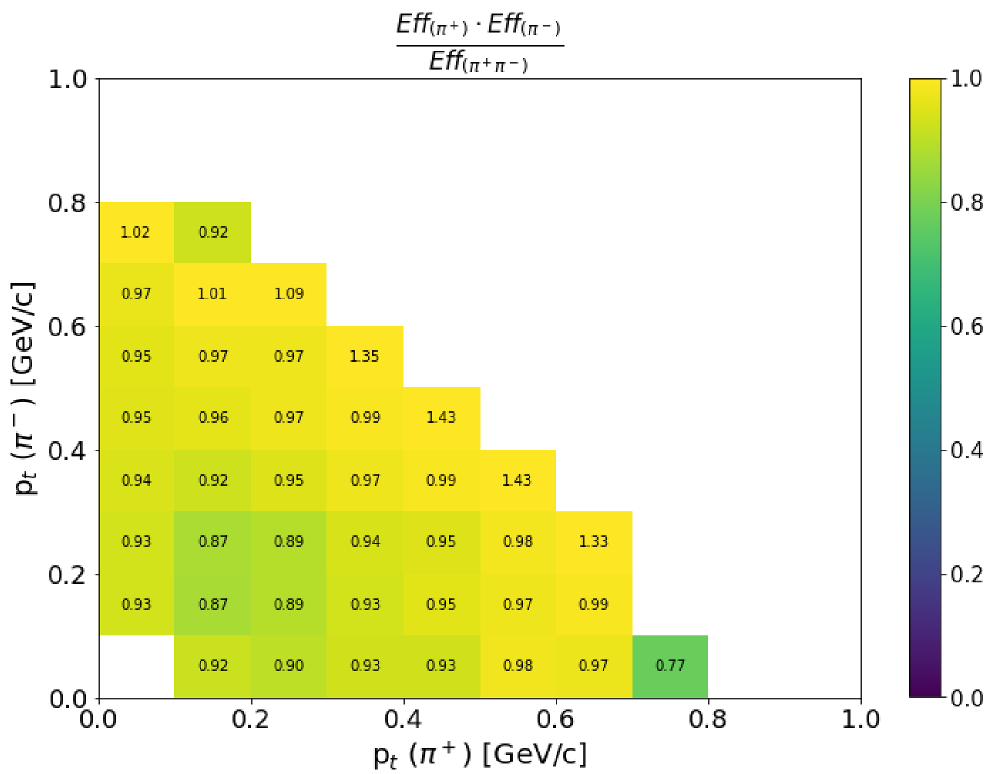

Figure 6.10: Ratio of the product of single pions selection efficiencies and the selection efficiency of the pion pair, in bins of reconstructed p_t for π^+ and π^-.

The plot shows that, overall, the ratio between the two efficiency is slightly lower than one, indicating that the correlation between the two pions increases the efficiency of reconstruction and selection compared to the product of efficiencies for single pions.

The differences are small, except for a few bins, in which the product of efficiencies is much higher (or lower) than the one evaluated for the pion pair. This effect is observed in a region of the pion pair p_t space where very few tracks are found, as can be seen in Fig. 6.1.

The same ratio has also been evaluated in bins of the reconstructed $cos\theta$ for π^+ and π^-, as shown in Fig. 6.11.

The overall difference between the two quantities is small; only in regions around $cos\theta = 0$ the product of efficiencies is slightly lower than the one measured for the pion pair, which means that in the direction perpendicular to the

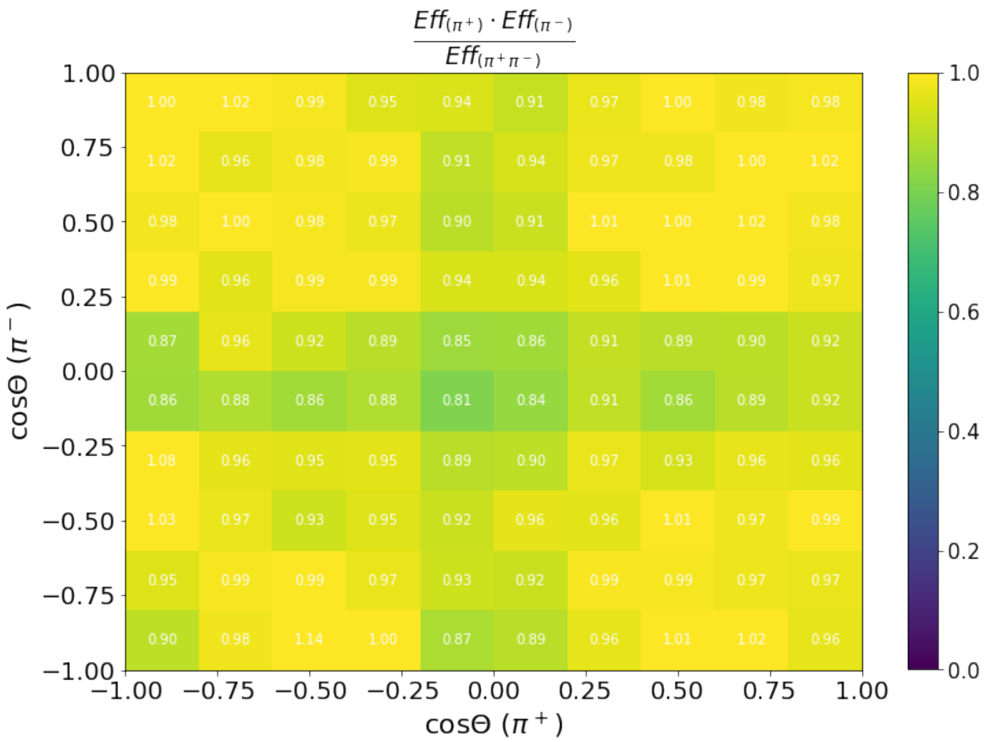

Figure 6.11: Ratio of the product of single pions selection efficiencies and the selection efficiency of the di-pion, in bins of reconstructed *cosθ* for π^+ and π^-.

solenoid axis there is a higher probability of reconstructing and selecting a pion pair compared to the one for single pions.

Chapter 7

Validation with control channel

In this chapter, the efficiency of the track selection cuts evaluated in Section 6.3 with MC samples will be validated using experimental data belonging to a well-known physics process.

In Section 7.1 the chosen control sample will be presented. In Section 7.2 the MC and data samples used for this study will be discussed. Then, in Section 7.3 the fit strategy to evaluate the efficiency and the results will be presented.

The plots in the following sections have been made using the Matplotlib Python library.

7.1 Control channel

The chosen control channel $D^{*+} \to \pi^+ D^0 \to \pi^+ K^- \pi^+$, with $BR(D^0 \to K^- \pi^+) = (3.95 \pm 0.03)\%$, is shown in Fig. 7.1.

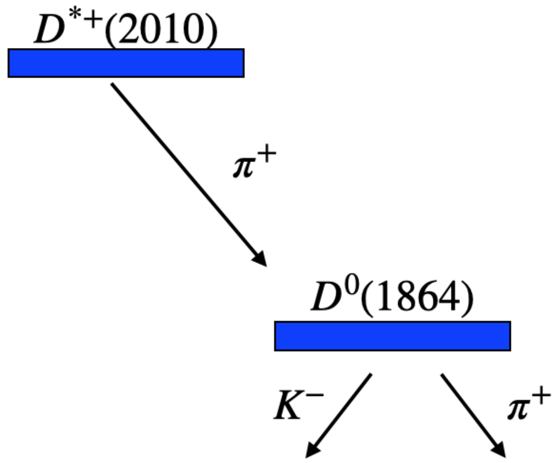

Figure 7.1: $D^{*+} \to \pi^+ D^0 \to \pi^+ K^- \pi^+$ decay channel, with $BR(D^0 \to K^- \pi^+) = (3.95 \pm 0.03)\%$.

This decay channel has been chosen because it has similar characteristics to the two decay processes studied in this analysis. In fact, the $D^{*+} \to \pi^+ D^0$ transition has a limited phase space, therefore the pion produced with the D^0

state is expected to have a very low momentum, just as observed for the pions from the direct decays of the $\Upsilon(10753)$ resonance.

A comparison between the transverse momentum distributions of reconstructed signal pions from both the D^{*+} and $\Upsilon(10753)$ decays is shown in Fig. 7.2. For the $e^+e^- \to \pi^+\pi^- h_b(1P)$ and $e^+e^- \to \pi Z_b(10610) \to \pi\pi h_b(1P)$ decays, the *signal MC sample* and the Z_b *signal MC sample*, already studied in the previous chapter, have been used; instead, for the decay $D^{*+} \to \pi^+ D^0 \to \pi^+ K^- \pi^+$, another MC sample has been used, which will be discussed in the next section.

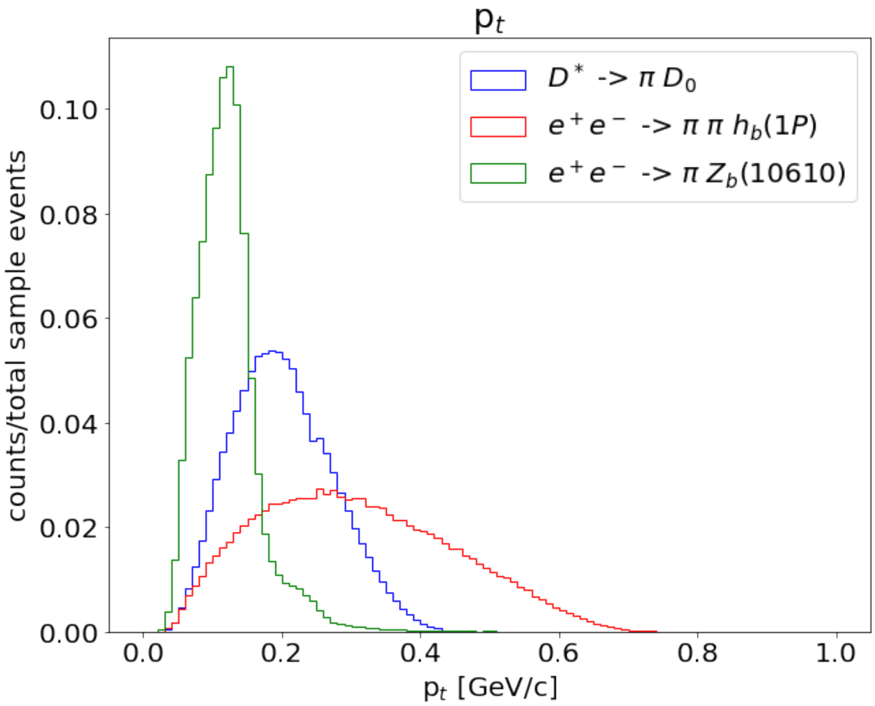

Figure 7.2: Normalized distributions of transverse momentum of reconstructed signal pions from $D^{*+} \to \pi^+ D^0 \to \pi^+ K^- \pi^+$ (blue), $e^+e^- \to \pi^+\pi^- h_b(1P)$ (red) and $e^+e^- \to \pi Z_b(10610) \to \pi\pi h_b(1P)$ (green) decays.

7.2 Studies on MC and data samples

The $D^{*+} \to \pi^+ D^0 \to \pi^+ K^- \pi^+$ decay channel has been studied using both MC and data samples.

Both samples are composed of events produced at the center-of-mass energy of the $\Upsilon(4S)$ resonance, i.e. 10.58 GeV, and also at the four energies of the scan previously discussed. The MC simulation includes decays from $B\bar{B}$, $u\bar{u}$, $d\bar{d}$, $s\bar{s}$, $c\bar{c}$ and $\tau\tau$ processes.

To reconstruct the D^{*+} state, an exclusive strategy has been applied for the decay chain shown in Fig. 7.1. The following selections have been used for the reconstruction on both the MC and data samples.

- For K^- and π^+ from the D^0 decay, only high purity lists of candidates have been selected.

- For the D^0 decay reconstruction, the D^0 mass has been constrained between 1.8 GeV/c^2 and 1.9 GeV/c^2.
- For the D^{*+} decay reconstruction, the D^{*+} mass has been constrained between 1.9 GeV/c^2 and 2.1 GeV/c^2.
- A simultaneous fit on the entire decay chain has also been performed using the *TreeFitter*, which is a global fitting tool used to find the best decay vertex positions and momenta for the given decay hypothesis. For this step, the D^0 mass was also constrained using the PDG value.

The distribution of the mass of the reconstructed D^{*+}, for both MC and data, is shown in Fig. 7.3. In the following plot, both the signal and the background events are included. Due to the higher luminosity of the MC sample compared to the data, both distributions have been normalized over the total number of events of each sample.

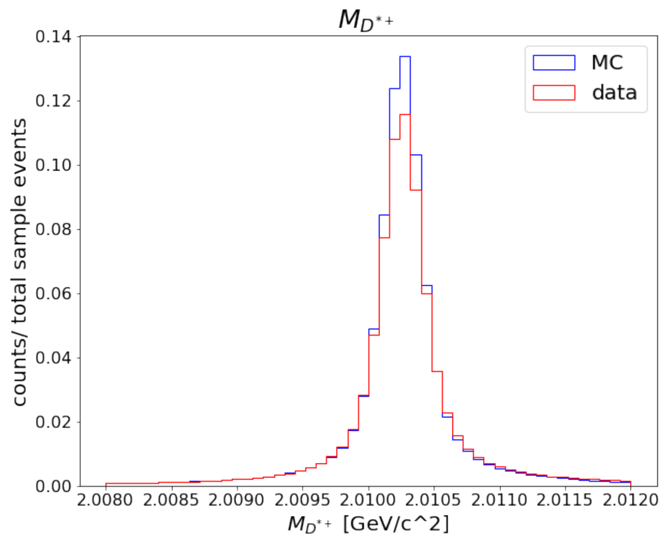

Figure 7.3: Normalized mass distributions of reconstructed D^{*+} from the $D^{*+} \to \pi^+ D^0 \to \pi^+ K^- \pi^+$ decay, for both MC (blue) and data (red) samples.

The two mass distributions show an overall good agreement, with an exception for the total yield. However, this is not relevant to the goal of this study.

7.3 Fit strategy and results

To validate the track selection efficiency of low momentum pions, the cuts discussed in Section 6.2 have been applied to pions directly produced in the $D^{*+} \to D^0$ transitions, which will be named *soft pions* from now on.

In this way, each sample has been divided into two, one in which pions have passed the cut and the other in which they do not pass the cut. These will be called *"passed"* and *"not passed" samples*, respectively.

In order to evaluate the efficiency as a function of the soft pion transverse momentum, the samples have been separated in different bins of p_t, of 10 MeV/c each. Events with p_t less than 50 MeV/c and more than 400 MeV/c have not been studied due to low statistics.

Then, the reconstructed D^{*+} mass distributions for both the "passed" and "not passed" samples have been fitted simultaneously. The fit function has been defined as a convolution of a Johnson's S_U distribution and a 1^{st} order Chebychev polynomial, to account for the signal and background shapes.

The total yield and the efficiency have been left as common free parameters to be calculated by the fit and have been defined as follows.

$$yield_{tot} = yield_{passed} + yield_{not\ passed}$$

$$yield_{passed} = yield_{tot} \cdot Eff$$

$$yield_{not\ passed} = yield_{tot} \cdot (1 - Eff)$$

Performing a simultaneous fit on the two "passed" and "not passed" samples allows to obtain an efficiency value and uncertainty that already take into account the correlation between the two.

The fit range has been defined from 2.008 GeV/c^2 to 2.012 GeV/c^2. Maximum likelihood fits have been performed on unbinned samples using the RooFit library of the ROOT analysis framework.

This strategy has been applied to both MC and data samples.

An example of the simultaneous fit in the p_t bin between 0.10 GeV/c and 0.11 GeV/c, for both MC and data, can be found in Fig. 7.4 and Fig. 7.5. The fit parameters can be found in Appendix H.

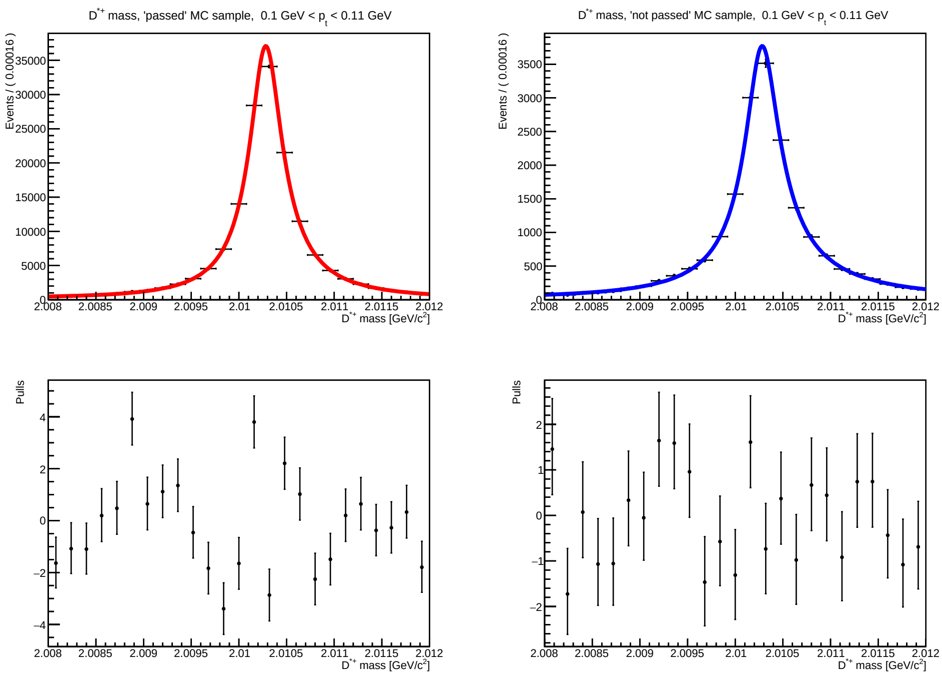

Figure 7.4: Simultaneous fit of the MC passed (red) and not passed (blue) samples for 0.10<p_t<0.11 GeV/c. Pulls distributions are also shown.

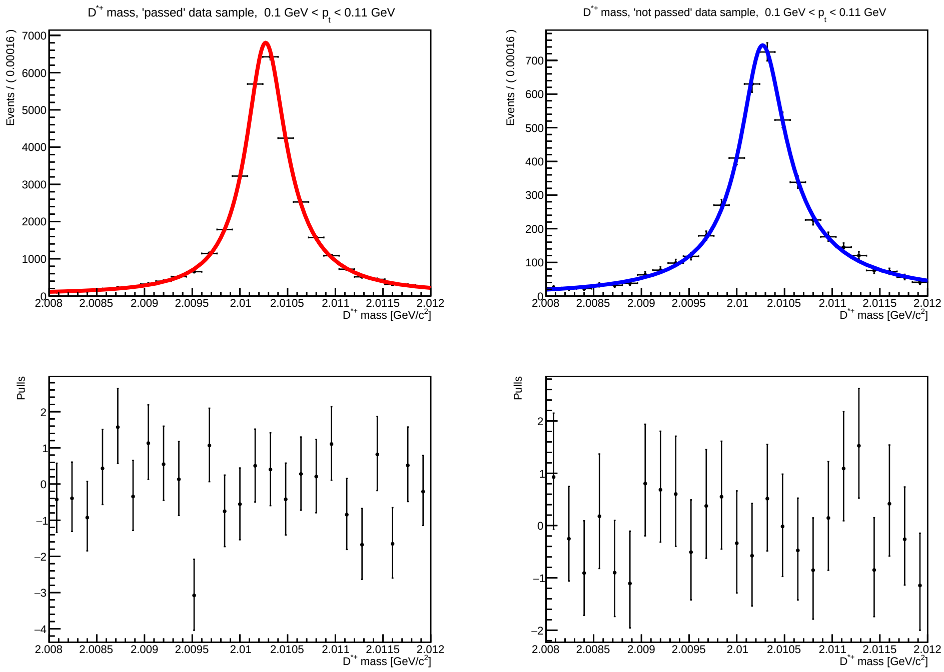

Figure 7.5: Simultaneous fit of the data passed (red) and not passed (blue) samples for $0.10 < p_t < 0.11$ GeV/c. Pulls distributions are also shown.

The efficiency values obtained in each bin of p_t from the fits, for MC and data, are shown in Fig. 7.6.

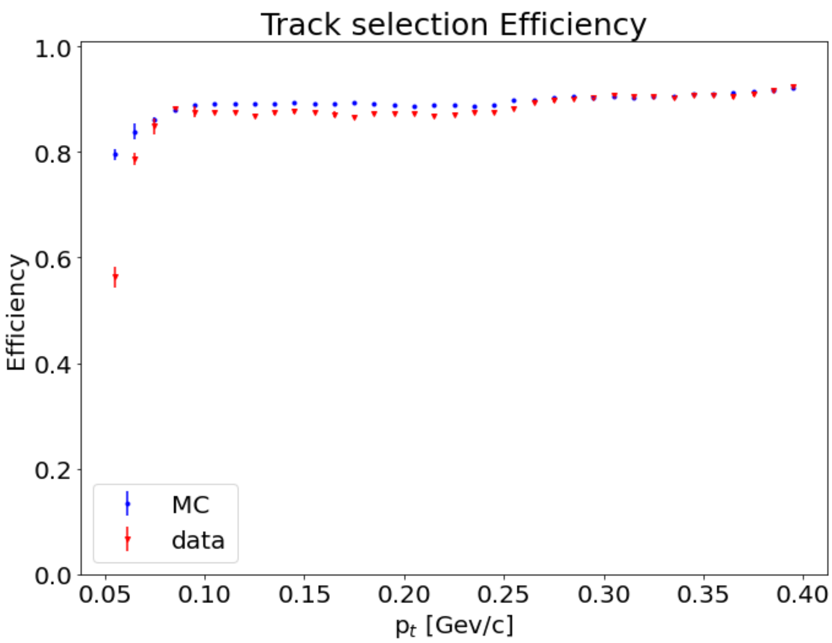

Figure 7.6: Comparison of track selection efficiency values as a function of p_t of soft pions, obtained from fit performed on MC (blue) and data (red) samples.

All these values can be found in Table H.3. The errors have been evaluated by the simultaneous fit.

Track selection efficiency for soft pions is overall very good for both MC and data, with values increasing with the transverse momentum from around 88% to 92%. For p_t lower than 80 MeV/c the efficiency decreases down to 80% for the MC and to 56% for the data sample.

To highlight any differences between the efficiency evaluated on data and MC, the following ratio has been computed as a function of the soft pions p_t.

$$R = \frac{Eff_{data}}{Eff_{MC}}$$

The results are shown in Fig. 7.7.

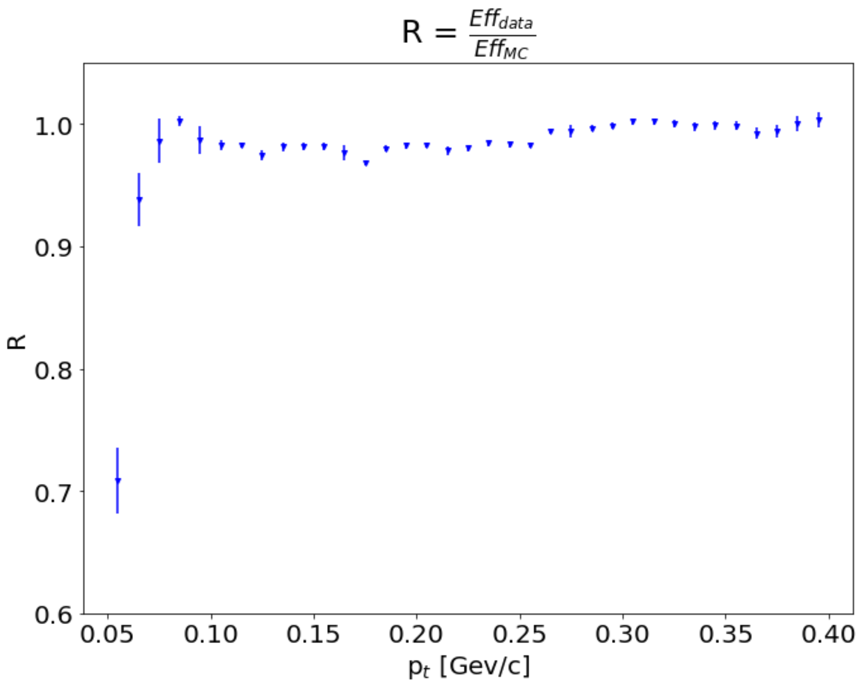

Figure 7.7: Ratio R evaluated as a function of the soft pions p_t.

All these values can also be found in Table H.3. Since the MC and data samples are not correlated, the errors have been evaluated using uncertainty propagation calculations.

The results show that, overall, the discrepancies between the tracks selection efficiencies for MC and data are small, around 1-3 %. An exception can be noticed for lower p_t values, where differences are more significant. This ratio will be used to correct data-MC discrepancies for the track selection when the fit on real data will be performed.

Chapter 8

Conclusion

Spectroscopy in the heavy quark sector is nowadays a field of strong interest for particle physics experiments. In particular, the discovery in 2003 of the $X(3872)$ resonance casted light on a new family of states observed in the $Q\bar{Q}$ sector spectra, whose nature could not be explained by conventional quarkonium models. In the last 20 years, several candidates belonging to this family of the so-called exotic states have been observed, but so far a unique interpretation of their nature has not been found.

In 2019, during an energy scan above the energy of the $\Upsilon(4S)$ state, a new exotic candidate named $\Upsilon(10753)$ was discovered by the Belle experiment. To better understand the nature of this state, more statistics was necessary, therefore, a new energy scan was performed in 2021 by the Belle II experiment, acquiring a total of 19.6 fb^{-1} luminosity around the resonance energy.

In this work, the $\Upsilon(10753) \to \pi^+\pi^- h_b(1P)$ decay has been studied. This transition can occur through a direct pure phase-space process, which is expected to be suppressed due to the violation of the HQSS; however, as already observed for the $\Upsilon(5S) \to \pi^+\pi^- h_b(mP)$ $(m = 1, 2)$ process, it could also take place passing through the intermediate charged state $Z_b(10610)$. Therefore, being the $\Upsilon(10753)$ resonance located around the $\pi Z_b(10610)$ production threshold, this decay channel allows to investigate the nature of both exotic candidates.

In this thesis, a blind analysis has been performed on Monte Carlo simulations and both decay chains have been reconstructed using an inclusive strategy.

To study these processes, it is important to accurately reconstruct the pions produced in the decays. Therefore, the performance of the latest available tracking reconstruction software was evaluated using MC simulation of both channels.

The distributions of several kinematic variables for signal pions were studied and, as expected, pions produced with the $Z_b(10610)$ resonance were found to have very low transverse momenta, around 80 MeV/c.

The distributions of the number of hits associated to signal tracks for each tracking detector have been inspected, also using a Particle Gun scan. It was observed that tracks of very low p_t pions were correctly found but they did not have any PXD hits attached to them, which degraded the overall reconstruction performance for these tracks. Retraining the CKF algorithm for this range of momenta or improving the track extrapolation toward the PXD might improve this issue in the future.

To evaluate tracking efficiency, several figures of merit were measured using MC truth-related information. For both channels, the finding charge efficiency was found to be overall good for p_t higher than 80 MeV/c. The charge efficiency, instead, decreased in the p_t region between 80 and 300 MeV/c.

The performance of the new Flip and Refit algorithm has also been evaluated. Using this new step of the tracking chain improved the measured charge efficiency values. In general, mostly low momentum tracks were flipped and the algorithm was found to not be effective below 80 MeV/c.

For the physics analysis, signals of both decay channels were studied using MC samples from the official Belle II production. In particular, the direct process is kinematically allowed for all four energies of the scan, while the one that proceeds through the $Z_b(10610)$ state is only possible for the last energy value.

The distributions of several kinematic variables for signal pions have been inspected, as well as recoil mass distributions to search for hints of the $h_b(1P)$ and $Z_b(10610)$ states.

To separate signal from fake tracks, selection cuts were studied. The overall efficiencies of these cuts for the two channels were found to be 85% and 71%, respectively.

The efficiency was also evaluated as a function of the transverse momentum and the cosine of the polar angle of signal pions. Low efficiency values were measured around $cos\theta = 0$ and for low p_t, due to very low momentum pions that keep curling in the detector, but also for certain values of $cos\theta$, corresponding to the SVD blind regions.

The effects of correlation between the two pions of the $e^+e^- \rightarrow \pi\pi h_b(1P)$ decay were also evaluated. It was found that correlation slightly increased the selection efficiency compared to the product of efficiencies evaluated for the single pions.

The efficiency of the track selection cuts was then validated using the $D^{*+} \rightarrow \pi^+ D^0 \rightarrow \pi^+ K^- \pi^+$ control channel, with both MC and data samples. The ratio R between the efficiency measured for data and MC was evaluated, showing that, overall, the discrepancies between two are small, only of a few %, with the exception of very low p_t values for which differences are more significant.

The future steps for the study of these decay channels will consist of defining a fitting strategy for the signal using MC samples and then, once the analysis will be unblinded by the internal referee committee, of performing a fit on real data of the scan.

Appendix A

Decay tables

Listing A.1: EvtGen decay table used for the generation of $\Upsilon(10753) \to \pi^+\pi^- h_b(1P)$ MC events.

```
[vpho -> pi pi h_b(1P)]

Decay vpho
1.000 pi+ pi- h_b  PHSP;
Enddecay

Decay  h_b
0.492000000   gamma  eta_b
                                   HELAMP 1. 0. 1. 0.;
0.508000000   g  g
                                           PYTHIA 91;
Enddecay

Decay eta_b
1.0  g  g  PHOTOS PYTHIA 91;
Enddecay

End
```

Listing A.2: EvtGen decay table used for the generation of $\Upsilon(10753) \to \pi Z_b(10610) \to \pi\pi h_b(1P)$ MC events.

```
[vpho -> pi Zb(10610) -> pi pi hb(1P)]

Decay vpho
0.5 pi+ Zb(10610)- PHSP;
0.5 pi- Zb(10610)+ PHSP;
Enddecay

Decay Zb(10610)-
1.0 pi- h_b PHSP;
Enddecay

Decay Zb(10610)+
1.0 pi+ h_b PHSP;
Enddecay

Decay  h_b
0.492000000   gamma  eta_b
                                   HELAMP 1. 0. 1. 0.;
0.508000000   g  g
                                           PYTHIA 91;
Enddecay

Decay eta_b
1.0  g  g  PHOTOS PYTHIA 91;
Enddecay

End
```

Appendix B

Missing PXD hits association hypotheses

B.1 Wrong Charge assignment

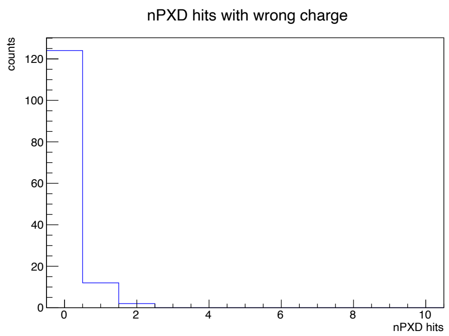

(a)

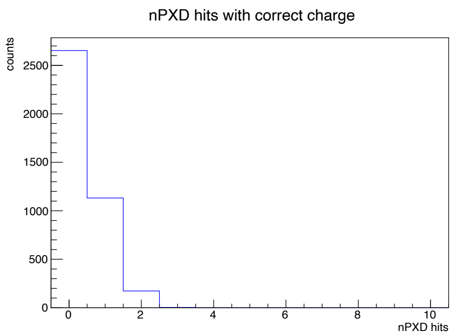

(b)

Figure B.1: Number of PXD hits distributions for single pions reconstructed in $\Upsilon(10753) \rightarrow \pi Z_b(10610) \rightarrow \pi\pi h_b(1P)$ decays. In (a) the condition requiring the wrong charge assignment is used; in (b) the right charge assignment is required. In both distributions a peak at 0 hits can be observed.

B.2 Particle seen in PXD

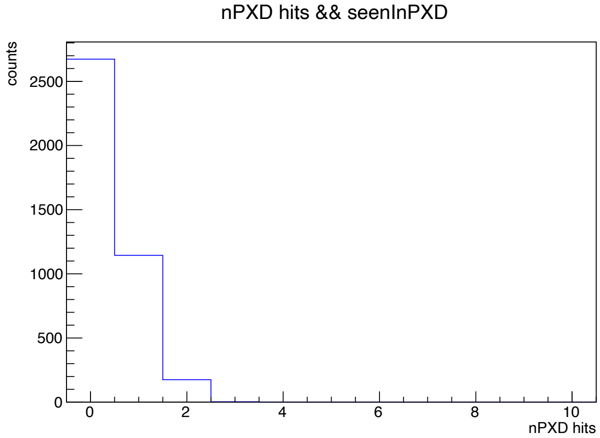

Figure B.2: Number of PXD hits distribution for single pions in $\Upsilon(10753) \to \pi Z_b(10610) \to \pi\pi h_b(1P)$ decays. The condition requiring that the MC particle is seen in the PXD is applied. A peak at 0 hits can be observed.

Appendix C

Effects of Geometrical Acceptance Cuts

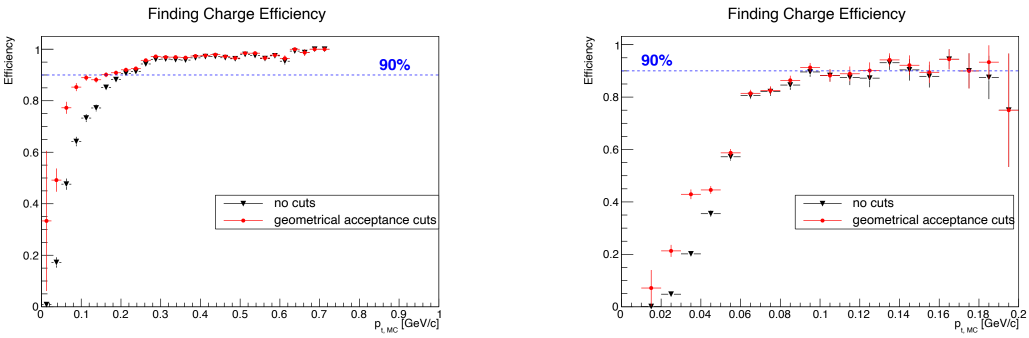

(a) (b)

Figure C.1: Finding Charge Efficiency evaluated for signal pions in $\Upsilon(10753) \to \pi^+\pi^- h_b(1P)$ (a) and $\Upsilon(10753) \to \pi Z_b(10610) \to \pi\pi h_b(1P)$ (b) decays. A comparison between the efficiency evaluated with (red) and without (black) geometrical acceptance cuts is shown.

Appendix D

Distributions used for Charge Efficiency evaluation

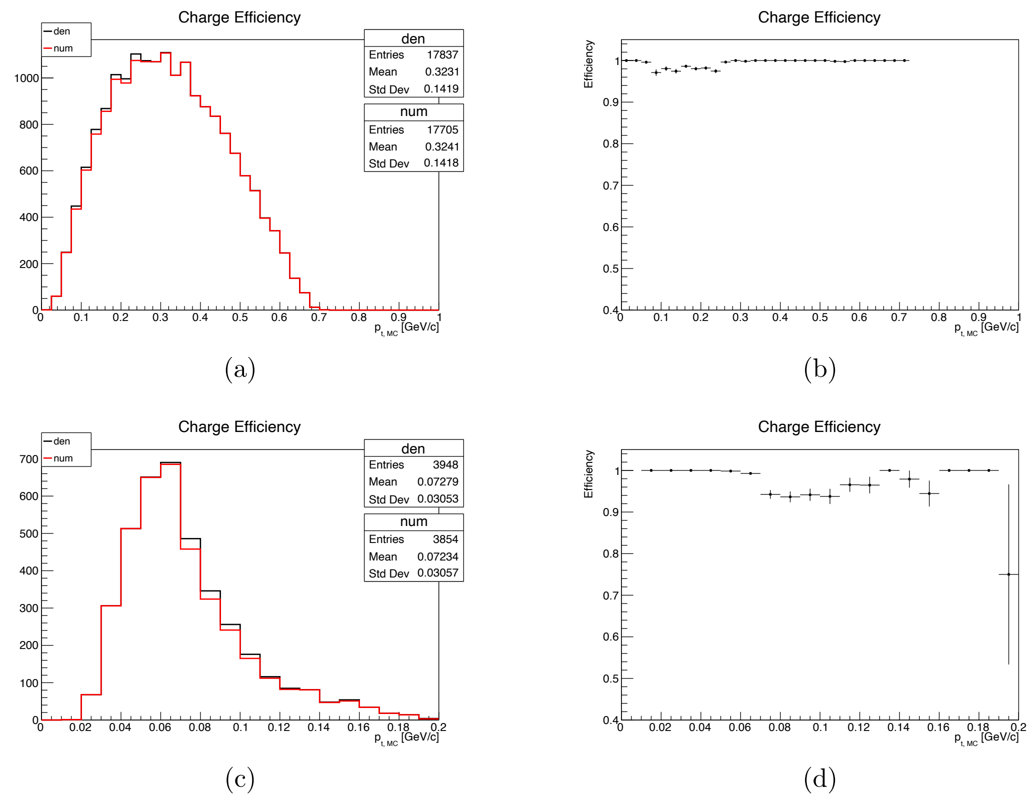

Figure D.1: Distributions used for the evaluation of the Charge Efficiency (left) and corresponding values (right), for signal pions of both $\Upsilon(10753) \to \pi^+\pi^- h_b(1P)$ (top) and $\Upsilon(10753) \to \pi Z_b(10610) \to \pi\pi h_b(1P)$ (bottom) decays. Flip and Refit is ON.

Appendix E

Kinematics variables distributions from $e^+e^- \to \pi^+\pi^- h_b(1P)$ decays

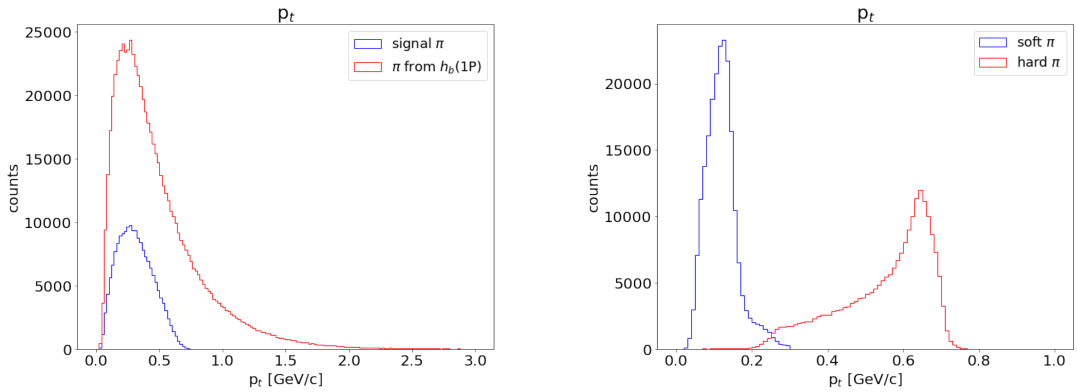

(a) (b)

Figure E.1: p_t distributions of pions reconstructed in $e^+e^- \to \pi^+\pi^- h_b(1P)$ (a) and $e^+e^- \to \pi Z_b(10610) \to \pi\pi h_b(1P)$ (b) decays.

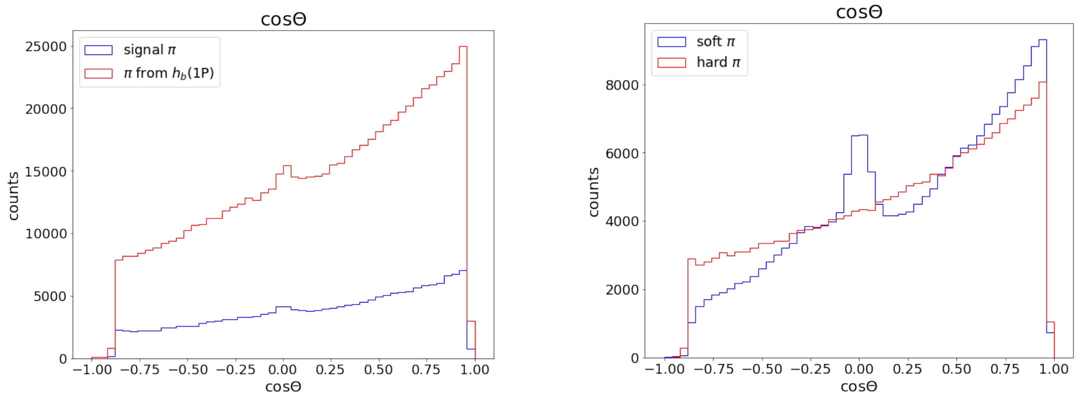

(a) (b)

Figure E.2: $\cos\theta$ distributions of pions reconstructed in $e^+e^- \to \pi^+\pi^- h_b(1P)$ (a) and $e^+e^- \to \pi Z_b(10610) \to \pi\pi h_b(1P)$ (b) decays.

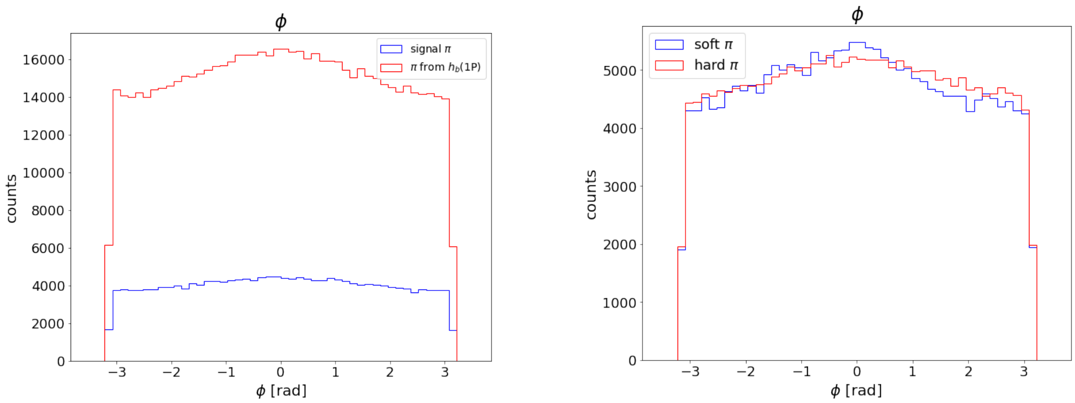

(a) (b)

Figure E.3: ϕ distributions of pions reconstructed in $e^+e^- \to \pi^+\pi^- h_b(1P)$ (a) and $e^+e^- \to \pi Z_b(10610) \to \pi\pi h_b(1P)$ (b) decays.

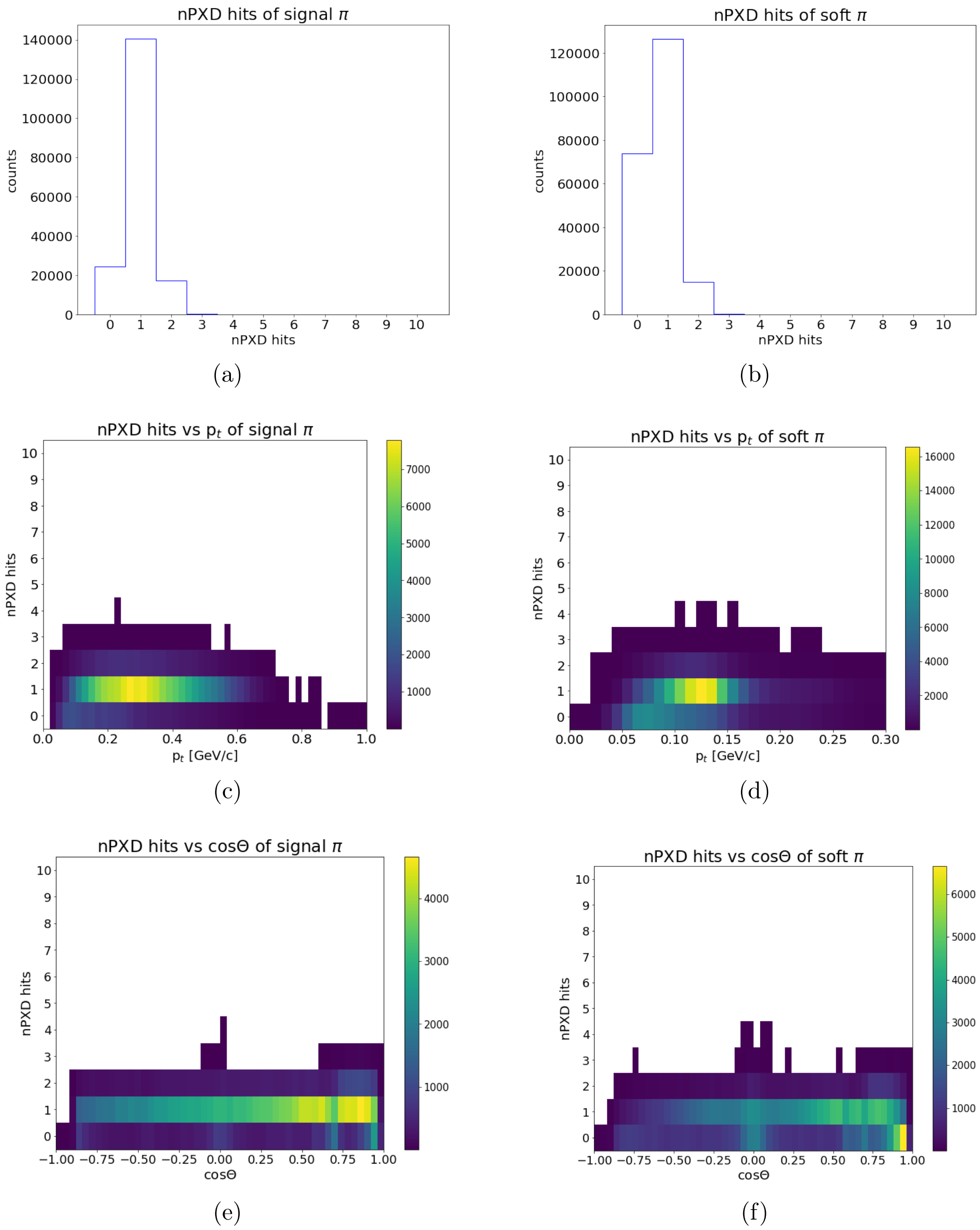

Figure E.4: Number of PXD hits distributions for signal pions reconstructed in $e^+e^- \to \pi^+\pi^- h_b(1P)$ (left) and $e^+e^- \to \pi Z_b(10610) \to \pi\pi h_b(1P)$ (right) decays. In second and third row, respectively, these distributions are shown as a function of p_t and cosθ.

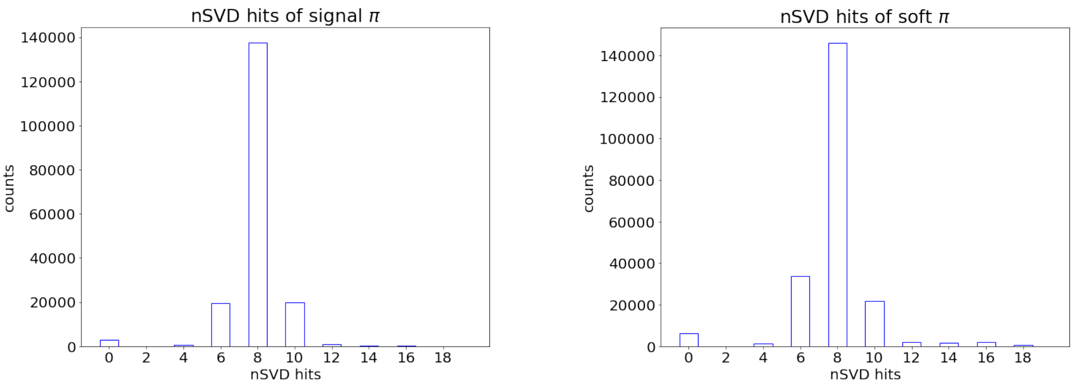

(a) (b)

Figure E.5: Number of SVD hits distributions of signal pions reconstructed in $e^+e^- \to \pi^+\pi^- h_b(1P)$ (a) and $e^+e^- \to \pi Z_b(10610) \to \pi\pi h_b(1P)$ (b) decays.

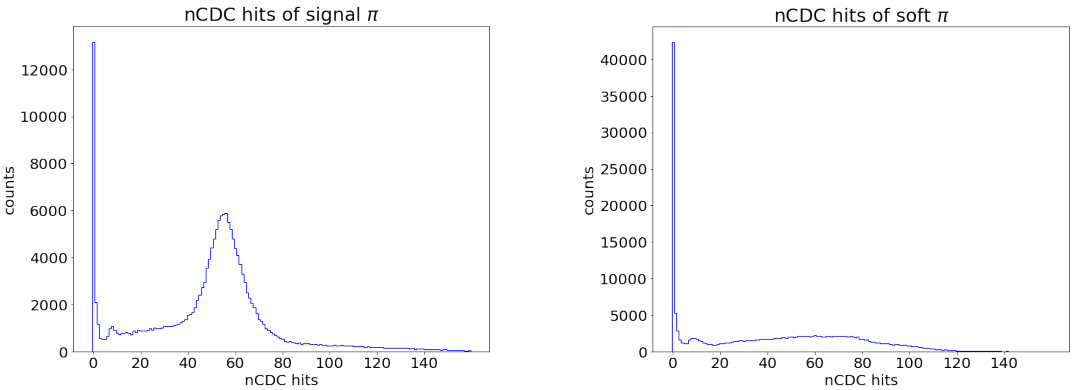

(a) (b)

Figure E.6: Number of CDC hits distributions of signal pions reconstructed in $e^+e^- \to \pi^+\pi^- h_b(1P)$ (a) and $e^+e^- \to \pi Z_b(10610) \to \pi\pi h_b(1P)$ (b) decays.

Appendix F

Study of p_t resolution

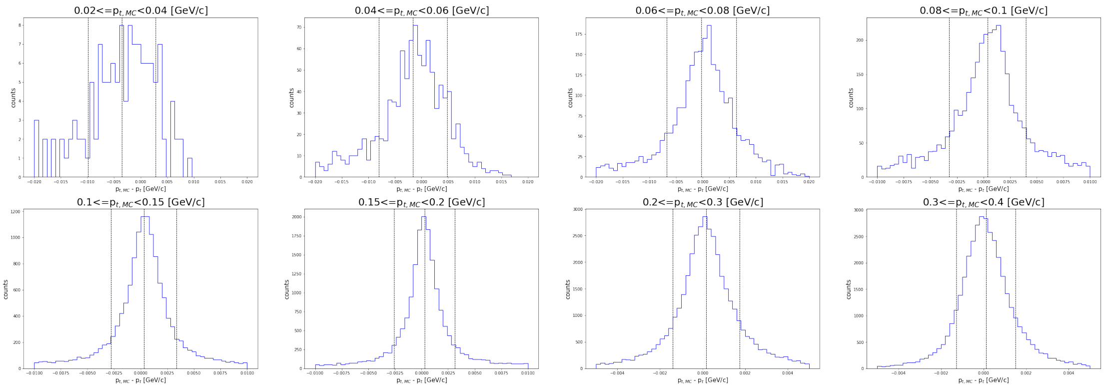

(a)

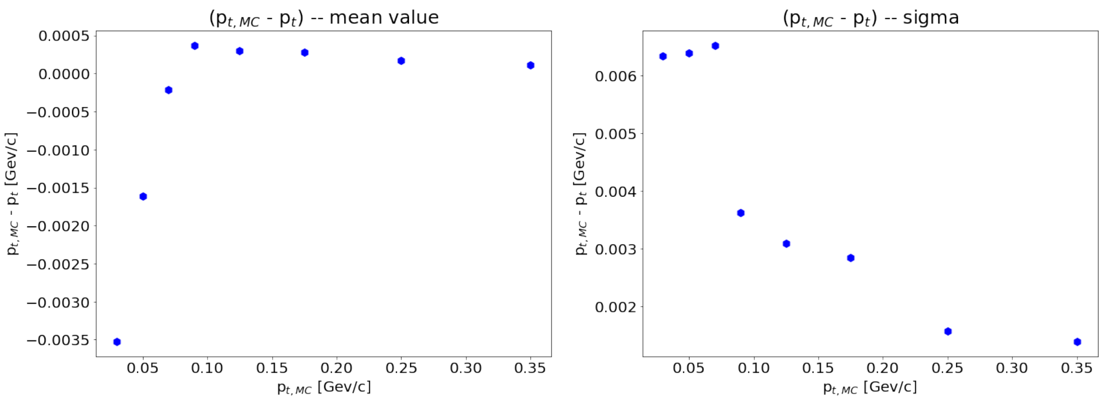

(b)

Figure F.1: Residuals p_t distributions (a) and measured mean values and sigmas (b) for signal pions reconstructed in $e^+e^- \to \pi^+\pi^- h_b(1P)$ decay.

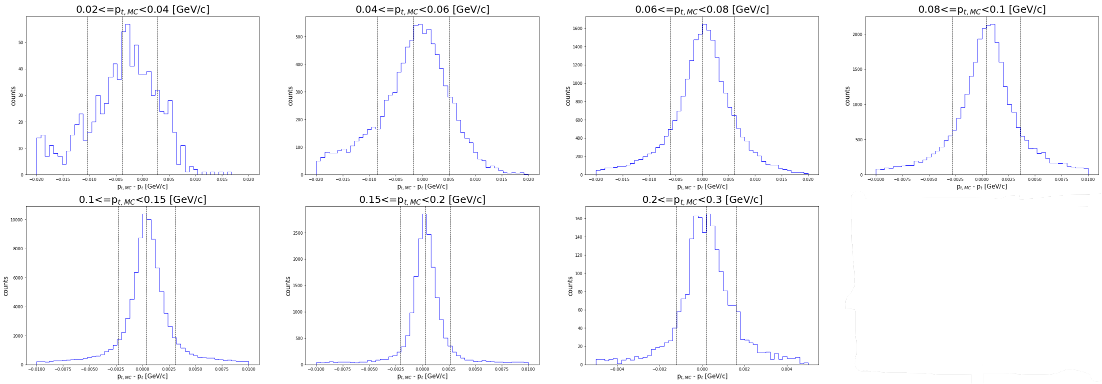

(a)

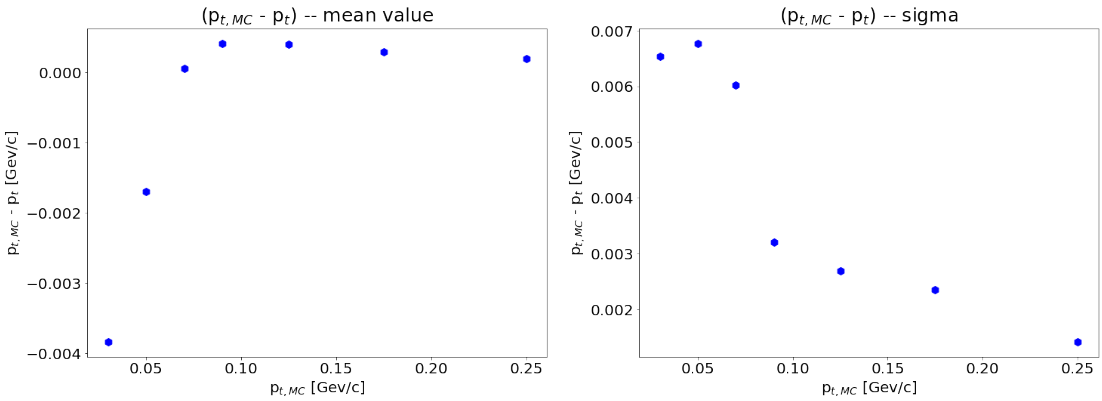

(b)

Figure F.2: Residuals p_t distributions (a) and measured mean values and sigmas (b) for signal pions reconstructed in $e^+e^- \to \pi Z_b(10610) \to \pi\pi h_b(1P)$ decay.

Appendix G

Track selection cuts efficiency for π^+ and π^-

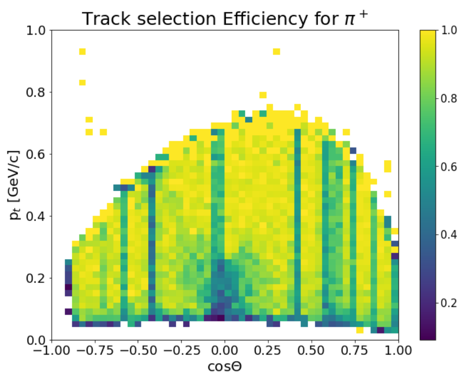

(a)

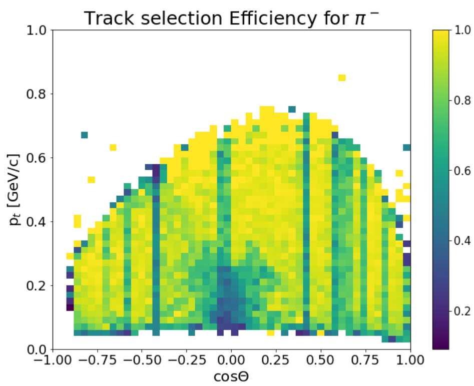

(b)

Figure G.1: 2D distributions for the efficiency of track selection cuts in bins of p_t and $cos\theta$, studied for π^+ (a) and π^- (b) in the $e^+e^- \to \pi\pi h_b(1P)$ decay.

Appendix H

Track selection efficiency validation

H.1 Fit parameters from MC and data examples

Table H.1: Parameters of simultaneous fit performed on the MC passed and not passed samples, for 0.10<p_t<0.11 GeV/c.

Parameter	**value ± error**
$yield_{tot}$	169792 ± 633
eff	0.891 ± 0.003
$nbkg_{pass}$	4101 ± 193
$delta_{pass}$	0.643 ± 0.002
$gamma_{pass}$	-0.067 ± 0.003
$lambda_{pass}$	0.0001761 ± 0.0000007
mu_{pass}	2.0102772 ± 0.0000008
$a1_{pass}$	-0.23 ± 0.06
$nbkg_{not}$	86 ± 12
$delta_{not}$	0.50 ± 0.02
$gamma_{not}$	-0.12 ± 0.01
$lambda_{not}$	0.000179 ± 0.000004
mu_{not}	2.010275± 0.000003
$a1_{not}$	-1.00 ± 0.5

Table H.2: Parameters of simultaneous fit performed on the data passed and not passed samples, for 0.10<p_t<0.11 GeV/c.

Parameter	**value ± error**
$yield_{tot}$	36227 ± 472
eff	0.875 ± 0.003
$nbkg_{pass}$	1432 ± 427
$delta_{pass}$	0.70 ± 0.03
$gamma_{pass}$	-0.11 ± 0.02
$lambda_{pass}$	0.000217 ± 0.000008
mu_{pass}	2.010259 ± 0.000004
$a1_{pass}$	-0.01 ± 0.02
$nbkg_{not}$	0 ± 1
$delta_{not}$	0.52 ± 0.04
$gamma_{not}$	-0.15 ± 0.03
$lambda_{not}$	0.00023 ± 0.00002
mu_{not}	2.01026± 0.00001
$a1_{not}$	-0.178 ± 0.003

H.2 Efficiency values and Ratio

Table H.3: Efficiency values evaluated from fit on MC and data and their ratio R.

p_t bin [GeV/c]	Eff_{MC}	$\pm err_{MC}$	Eff_{data}	$\pm err_{data}$	$Ratio$	$\pm err_{Ratio}$
(0.05, 0.06)	0.80	0.01	0.56	0.02	0.71	0.03
(0.06, 0.07)	0.84	0.02	0.79	0.01	0.94	0.02
(0.07, 0.08)	0.861	0.004	0.85	0.01	0.99	0.03
(0.08, 0.09)	0.879	0.003	0.8812	0.0004	1.002	0.004
(0.09, 0.1)	0.8881	0.0009	0.88	0.01	0.99	0.01
(0.1, 0.11)	0.891	0.003	0.875	0.003	0.983	0.004
(0.11, 0.12)	0.8915	0.0008	0.876	0.002	0.983	0.002
(0.12, 0.13)	0.891	0.004	0.868	0.002	0.974	0.004
(0.13, 0.14)	0.891	0.001	0.875	0.003	0.981	0.004
(0.14, 0.15)	0.893	0.001	0.876	0.003	0.981	0.003
(0.15, 0.16)	0.8913	0.0008	0.875	0.003	0.981	0.003
(0.16, 0.17)	0.8923	0.0008	0.871	0.006	0.977	0.007
(0.17, 0.18)	0.8934	0.0008	0.865	0.001	0.968	0.002
(0.18, 0.19)	0.8917	0.0008	0.874	0.002	0.980	0.003
(0.19, 0.2)	0.8887	0.0008	0.873	0.002	0.982	0.002
(0.2, 0.21)	0.8879	0.0008	0.872	0.002	0.983	0.002
(0.21, 0.22)	0.888	0.002	0.869	0.002	0.978	0.004
(0.22, 0.23)	0.8891	0.0008	0.872	0.002	0.980	0.003
(0.23, 0.24)	0.8878	0.0009	0.874	0.002	0.985	0.003
(0.24, 0.25)	0.8891	0.0008	0.874	0.002	0.983	0.002
(0.25, 0.26)	0.8972	0.0008	0.881	0.002	0.982	0.002
(0.26, 0.27)	0.8989	0.0008	0.894	0.002	0.994	0.002
(0.27, 0.28)	0.9030	0.0008	0.898	0.005	0.994	0.005
(0.28, 0.29)	0.9049	0.0008	0.902	0.002	0.996	0.002
(0.29, 0.3)	0.9034	0.0009	0.902	0.002	0.999	0.002
(0.3, 0.31)	0.905	0.001	0.907	0.002	1.002	0.003
(0.31, 0.32)	0.904	0.001	0.906	0.002	1.002	0.003
(0.32, 0.33)	0.905	0.001	0.905	0.003	1.001	0.003
(0.33, 0.34)	0.905	0.001	0.903	0.003	0.998	0.003
(0.34, 0.35)	0.909	0.001	0.908	0.003	0.999	0.004
(0.35, 0.36)	0.910	0.002	0.908	0.003	0.999	0.004
(0.36, 0.37)	0.912	0.002	0.905	0.004	0.992	0.005
(0.37, 0.38)	0.916	0.002	0.910	0.004	0.994	0.005
(0.38, 0.39)	0.916	0.002	0.917	0.005	1.000	0.006
(0.39, 0.4)	0.921	0.003	0.923	0.005	1.003	0.006

Bibliography

[1] Giulio Mezzadri and Stefano Spataro. “XYZ states: An experimental point-of-view”. In: *Reviews in Physics* 8 (2022), p. 100070. ISSN: 2405-4283. DOI: https://doi.org/10.1016/j.revip.2022.100070. URL: https://www.sciencedirect.com/science/article/pii/S2405428322000028.

[2] Nora Brambilla et al. “The XYZ states: Experimental and theoretical status and perspectives”. In: *Physics Reports* 873 (2020). The XYZ states: experimental and theoretical status and perspectives, pp. 1–154. ISSN: 0370-1573. DOI: https://doi.org/10.1016/j.physrep.2020.05.001. URL: https://www.sciencedirect.com/science/article/pii/S0370157320301915.

[3] J. E. Augustin et al. “Discovery of a Narrow Resonance in e^+e^- Annihilation”. In: *Phys. Rev. Lett.* 33 (23 1974), pp. 1406–1408. DOI: 10.1103/PhysRevLett.33.1406. URL: https://link.aps.org/doi/10.1103/PhysRevLett.33.1406.

[4] J. J. Aubert et al. “Experimental Observation of a Heavy Particle J”. In: *Phys. Rev. Lett.* 33 (23 1974), pp. 1404–1406. DOI: 10.1103/PhysRevLett.33.1404. URL: https://link.aps.org/doi/10.1103/PhysRevLett.33.1404.

[5] S. W. Herb et al. “Observation of a Dimuon Resonance at 9.5 GeV in 400-GeV Proton-Nucleus Collisions”. In: *Phys. Rev. Lett.* 39 (5 1977), pp. 252–255. DOI: 10.1103/PhysRevLett.39.252. URL: https://link.aps.org/doi/10.1103/PhysRevLett.39.252.

[6] S.-K. Choi et al. “Observation of a Narrow Charmoniumlike State in Exclusive $B^\pm \to K^\pm\pi^+\pi^- J/\psi$ Decays”. In: *Phys. Rev. Lett.* 91 (26 2003), p. 262001. DOI: 10.1103/PhysRevLett.91.262001. URL: https://link.aps.org/doi/10.1103/PhysRevLett.91.262001.

[7] E Kou et al. “The Belle II Physics Book”. In: *Progress of Theoretical and Experimental Physics* 2019.12 (Dec. 2019). ISSN: 2050-3911. DOI: 10.1093/ptep/ptz106. URL: http://dx.doi.org/10.1093/ptep/ptz106.

[8] Stephen Lars Olsen, Tomasz Skwarnicki, and Daria Zieminska. “Nonstandard heavy mesons and baryons: Experimental evidence”. In: *Reviews of Modern Physics* 90.1 (Feb. 2018). ISSN: 1539-0756. DOI: 10.1103/revmodphys.90.015003. URL: http://dx.doi.org/10.1103/RevModPhys.90.015003.

[9] S. Navas et al. “Review of particle physics”. In: *Phys. Rev. D* 110.3 (2024), p. 030001. DOI: 10.1103/PhysRevD.110.030001.

[10] LHCb collaboration. *Exotic hadron naming convention.* 2023. arXiv: 2206.15233 [hep-ex]. URL: https://arxiv.org/abs/2206.15233.

[11] B. Aubert et al. "Observation of a Broad Structure in the $\pi^+\pi^- J/\psi$ Mass Spectrum around 4.26 GeV/c^2". In: *Phys. Rev. Lett.* 95 (14 2005), p. 142001. DOI: 10.1103/PhysRevLett.95.142001. URL: https://link.aps.org/doi/10.1103/PhysRevLett.95.142001.

[12] Particle Data Group et al. "Review of Particle Physics". In: *Progress of Theoretical and Experimental Physics* 2020.8 (Aug. 2020), p. 083C01. ISSN: 2050-3911. DOI: 10.1093/ptep/ptaa104. eprint: https://academic.oup.com/ptep/article-pdf/2020/8/083C01/34673722/ptaa104.pdf. URL: https://doi.org/10.1093/ptep/ptaa104.

[13] M. Ablikim et al. "Precise measurement of the e+e→+J/ cross section at center-of-mass energies from 3.77 to 4.60 GeV". In: *Physical Review Letters* 118.9 (Mar. 2017). ISSN: 1079-7114. DOI: 10.1103/physrevlett.118.092001. URL: http://dx.doi.org/10.1103/PhysRevLett.118.092001.

[14] R. Mizuk et al. "Observation of a new structure near 10.75 GeV in the energy dependence of the e+e→ (nS)+ (n = 1, 2, 3) cross sections". In: *Journal of High Energy Physics* 2019.10 (Oct. 2019). ISSN: 1029-8479. DOI: 10.1007/jhep10(2019)220. URL: http://dx.doi.org/10.1007/JHEP10(2019)220.

[15] Xiang-Kun Dong et al. "Hadronic cross section of e+e annihilation at bottomonium energy region *". In: *Chinese Physics C* 44.8 (Aug. 2020), p. 083001. ISSN: 2058-6132. DOI: 10.1088/1674-1137/44/8/083001. URL: http://dx.doi.org/10.1088/1674-1137/44/8/083001.

[16] Zhi-Gang Wang. "Vector hidden-bottom tetraquark candidate: Y(10750) *". In: *Chinese Physics C* 43.12 (Dec. 2019), p. 123102. ISSN: 2058-6132. DOI: 10.1088/1674-1137/43/12/123102. URL: http://dx.doi.org/10.1088/1674-1137/43/12/123102.

[17] Ahmed Ali et al. "Interpretation of Yb(10750) as a tetraquark and its production mechanism". In: *Physics Letters B* 802 (2020), p. 135217. ISSN: 0370-2693. DOI: https://doi.org/10.1016/j.physletb.2020.135217. URL: https://www.sciencedirect.com/science/article/pii/S0370269320300216.

[18] Jaume Tarrús Castellà and Emilie Passemar. "Exotic to standard bottomonium transitions". In: *Physical Review D* 104.3 (Aug. 2021). ISSN: 2470-0029. DOI: 10.1103/physrevd.104.034019. URL: http://dx.doi.org/10.1103/PhysRevD.104.034019.

[19] Yu-Shuai Li, Zi-Yue Bai, and Xiang Liu. "Investigating the (10753)→(13DJ) transitions". In: *Physical Review D* 105.11 (June 2022). ISSN: 2470-0029. DOI: 10.1103/physrevd.105.114041. URL: http://dx.doi.org/10.1103/PhysRevD.105.114041.

[20] K.-F. Chen et al. "Observation of anomalous Upsilon(1S)pi+pi- and Upsilon(2S)pi+pi- production near the Upsilon(5S) resonance". In: *Physical Review Letters* 100.11 (Mar. 2008). ISSN: 1079-7114. DOI: 10.1103/physrevlett.100.112001. URL: http://dx.doi.org/10.1103/PhysRevLett.100.112001.

[21] I. Adachi et al. "First observation of the P-wave spin-singlet bottomonium states $h_b(1P) and h_b(2P)$". In: *Physical Review Letters* 108.3 (Jan. 2012). ISSN: 1079-7114. DOI: 10.1103/physrevlett.108.032001. URL: http://dx.doi.org/10.1103/PhysRevLett.108.032001.

[22] A. Bondar et al. "Observation of two charged bottomonium-like resonances in Y(5S) decays". In: *Physical Review Letters* 108.12 (Mar. 2012). ISSN: 1079-7114. DOI: 10.1103/physrevlett.108.122001. URL: http://dx.doi.org/10.1103/PhysRevLett.108.122001.

[23] Alexander Bondar and Roman Mizuk. *Status and new results on the Zb resonances*. 2013. arXiv: 1303.0101 [hep-ex]. URL: https://arxiv.org/abs/1303.0101.

[24] P. Krokovny et al. "First Observation of the Zb0(10610) in a Dalitz Analysis of Y(5S) -> Y(nS) pi0 pi0". In: *Physical Review D* 88.5 (Sept. 2013). ISSN: 1550-2368. DOI: 10.1103/physrevd.88.052016. URL: http://dx.doi.org/10.1103/PhysRevD.88.052016.

[25] Q. Wang et al. "The line shapes of the Zb(10610) and Zb(10650) in the elastic and inelastic channels revisited". In: *Physical Review D* 98.7 (Oct. 2018). ISSN: 2470-0029. DOI: 10.1103/physrevd.98.074023. URL: http://dx.doi.org/10.1103/PhysRevD.98.074023.

[26] T. Abe et al. *Belle II Technical Design Report*. 2010. arXiv: 1011.0352 [physics.ins-det]. URL: https://arxiv.org/abs/1011.0352.

[27] Valerio Bertacchi et al. "Track finding at Belle II". In: *Computer Physics Communications* 259 (2021), p. 107610. ISSN: 0010-4655. DOI: https://doi.org/10.1016/j.cpc.2020.107610. URL: https://www.sciencedirect.com/science/article/pii/S0010465520302861.

[28] S. Mondal et al. "Silicon vertex detector of the Belle II experiment". In: *Journal of Instrumentation* 19.02 (Feb. 2024), p. C02038. ISSN: 1748-0221. DOI: 10.1088/1748-0221/19/02/c02038. URL: http://dx.doi.org/10.1088/1748-0221/19/02/C02038.

[29] Ezio Torassa. "TOP detector for particle identification at Belle II". In: *International Journal of Modern Physics A* 39.26n27 (Sept. 2024). ISSN: 1793-656X. DOI: 10.1142/s0217751x24420144. URL: http://dx.doi.org/10.1142/S0217751X24420144.

[30] Yosuke Yusa. "The ARICH detector at Belle II experiment". In: *PoS* EPS-HEP2013 (2013), p. 556. DOI: 10.22323/1.180.0556.

[31] A. Kuzmin. "Electromagnetic calorimeter of Belle II". In: *Nuclear Instruments and Methods in Physics Research Section A: Accelerators, Spectrometers, Detectors and Associated Equipment* 958 (2020). Proceedings of the Vienna Conference on Instrumentation 2019, p. 162235. ISSN: 0168-9002. DOI: https://doi.org/10.1016/j.nima.2019.05.076. URL: https://www.sciencedirect.com/science/article/pii/S0168900219307405.

[32] URL: https://software.belle2.org/release-08-00-05/sphinx/index.html.

[33] T. Kuhr et al. "The Belle II Core Software". In: *Computing and Software for Big Science* 3.1 (2018), p. 1. DOI: 10.1007/s41781-018-0017-9. URL: https://doi.org/10.1007/s41781-018-0017-9.

[34] Anders Ryd et al. "EvtGen: A Monte Carlo Generator for B-Physics". In: (May 2005).

[35] S. Agostinelli et al. "Geant4—a simulation toolkit". In: *Nuclear Instruments and Methods in Physics Research Section A: Accelerators, Spectrometers, Detectors and Associated Equipment* 506.3 (2003), pp. 250–303. ISSN: 0168-9002. DOI: https://doi.org/10.1016/S0168-9002(03)01368-8. URL: https://www.sciencedirect.com/science/article/pii/S0168900203013688.

[36] Hauth, Thomas. "Belle II Track Reconstruction and Results from first Collisions". In: *EPJ Web Conf.* 214 (2019), p. 02032. DOI: 10.1051/epjconf/201921402032. URL: https://doi.org/10.1051/epjconf/201921402032.

[37] Tadeas Bilka et al. *Implementation of GENFIT2 as an experiment independent track-fitting framework*. 2019. arXiv: 1902.04405 [physics.data-an]. URL: https://arxiv.org/abs/1902.04405.

[38] Stefano Spataro. "Track Fitting for the Belle II Experiment". In: *EPJ Web Conf.* 214 (2019). Ed. by A. Forti et al., p. 02039. DOI: 10.1051/epjconf/201921402039.

[39] V. Baru et al. "Emergence of heavy quark spin symmetry breaking in heavy quarkonium decays". In: *Physical Review D* 107.1 (Jan. 2023). ISSN: 2470-0029. DOI: 10.1103/physrevd.107.014027. URL: http://dx.doi.org/10.1103/PhysRevD.107.014027.

[40] A. E. Bondar et al. "Heavy quark spin structure in $Z_b resonances$". In: *Physical Review D* 84.5 (Sept. 2011). ISSN: 1550-2368. DOI: 10.1103/physrevd.84.054010. URL: http://dx.doi.org/10.1103/PhysRevD.84.054010.

[41] Christian Bierlich et al. *A comprehensive guide to the physics and usage of PYTHIA 8.3*. 2022. arXiv: 2203.11601 [hep-ph]. URL: https://arxiv.org/abs/2203.11601.